SISSA  **ISAS**

SCUOLA INTERNAZIONALE SUPERIORE DI STUDI AVANZATI
INTERNATIONAL SCHOOL FOR ADVANCED STUDIES

High temperature physics and nanofriction properties of alkali halide surfaces

Thesis submitted for the degree of
Doctor Philosophiæ

Candidate:
Tatyana Zykova-Timan

Supervisor:
Erio Tosatti

October 2005

Contents

Introduction

Surface science is a mature field, where newer and newer experimental techniques have had a strong impact over the last three decades, and where many important and deep conceptual problems have been theoretically tackled and solved. Yet, the tools of surface science have just about begun to come of use for the larger class of problems that encompass strongly developing and strongly relevant areas such as nanoscience, adhesion, and friction.

The scope of this thesis is to use the theoretical and computational tools of surface physics and work out with them a case study whose full solution can have an impact in these areas. The case study we have chosen, is that of understanding the nonwetting habit of a certain crystal surface, sodium chloride (100), by its own melt, and to explore its consequences from various viewpoints, particularly in nanofriction. The reasons for this choice are manifold.

First, the nonwetting phenomenology is there, it is not exclusive to NaCl, and has been left without an explanation for about thirty years from the experiments of Mutaftschiev's group [1]. Second, bad wetting of a solid by a liquid involves poor adhesion, for which there are many typical examples in nature. However, there is no immediate understanding for why should a liquid be repelled by *its own* solid, as is the case here. Third, alkali halides represent a lucky case where thanks to the work of many people some 40-50 years ago, the interatomic forces are very accurately known, a fact which offers a natural line of attack through classical computer simulation. This would not be available for the other known cases of bad self-wetting, occurring mostly in metals and in semiconductors. Fourth, the high temperature behavior of a solid surface, including a full calculation of its temperature dependent free energy and a comparison with that of the liquid and of the solid-liquid interface has never been available so far, and here we can just do it. In particular, despite many long standing bulk studies, the physics of the molten salt *surface* has apparently not been addressed prop-

erly so far and can have surprises in reserve, as it indeed does. Sixth, simulated nanoexperiments can be carried out for this system, such as the deposition of a nonwetting nanodroplet on the hot solid surface, the melting of a nanocube, the scratching of a hot solid surface by a nanotip. These simulated experiments can be as illuminating as the real ones, albeit less difficult.

This thesis is organized into two parts. Here is an outline of the work which forms its body. The starting point of the project was to reproduce a classic experiment demonstrating NaCl partial wetting phenomena done by the group of Mutaftschiev [1, 2, 3] some decades ago. Since the substance used in the experiment is rather simple and commonly used the project can be considered a case study and can be easily generalized for the whole class of alkali halide materials.

In the first part following this brief introduction, I will present the broad theme of surface melting and nonmelting, as examples of different wetting habits of a liquid onto one face of its own crystalline solid. Next, I will briefly review the known phenomenology of NaCl surfaces with clear indications of partial or incomplete wetting. Then I will introduce the thermodynamical and simulation methods, and the Born-Mayer-Huggins-Fumi-Tosi (BMHFT) interatomic potentials that I will employ for my theoretical attack to this general problem, and to the case of an alkali halide in particular and its (100) surface. Many delicate points and well known or less well known pitfalls will be dealt with in this section.

Armed with this instruments, I will present extensive simulations of solid bulk NaCl from low temperatures extending until above the melting point, and of liquid NaCl from somewhat below the melting point upwards. Even at the pure bulk level, one finds that there are still new things that emerge here, despite a wealth of existing studies.

Following these two separate bulk studies, I will consider solid-liquid coexistence, and from the simulated behavior of the solid-liquid interface I will extract an accurate value of the bulk melting temperature of the BMHFT model, which is found remarkably close to the experimental value of NaCl. At this point I can begin the surface study properly said. I will describe separately solid-vapor and liquid-vapor interfaces and calculate their free energies. I will also present the deposition of a NaCl liquid nanodroplet on solid NaCl(100) directly illustrating partial wetting. Finally I will explain surface nonmelting and overheating and connect it with partial self-wetting by a simple model. I believe that this is the first study of this kind ever done.

The second part of the thesis is dedicated to the newly developing field of nanotribology. Here I will attempt to apply our present knowledge of the physics of NaCl(100) to the recently revived problems of friction and wear on atomically flat surfaces when brought to very high temperatures. In practice I will discuss our idealized AFM simulations of a tip sliding in contact mode with the high temperature surface. Since I was interested to reveal new frictional phenomena near the bulk melting temperature a natural choice was precisely to work with nonmelting surfaces like NaCl(100) which would resist scratching and local heating by the tip even at high temperatures.

The nanofriction simulations reveal two distinct and opposite phenomena. Deep ploughing friction of a sharp tip shows a drop of the frictional force close to $T_{\rm M}$, where the tip wades or skates through the hot solid, accompanied by a small moving liquid cloud, the furrow behind promptly healing and recrystallizing. At the opposite limit, the grazing (wearless) friction of a flat tip shows on the contrary a sharp surge of the initially weak frictional force as the surface lattice, still solid, turns increasingly compliant near $T_{\rm M}$. This surge may be understood as a nanofrictional analogue of the celebrated peak effect of sliding vortices in the mixed state of type II superconductors.

There have been no attempts as yet to conduct real nanofriction experiments on alkali halides—a very popular substrate at room temperature—at these higher temperatures, but I do hope that there will to verify the predictions that result from our work.

The work contained in this thesis has led and is leading to the following publications:

1. T. Zykova-Timan, D. Ceresoli, U. Tartaglino, W. Zaoui-Sekkal and E. Tosatti, *NaCl droplets on NaCl(100) at the melting point*, Surf.Sci. **566-568**, 794 (2004).

2. T. Zykova-Timan, D. Ceresoli, U. Tartaglino and E. Tosatti,*Why alkali halides solid surfaces do not wet by its own melt?*, Phys. Rev. Lett. **94**, 176105 (2005).

3. T. Zykova-Timan, D. Ceresoli, U. Tartaglino and E. Tosatti, *NaCl(100) surface: why does it not melt?*, *Highlights in the quantum theory of condensed matter, a volume in honor of M.P. Tosi*, Scuola Normale Superiore di Pisa (2005).

4. U. Tartaglino, T. Zykova-Timan, F. Ercolessi and E. Tosatti, *Melting and nonmelting of solid surfaces and nanosystems*, Phys. Rep. **411**, 291 (2005).

5. U. Tartaglino, T. Zykova-Timan, F. Ercolessi and E. Tosatti, *Surfaces, materials and nanosystems near the melting point*, J. Mater. Sci. **40**, 2141 (2005).

6. T. Zykova-Timan, D. Ceresoli, U. Tartaglino and E. Tosatti, *Physics of alkali halide solid and liquid surfaces near the melting point*, to appear in J.Chem.Phys.

7. D. Ceresoli, T. Zykova-Timan and E. Tosatti, *Electron-stimulated emission of Na atoms from NaCl nanocube corners*, submitted to Surf.Sci.

8. T. Zykova-Timan, D. Ceresoli, U. Tartaglino and E. Tosatti, *Physics and nanofriction of alkali halide surface near the melting point*, submitted to Surf. Sci.

9. T. Zykova-Timan, D. Ceresoli, and E. Tosatti, *Peak effect versus skating in high temperature surface nanofriction*, in preparation.

Part I

The thermodynamics of rocksalt surfaces

Chapter 1

Overview of bulk and surface melting phenomena

This chapter is a brief general review of melting, nucleation and accompanying processes on solid surfaces. Firstly I will briefly classify the basic phenomena arising at melting near the interfaces, paying particular attention to the connection of wetting (nonwetting) and melting (nonmelting). Secondly I will survey the principal experiments, basic approximations and popular theoretical models used to predict the melting properties in the past and nowadays. Then I will proceed describing the numerical simulations which presently offer a powerful tool to study these and other phenomena. Here I will confine myself mainly to known computational simulations of *surfaces* at high temperatures. Finally I will focus on *surface nonmelting* and *overheating*—the main subjects of the current study— and will enumerate the various possible mechanisms of the surface nonmelting that can make solid overheating possible. Of course, in this very fast review of surface melting I do not intend to give a complete description of all the overwhelming and complex problems connected with the melting transition, my goal is merely to show a glimpse to the iceberg apex (Fig. 1).

1.1 Definitions: melting, surface melting and nonmelting

In bulk system the *melting point* $T_{\rm M}$ of a homogeneous pure solid phase arises when the chemical potentials μ(P,T) of solid and liquid states are equal (Fig. 1.1). Below or above the crosspoint of solid and liquid chemical potentials only the

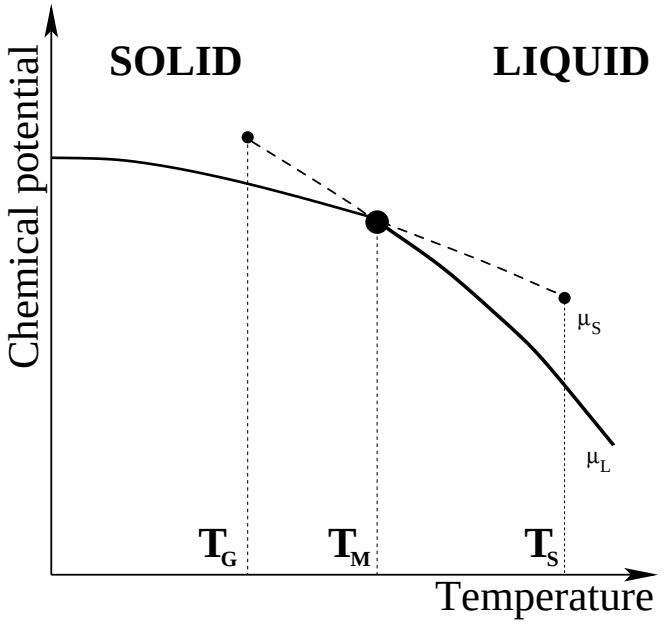

Figure 1.1: The solid μ_S and liquid μ_L chemical potentials at fixed P versus temperature. The dash lines show the metastable regions. The melting temperature $T_{\rm M}$ is a crosspoint of two curves. $T_{\rm S}$ and $T_{\rm G}$ are the spinodal points of the solid and liquid bulk phases correspondingly.

phase which possesses the lowest chemical potential remains stable. The other phase can still exist in its metastable state up to a spinodal point $T_{\rm S}$ and down to a glass temperature $T_{\rm G}$. As a result, it should generally be possible to undercool the high temperature phase, and to overheat the low temperature phase. Periodic heating and cooling through the first order transition should thus generate a full hysteresis cycle.

In melting, this is only half true. Supercooling of the liquid is allowed by the absence of a solid germ; overheating of the solid is prevented by that omnipresent germ, a surface. This observation provides perhaps the first macroscopic hint that

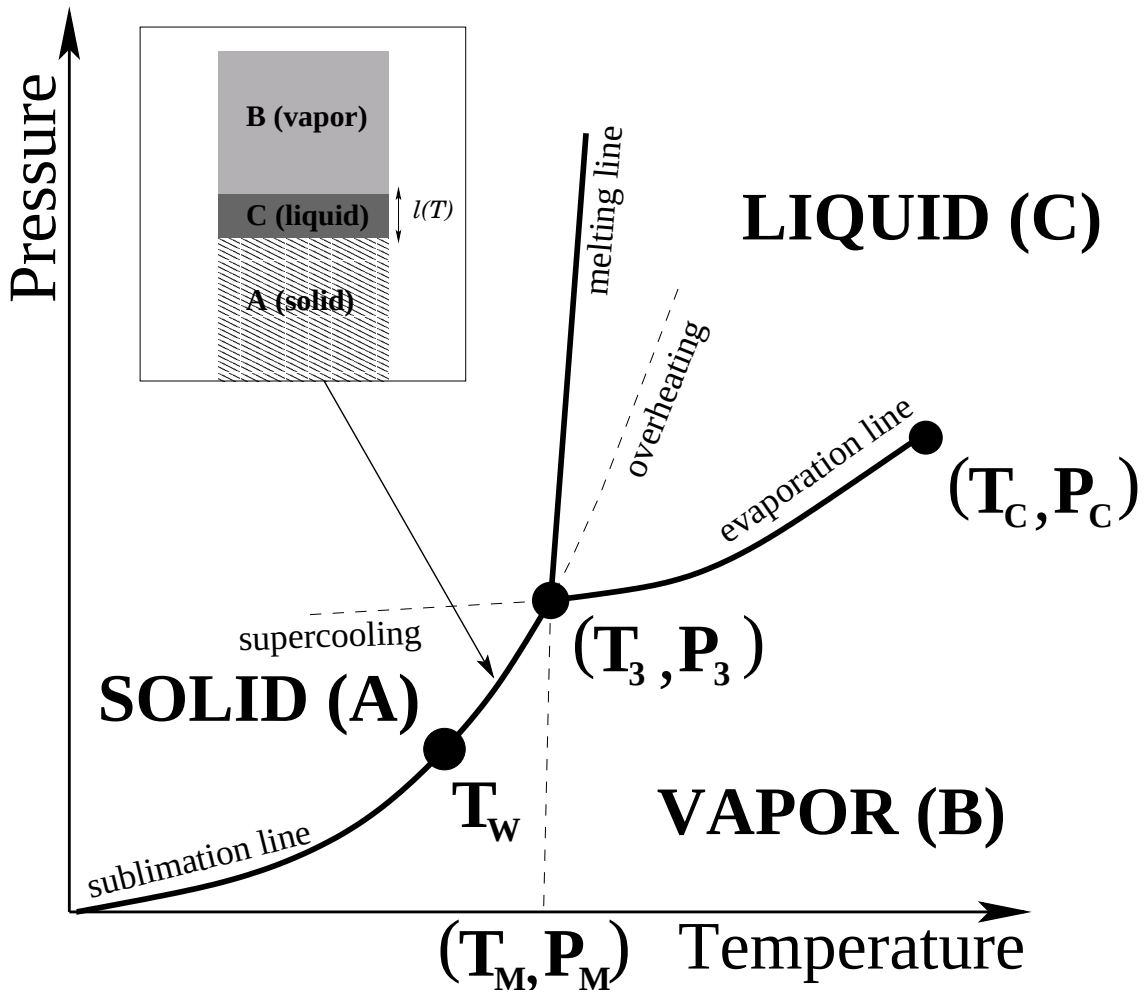

Figure 1.2: The generic bulk phase diagram in P-T variables for a pure homogeneous system with solid, liquid and gas interface. The melting- and sublimation-lines meet the evaporation line at the triple point (T_3, P_3). The extrapolation of the melting line ends at the melting point (T_M, P_M) at zero pressure. The evaporation line ends at the critical point (T_C, P_C). The inset shows the surface melting which may occur at the solid-vapor interface $T_{\mathrm{W}} < T < T_3$.

solid surfaces might be already wet somewhat below the bulk melting point. The starting motivation for a microscopic study of surface melting begins right there. In order to find out under which conditions surface melting occurs let us consider the system near the *triple point* (Fig. 1.2) where three phases (solid, liquid, gas, for a simple material) are in coexistence. If we move along the coexistence line (*sublimation line*) of two phases A (solid) and B (vapor) towards the triple point where the phase C (liquid) becomes thermodynamically stable as a bulk phase, wetting may arise: a thin film of the third phase C may intervene between A

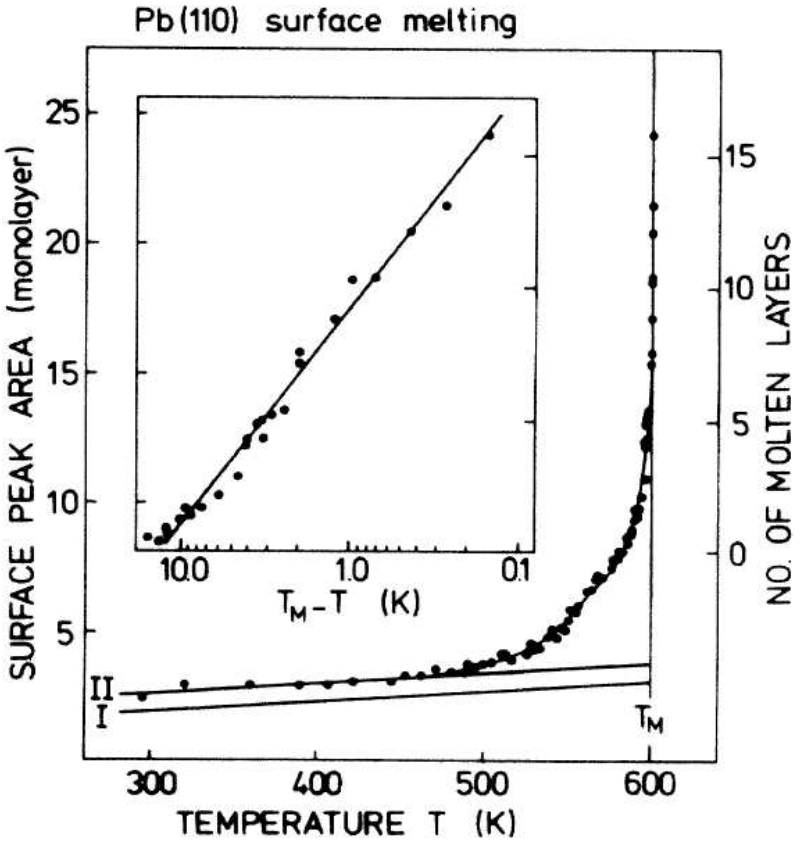

Figure 1.3: Experimental evidence of surface melting of Pb(110): Medium energy ion scattering shows an increasing number of disordered (liquid) layers approaching the melting temperature. From Ref. [4]

and B (Fig. 1.2, inset), even if the triple point is not yet reached. If phase C (the liquid) wets the A-B interface, a thin wetting film of C can appear well below $T_{\rm M}$. The temperature $T_{\rm W}$ where this process happens is called the surface melting temperature or wetting temperature. *Surface melting* (SM) arises above $T_{\rm W}$ when the thickness $\ell(T)$ of the liquid film diverges as T approaches the triple point along the sublimation line. SM is quite common for most elemental materials. A rather famous microscopic characterization of SM is that of Pb(110), first reported by Frenken and van der Veen [4]. Medium energy ion scattering data revealed (Fig. 1.3) the presence at the solid-vapor interface of a disordered (liquid) film whose thickness $\ell(T)$ grows without limit as $T \to T_{\rm M}$.

SM is not universal, and several surfaces are known that do not melt, but remain solid and crystalline all the way up to $T_{\rm M}$. Not surprisingly, this behavior has been called surface nonmelting (NM) [5]. Slightly more surprisingly, SM and

NM can both occur for the same substance, of course on two different crystallographic faces. For example, NM was demonstrated for Pb(111) [6], while by contrast SM prevails on Pb(110).

Exchanging roles of A, B and C we might instead take A = liquid, B = vapor, C = solid, consider cooling a liquid-vapor interface along the coexistence line, and ask whether a thin solid film might occur at this interface, above the freezing point. This is called *surface freezing* [7]. In general one can notice a kind of symmetry between SM and surface freezing. The SM and the lack of overheating have been discussed above. Surface freezing of a liquid will similarly imply a lack of supercooling of the bulk liquid. Surface freezing is a relatively rare phenomenon characterized by the existence of finite solid surface film floating on the liquid phase above T_{M}. It has been mainly observed in alkanes [8, 9] and alcohols[10]. Clearly SM excludes the possibility of surface overheating and surface freezing of the liquid excludes the supercooling. The Table.1.1 summarizes the conditions of both surface phenomena. In this table γ_{SV}, γ_{SL}, γ_{LV} indicate regular interface

	$\mathrm{T} \leq T_{\mathrm{M}}$		$\mathrm{T} > T_{\mathrm{M}}$
In liquids:	bulk supercooling $\gamma_{\mathrm{LV}} < \gamma_{\mathrm{SV}} + \gamma_{\mathrm{SL}}$	OR	surf. freezing $\gamma^{+}_{\mathrm{LV}} \geq \gamma_{\mathrm{SV}} + \gamma_{\mathrm{SL}}$
In solids:	surf. melting $\gamma^{+}_{\mathrm{SV}} \geq \gamma_{\mathrm{LV}} + \gamma_{\mathrm{SL}}$	OR	bulk overheating $\gamma_{\mathrm{SV}} < \gamma_{\mathrm{LV}} + \gamma_{\mathrm{SL}}$

Table 1.1: Surface phenomena and thermodynamical conditions for their existence below and above T_{M}.

free energies, whereas γ^{+}_{SV} and γ^{+}_{LV} indicate some kind of saddle-point solid-vapor and liquid-vapor surface free energies, evaluated in a situation where these two interfaces are not really stable.

In the language of wetting, SM is nothing else than complete interfacial wetting of the solid by *its own melt*. (This is reminiscent, but not really coincident with *triple point complete wetting* which happens when the solid substrate and the wetting liquid are made of different materials)[11]. By contrast, NM corresponds to partial wetting, schematized in Fig. 1.4. In this case, there is a clear connection between the surface thermodynamic parameters and the angles of partial wetting [12] as will be clarified further below. Thermodynamically, NM will take place whenever the solid surface (solid-vapor interface) is unable to lower its free energy by turning into a sequence of two separate solid-liquid plus liquid-vapor

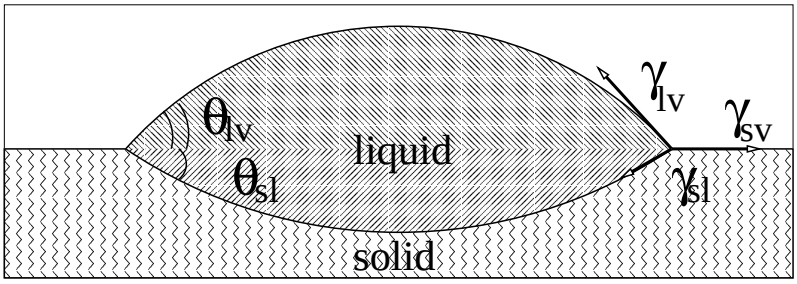

Figure 1.4: Partial wetting of a solid by its own melt is an indirect evidence of surface nonmelting. The $\gamma_{\rm LV}$, $\gamma_{\rm SV}$ and $\gamma_{\rm SL}$ are the free energies of the interfaces; $\theta_{\rm SL}$ and $\theta_{\rm LV}$ are the interior and outer contact angles.

interfaces, namely when

$$\gamma_{\rm SV} < \gamma_{\rm SL} + \gamma_{\rm LV}\,, \tag{1.1}$$

In general, $\gamma_{\rm SV}$ is at most equal to $\gamma_{\rm LV}$+ $\gamma_{\rm SL}$, and $\gamma_{\rm LV}$ is at most equal to $\gamma_{\rm SV}$+ $\gamma_{\rm SL}$ [13]. Conversely, when the inequality (1.1) does not hold, SM will ensue instead of NM. There is an interesting connection between these interface free energies and the physics of surface melting.

As Fig. 1.3 shows, in SM the liquid film, although technically of divergent thickness at $T_{\rm M}$, remains atomically thin until fractions of a degree below $T_{\rm M}$. Interactions propagate readily across such a thin liquid film. The solid-liquid and the liquid-vapor interfaces "feel" their mutual presence, so much that they actually merge when $\ell(T)$ is small enough. For a generic temperature $T < T_{\rm M}$ the free energy change caused by melting a film of thickness ℓ can be written

$$\Delta G/A = [(\gamma_{\rm SL} + \gamma_{\rm LV}) - \gamma_{\rm SV}] + \ell L \rho_{\rm L}(T_{\rm M} - T) + V(\ell) \tag{1.2}$$

where A is the surface area, L is the latent heat of melting per unit mass, $\rho_{\rm L}$ is the density of the liquid, and $V(\ell)$ represents a phenomenological "interaction" free energy term between the liquid-vapor and the solid-liquid interfaces. As defined by (1.2), the interaction $V(\ell)$ vanishes for $\ell \to \infty$, and tends to $V(0) = \gamma_{\rm SV} - (\gamma_{\rm SL} + \gamma_{\rm LV})$ when $\ell \to 0$, where the dry solid surface free energy is recovered. Eq. (1.1) amounts to say that in SM the interface interaction $V(\ell)$ is globally *repulsive*, whereas in NM it is *attractive*. In case when the interactions $V(\ell)$ between SL and LV are Van der Waals type it takes the form $-H/\ell^2$ where H is Hamaker constant [14].

The microscopic mechanism behind interface attraction or repulsion varies, and may be eventually related to such different physical causes as layering or-

der [12], van der Waals forces [15], or molecular order [16]. We will discuss this in detail in Section 1.4.

1.2 Empirical laws of melting and freezing

Although in general the melting and freezing transition of a substance is very specific and non-universal, some useful phenomenological criteria have been given to the melting of a solid or the freezing of a liquid which are usually based on the properties of only one of the two coexisting phases. The advantage of these empirical rules is that they sometimes permit a prediction of the solid-liquid coexistence point avoiding much more difficult but more satisfactory free energy calculation.

Two very different rules have been identified. The first starts from the solid phase and the second from the liquid one.

- The solid-based empirical rule of bulk melting is the so-called Lindemann criterion according to which a crystal melts when the amplitude of thermal vibrations (r.m.s.) reaches a certain percentage of the average size of the unit cells [17]. For many materials this Lindemann ratio $(\overline{\Delta r^2})^{1/2}/a$ is of order of $\simeq 0.15\%$. It becomes a useful criterion for melting with a rather wide applicability, since the precise value of ratio is insensitive to details of the potential, at least for simple substances. A generalized formulation of Lindemann criterion was formulated by Ross [18]. The Ross criterion is equivalent to assuming the reduced free volume constant along the melting line. The rule proves quite successful in predicting the melting properties both of rare gases and liquid metals, given reasonable choices for the pair potentials.

  Atoms at surfaces are less coordinated and more free than in bulk, and consequently their vibration amplitudes are larger. Surfaces may thus reach the Lindemann instability vibration amplitude at a lower temperature than the bulk. A model embodying the bulk Lindemann criterion is the mechanical thermal instability model [19]. An infinite solid will, if prevented from melting, become mechanically unstable at a sufficiently high temperature. Although the ideal mechanical instability temperature of a solid is different, and of course higher than the true melting temperature T_{M} (where the free energy crossing of solid and liquid phases takes place) as in Fig. 1.1, it can

nonetheless heuristically be taken as a qualitative indicator of the tendency of the solid to melt. Adopting that line, one can ask whether the stability of the *surface* will not cease before that of the bulk. In a model semi-infinite solid it is found indeed that the mechanical instability of the first surface layer occurs at a temperature which is only 73% that of the bulk [20]. This suggests – correctly – that solid surfaces should begin to soften and melt at about 3/4 the bulk melting temperature. That is indeed generally the case, as has been long known and noted by such precursors as Tammann and Stranski [21]. Self-consistent surface phonon calculations [22] and also experiments [23] in fact reveal a much more pronounced anharmonic outward expansion of the first surface layer relative to that of the bulk, exhibiting a very steep increase well below the melting temperature $T_{\rm M}$ of the bulk. Although it is not really possible to generalize, that is undoubtedly one of the qualitative elements heralding a stronger tendency of a surface to become unstable before the bulk.

- A second liquid-based criterion was formulated by Hansen and Verlet [24]. For a Lennard-Jones (LJ) liquid they found by computer simulation that the first maximum of the liquid structure factor *S(k)* has a constant amplitude of 2.85 along the freezing line. By scattering experiment and by computer simulation of various systems other than LJ it was found that the maximum of *S(k)* is always close to 3 at freezing. In general the freezing sets in if the short-range order in the liquid system, measured by the first maximum exceeds a certain universal value.

1.3 Ginzburg-Landau (Cahn-Hillard) theory of surface melting

To a first approximation, one may consider that liquid and solid differ in their (average) density ρ. The simplest theory of SM is based on optimizing the order parameter spatial profile, in particular the density profile $\rho(\mathbf{z})$ of a solid-vapor interface in a system with short range interactions. Assuming a bulk grand potential density $\omega = \omega(\rho)$, the solid vapor coexistence near the triple point as in Fig. 1.2 implies two equivalent solid and vapor minima of the grand potential per unit volume $\omega(\rho) = \omega_o$ plus one additional secondary liquid minimum with a higher grand potential density $\omega_o + \Delta$. The total grand potential of an inhomo-

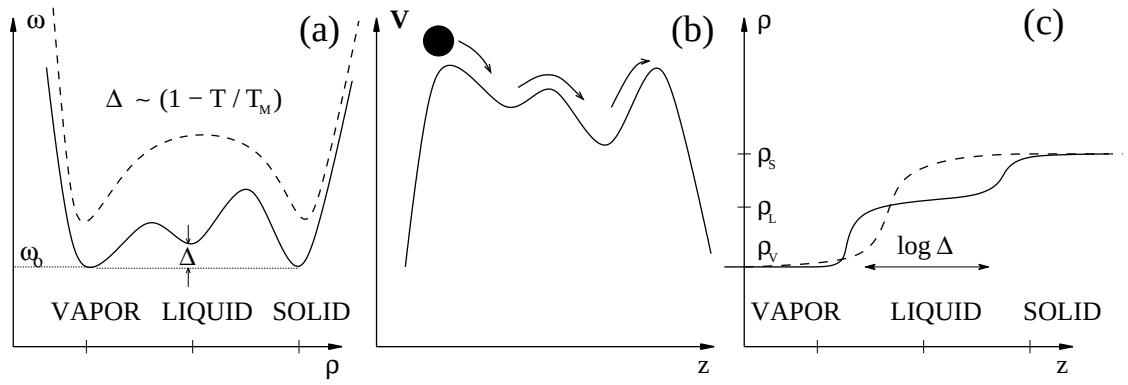

Figure 1.5: (a) Grand potential profile close to the melting point (solid) and well below $T_{\rm M}$ (dashed) , (b) Mechanical equivalent of the interface free energy minimization (see text), (c) Density profile, showing that the SV interface has split into a SL plus LV close to $T_{\rm M}$ (solid) but not well below $T_{\rm M}$ (dashed).

geneous system such as the solid-vapor interface can be written

$$\Omega = \iiint d^3x \, \left[\omega(\rho(\mathbf{x})) + \frac{J}{2}\left|\nabla\rho\right|^2\right] \tag{1.3}$$

In this Ginzburg-Landau (or Cahn-Hillard) type of free energy (acceptable for a system with short range forces) the first term represents the thermodynamic potential density for a uniform system, while the gradient term signifies the extra cost caused by any spatial change in the order parameter (supposed to be slowly varying). To describe a solid-vapor interface [25] we may assume $\rho = \rho(z)$ and seek to minimize Ω (per unit area):

$$\Omega/A = \int dz\, \omega(\rho(z)) + \frac{J}{2}\left(\frac{d\rho}{dz}\right)^2 = \min \tag{1.4}$$

where $J > 0$ is a parameter, and the constraints $\rho(-\infty) = \rho_{\rm S}$ and $\rho(+\infty) = \rho_{\rm L}$, where $\rho_{\rm S}$ and $\rho_{\rm V}$ are solid and vapor densities respectively. $\omega(\rho(z))$ has the shape shown on Fig. 1.5a.

This minimum problem is formally identical to the minimum action problem for the one dimensional Lagrangian motion of a classical point object of coordinate ρ, mass J, as a function of time z, in a potential $V = -\omega(\rho)$ (Fig. 1.5b): Starting at time $z = -\infty$ with zero kinetic energy and with a small $\rho = \rho_{\rm V}$ from a first hilltop of height $-\omega(\rho_{\rm V}) = -\omega_o$ (the vapor phase), the point moves "downhill" eventually reaching at time $z = +\infty$ the last, and exactly equivalent, hilltop $-\omega(\rho_{\rm S}) = -\omega(\rho_{\rm V}) = -\omega_o$ (the solid phase) (Fig. 1.5).

At temperatures well below the melting point, there is no liquid phase (not even metastable), meaning that there exists no liquid-like local minimum in $\omega(\rho)$ (Fig. 1.5a, dashed line). Thus $-\omega(\rho)$ has no other maxima than the vapor and solid hilltops, and the resulting solid-vapor interface is unsplit and featureless (Fig. 1.5c, dashed line). Closer to $T_{\rm M}$ however $-\omega(\rho_{\rm V})$ develops a secondary maximum—a lower hilltop, as it were—at an intermediate $\rho = \rho_{\rm L}$. En route between the vapor to the solid hilltops, the point particle must negotiate this intermediate "mountain pass", where it will not stop, but will still slow down considerably. It is easy to check that if $\Delta = \omega(\rho_{\rm L}) - \omega(\rho_{\rm S})$ is the height difference between main and secondary hilltop (the free energy difference between solid and liquid, that goes to zero only at the melting point), then the "time" δz the point will spend near the liquid hill (and therefore with $\rho \approx \rho_{\rm L}$ is proportional to $\log \Delta$). The interface density profile is now split into two interfaces: first a vapor-liquid one, then a liquid-solid one (Fig.1.5c). They are separated by a liquid film of density close to $\rho_{\rm L}$, whose thickness $\ell = \delta z$ is logarithmically increasing as $T \to T_{\rm M}$. And this is just surface melting.

The above also suggests that one might identify the temperature $T^* < T_{\rm M}$ where the *bulk* free energy first develops the local minimum corresponding to the liquid phase, with the temperature where a solid surface is likely to begin wetting itself with the thinnest liquid film. It must be underlined that this simple heuristic theory only describes SM and cannot account for NM or for many other complications, upon which we shall return below.

1.4 Occurrence and mechanisms of surface melting/nonmelting

Surface melting has been studied in a variety of systems by experiments and by simulations:

Rare gas solids are reasonably described through a Lennard-Jones potential. As first shown by extensive MD studies by Broughton and collaborators [26, 27] they are expected to display surface melting on all crystalline faces. Here truly microscopic experiments are not abundant, because of technical difficulties. There is however a large body of work by the surface adsorption community, interested in understanding absorbtion isotherms (a relationship between the partial pressure of an adsorbate gas and the surface coverage of the adsorbent at constant temperature) as a function of tempera-

ture [28].

Metals and their surface melting behavior has received by comparison much more experimental attention. Metal surfaces usually possess positive Hamaker constants (see Section 1.1), and generally melt. In detail, they may occasionally exhibit nonmelting, depending on the metal and on the crystallographic orientation. A minority of close packed surfaces such as Pb(111) [6], Al(111) and Al(100) [29], etc. display NM, and remain in fact smooth and dry all the way to $T_{\rm M}$. The vast majority of metal faces consisting of all other orientations, where packing is poorer, undergo SM. In intermediate packing cases like for instance Pb(100) [4], the first few layers melt, but the wetting does not proceed and the liquid film growth is blocked to a finite thickness until $T_{\rm M}$ (incomplete SM). Although this incomplete melting will macroscopically appear just the same as NM—namely partial wetting with a finite wetting angle—there is a clear microscopic difference because the surface is no longer dry below $T_{\rm M}$. An early review of SM on metals can be found elsewhere [30].

In surface NM there exists a critical liquid nucleation thickness ℓ_{crit} which is finite above $T_{\rm M}$ and only vanishes at some "surface spinodal temperature" $T_{\rm SS} > T_{\rm M}$. This fact, first discovered in simulation[5], indicates that in NM the solid surface is metastable, and protected by a nucleation barrier, between $T_{\rm M}$ and $T_{\rm SS}$. An immediate consequence is that NM solid surfaces can be overheated, of course only for a short time, up to at most $T_{\rm S}$. For the (111) surfaces of Pb, Al and Au the calculated amount of maximum theoretical surface overheating $O = T_{\rm SS} - T_{\rm M}$ is 120K, 150K, and $\sim$ 150K respectively. This possibility was demonstrated experimentally by laser heating techniques [31], and also in small Pb clusters [32].

A second interesting point is the microscopic investigation and clarification of the relationship between solid surface NM and its partial wetting by a drop of melt. While macroscopic partial wetting with a nonzero contact angle of the liquid with its own solid is not commonly reported, it is very clearly found by simulation [12].

In addition to the above thermodynamics, there is a simple microscopic understanding for the physics that leads to NM of the close packed metal surfaces. It has to do with the intrinsic atomic structure of the two SL and LV interfaces involved. A series of z-resolved in-plane averaged density profiles of the SL and LV interfaces as displayed by MD simulations of suitably

prepared liquid films on Au(111), Au(110), and LJ(111) near their respective $T = T_{\mathrm{M}}$ is shown in Fig. 1.6. A well defined damped density oscillation

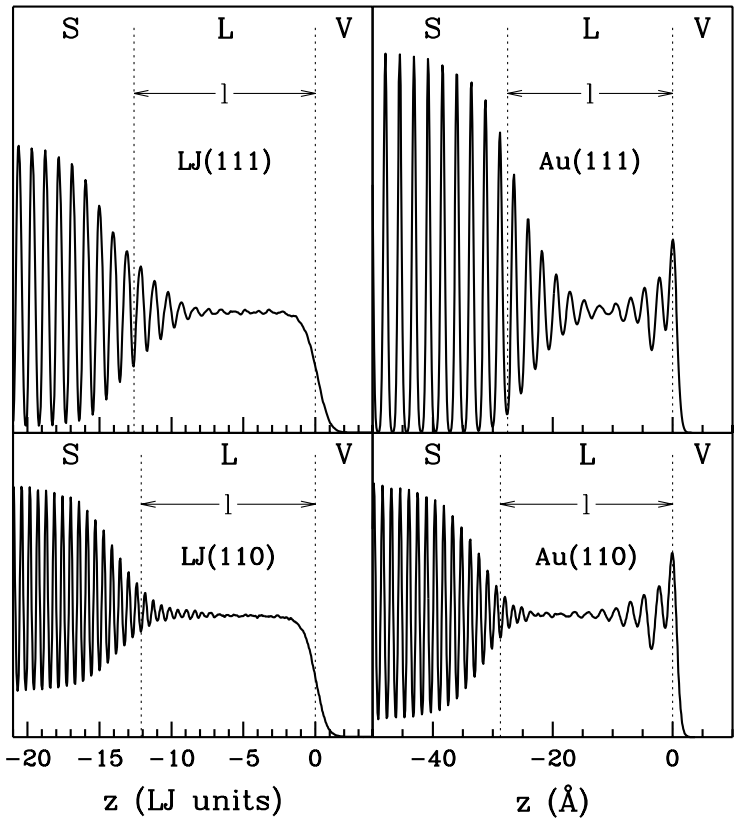

Figure 1.6: Typical solid-liquid-vapor density profiles obtained by simulations of Lennard-Jones(110), (111) and Au(110) (three surfaces that undergo SM) just below T_{M}. For Au(111) (which is instead a NM surface) a nonequilibrium configuration is shown with two facing equal-period density oscillations which lead to attraction and eventually to the collapse of the two interfaces (see text). Picture from Ref. [33]

is seen to propagate from the solid into the liquid, carrying approximately the solid interplanar distance as a wavelength. That wavelength of course depends on the crystallographic direction, in the present example it is large for (111) but small for (110). A second damped density oscillation starts at the liquid surface, carrying *inwards* a generally different wavelength, determined this time by the main peak in the liquid structure factor $S(k)$. This second oscillation (layering), essentially non-existent in the LJ liquid, is gen-

erally strong in a metal. Being a property of the liquid, the surface layering oscillation of the surface melted film is obviously face *independent*.

When, as in Au(110), the solid and liquid oscillations facing one another possess wavelengths that are out of tune, then their superposition is unfavorable and causes interface repulsion, eventually leading to SM. That is what happens most commonly. When instead (as in Au(111)) the two oscillations are close to being perfectly tuned, their superposition is favorable and causes interface attraction, leading to NM. This situation is typically realized on the closest packed metal surfaces such as Pb(111), Al(111). Finally, the practical absence of a layering oscillation in the LJ liquid surface indicates indifference of the two interfaces. They nonetheless eventually interact via the positive Hamaker constant (see Section 1.1), and therefore SM ensues in that case too.

Valence semiconductors such as Si, Ge, GaAs and semimetals like Ga are known to turn both fully metallic, and denser, either at high pressure or when they melt at high temperature. This case is special since the van der Waals forces [13] are inverted in this case, turning the interaction from repulsive to attractive. In fact, the higher liquid density here causes the Hamaker constant H to be negative [34], and this necessarily hinders complete surface melting. Reports of regular SM with unlimited growth of the liquid film at T_{M} that have appeared for Ga [35] are apparently incompatible with the negative Hamaker constant, and might be an artifact, possibly due to strains. Due to the long range attraction, regular and complete SM is excluded for all faces of these $H < 0$ materials.

1.5 Alkali halides interface properties near the melting point

Surfaces of ionic crystals such as NaCl, MgO, etc, are often used as substrates for growing other materials, and their properties are therefore better known far below the melting point. Yet, some data are also available about their behavior at T_{M}. As it was discussed long ago in the literature, an ionic salt does not possess any stable surface that is not neutral[36]. The basic neutral surface is rocksalt structure is 100 (see Fig. 1.7). This surface was well characterized by the neutron scattering [37, 38]. The surfaces of molten salts has been poorly studied so far

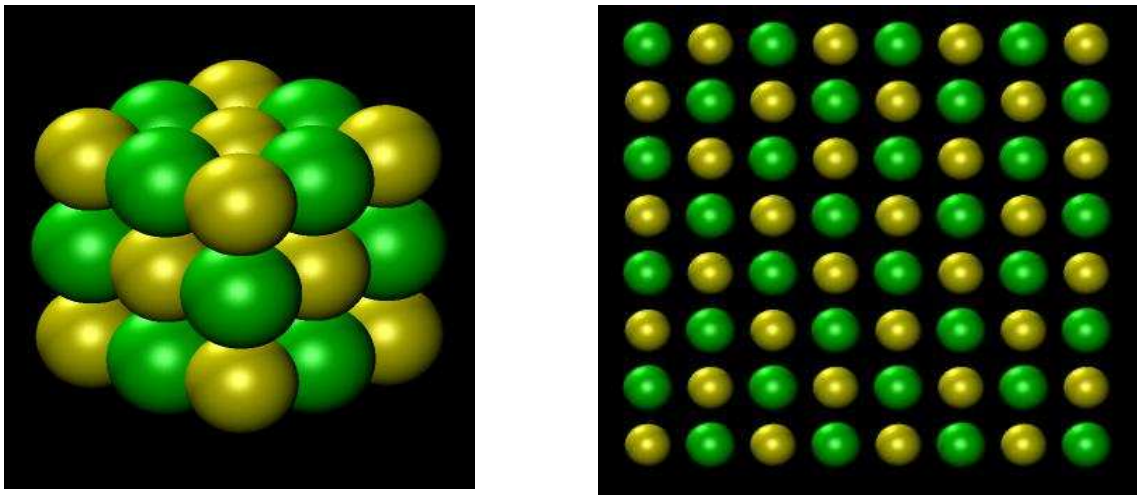

Figure 1.7: The fcc crystal structure of NaCl and (100) face

though there are results for surface tension[39], theoretical approaches and early simulations[40].

The contact angle measurements at the NaCl(100) crystal-melt interface

Here I will consider the wetting of solid NaCl by its own liquid. A very precise experimental determination of the wettability of NaCl crystal by its own melt was performed by a group of Mutaftschiev beginning in 1975 [1, 2, 3].

Commonly measurements of the crystal-melt contact angle meet great difficulties due to the impossibility of maintaining thermal equilibrium at the melting point. The widespread method based on the profile of a sessile drop on a solid substrate is not an exception. Mutaftschiev *et al* implemented a new technique (so-called ”bubble method”) using inert bubbles injected toward a solid surface in contact with the melt in a nearly two-dimensional setup. The main advantage is the possibility to obtain a quasiequilibrium steady state growth solid-melt interface at a temperature slightly away from T_{M}. The ultra-pure gas of the bubble contains fewer impurities with respect to the ambient gas phase during sessile drop observation. It is easy to extract the contact angle at the solid-liquid-vapor interface from the two-dimensional bubble's profile [41].

The results revealed a surprising lack of complete wetting of the molten salt on the solid (100) surface, with a large partial self-wetting angle of about 48° (Fig. 1.8) in NaCl and 50° in KCl. As was mentioned before (Section 1.1) the wet-

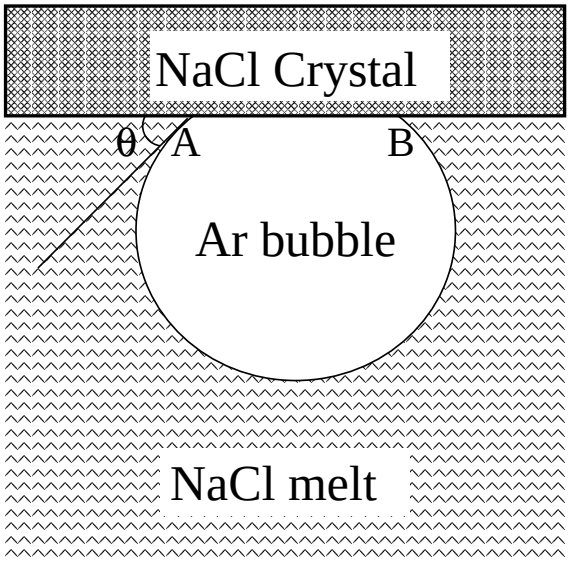

Figure 1.8: Argon bubble studies of liquid NaCl in contact with the solid revealed a surprising lack of complete wetting, with a large partial wetting angle of about 48 degrees.

ting angle at T_{M} is a universal characteristic of the solid-melt contact. It reflects the interface free energies balance and the nature of the interaction between SL-LV interfaces. Mutaftschiev made an attempt at estimating the γ_{LV}, γ_{SV} and γ_{SL} individual contributions[3]. Whereas the contact angle and liquid-vapor free energy γ_{LV} are available from direct measurements of the bubble and of the liquid surface tension respectively, the γ_{SV} could be only crudely extrapolated from γ_{LV} experimental values. That is a bad approximation especially in view of the striking diversity of solid and liquid alkali halide. The last unknown ingredient is γ_{SL}. For many elements it might be indirectly estimated empirically by using e.g. Turnbull's rule [42] which connects γ_{SL} with heat of fusion or it could be extracted from the nucleation experiment [43]. For NaCl(100)/NaCl melt the interface free energy γ_{SL} is simply not known.

In this theoretical thesis I will arrive at reasonably accurate interface free energies γ_{SV},γ_{LV} , γ_{SL} using a specific technique for each of them. γ_{LV} in particular will be derived via a surface stress calculation, γ_{SV} by a free energy thermodynamic integration (the first to our knowledge for a solid surface) and γ_{SL} is derived from direct simulation of partial wetting of NaCl(100) by a liquid droplet and subsequent use of Young's equation. The detailed physics behind these three numbers will be my main scope, along with explaining in detail the partial wetting results

of Mutaftschiev *et al*.

How do the NaCl clusters melt?

Another area of potential interest is the explanation of equilibrium crystal shapes of NaCl clusters at high temperatures. As it is shown in the experiments of Heyraud and Métois (see Fig.1.9) at 893 K the cluster's profile remains strictly cubic and persists up to the *corner rounding* temperature $T_0 \simeq 923$ K. At T_1 = 983 K the facets are entirely separated by rounded regions[44]. This rounding has an interpretation in terms of surface roughnening[45]. However, the roughening explanation does not clarify a possible role of liquid-like mobility so very close to the melting point. The rounded region could in reality be a liquid lens, which besides being rough, would also be diffusive and mobile. Alkali halides cluster melting has been addressed by R.S. Berry and collaborators[46], who concluded that melting occurs abruptly. However the role of corners has not yet been investigated properly.

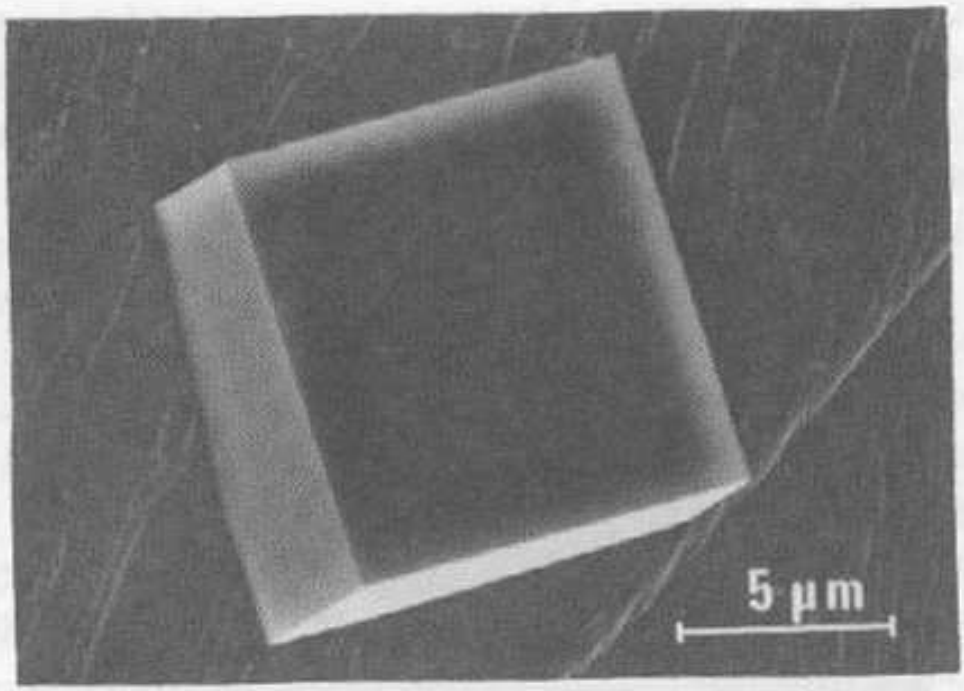

Fig. 2. Equilibrium shape of NaCl crystal at 620 °C observed by SEM.

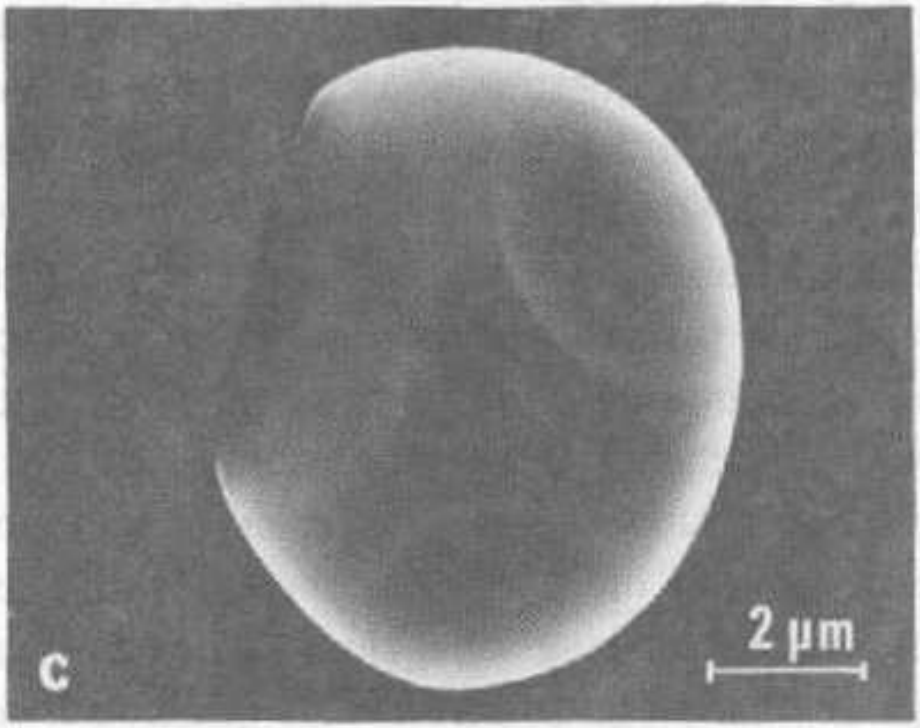

Fig. 3. Equilibrium shape of NaCl crystal at 710 °C; (a)–(c)

Figure 1.9: The equilibrium crystals of NaCl at (a) 893 K and (b) 983 K. From Ref. [44]

Chapter 2

MD calculations and interatomic potentials

In present Chapter I will commence with a detailed description of the main technical features used in our Molecular Dynamics (MD) simulations: molecular dynamics propagators, temperature control, Ewald sum, calculation of pressure and surface tension. Then I will discuss the specific methods applied to the surface such as surface free energy integration, the "effective" approximation and other necessary techniques used in our study.

2.1 Simulation methods

Atomistic simulations constitute a very important tool in the field of melting and surface melting. They can be either of Monte Carlo (MC) type, or of the Molecular Dynamics (MD) type. The main advantage of the MD method over the MC is that it allows the calculation of dynamical properties in addition to the equilibrium properties which can be obtained by either method. Under "ergodic hypothesis" one fundamental principle is that ensemble averages can be computed as time averages over the trajectories in the phase space:

$$\langle A \rangle = \lim_{t_{obs} \to \infty} \int_0^{t_{obs}} A(\Gamma(t)) dt \tag{2.1}$$

where $\langle ... \rangle$ denotes average over ensemble and $\Gamma(t)$ is the trajectory in phase space. The MD simulations consist in solving Newton's equations of motion

$$M_i \ddot{\mathbf{R}}_i = -\nabla_i E_{\rm pot}(\{\mathbf{R}\}) \tag{2.2}$$

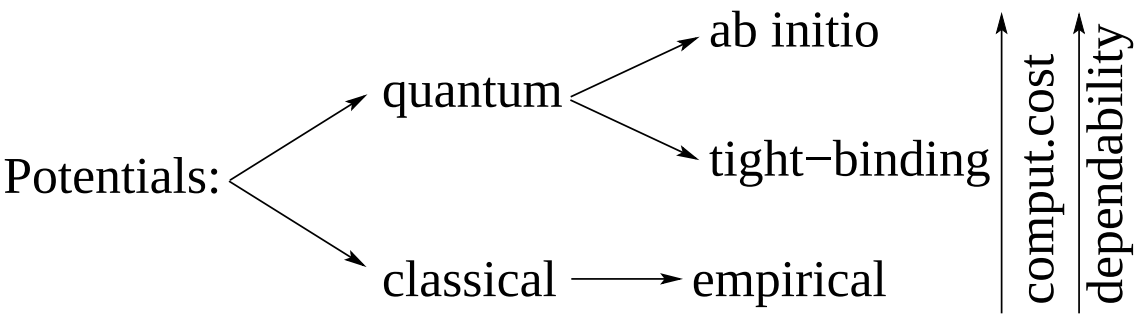

Figure 2.1: Classification of interatomic potentials.

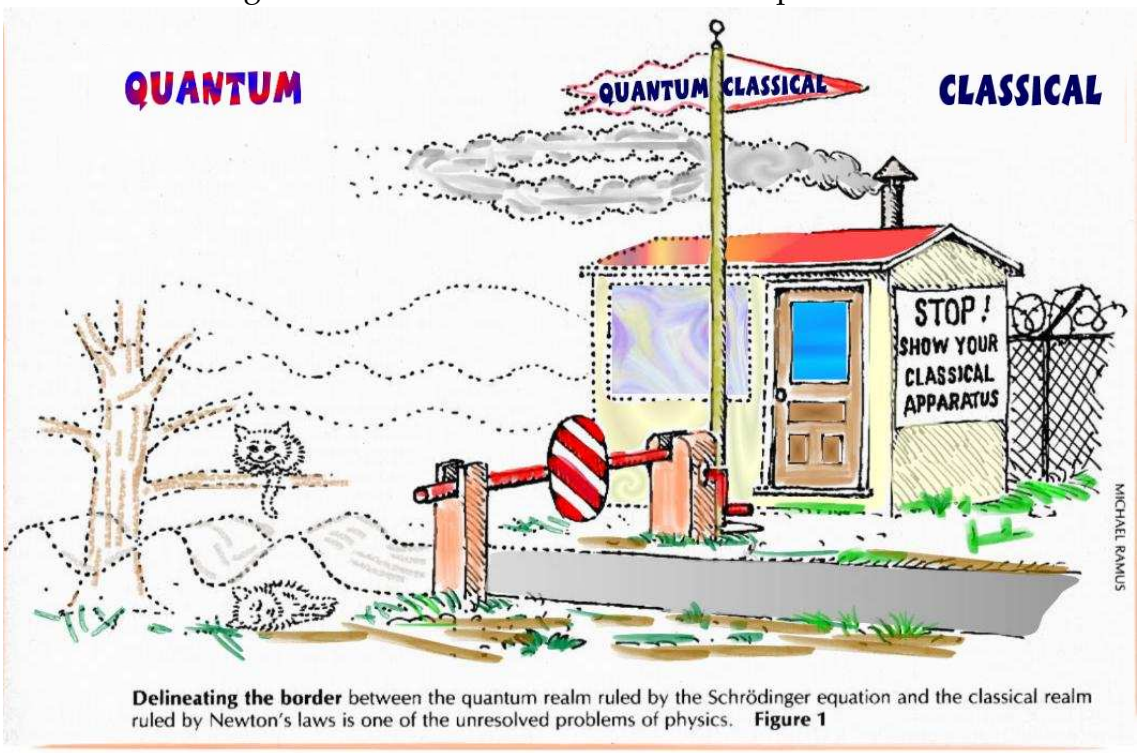

Figure 2.2: After Ref. [47]

for all particles of mass M_i, and coordinates $\mathbf{R}_i$.

The basic input needed in MD is the potential energy $E_{\rm pot}(\{\mathbf{R}\})$ as a function of all coordinates. Depending on systems, and on the accuracy needed, the choice is between empirical interatomic potentials on one side, and first principles total energy determinations of $E_{\rm pot}(\{\mathbf{R}\})$ on the other side. The highest physical dependability and computational cost have "quantum" interatomic potentials which take into account the details of electronic properties of the system, meanwhile the classical interatomic potentials are fitted to certain physical properties (elastic properties, phononic dispersion curves, etc) and are very effective

for massive calculations. The scheme 2.2 summarizes the potential's "hierarchy"

Next comes the question, how to model $E_{\rm pot}(\{\mathbf{R}\})$ in a given specific case the interactions between the particles. Empirical two-body potentials, such as Lennard-Jones (LJ), are quite reasonable for rare gas solids or Van der Waals molecular crystals, but not for most other solids. For metals, empirical many body potentials such as the Embedded Atom Model [48], the similar glue model [49], the Finnis-Sinclair potential [50], etc., are much more suitable than two-body forces. Many-body empirical potentials were developed also for such systems as valence semiconductors [51, 52] but here first principles simulations are generally much more appropriate [53].

In practice the integration of Eq.(2.2) is done numerically discretizing time. Among the possible integration schemes we have implemented the velocity Verlet algorithm, where error in positions is of order $\mathcal{O}(\delta t^4)$ and in velocities is of order $\mathcal{O}(\delta t^3)$. The method has been shown to have excellent energy-conserving properties even with long time steps [54].

The framework of molecular dymanics can be employed for purposes other than reproducing the time evolution of the system, and computing thermodynamical averages. Once the forces on the particles are computed, several "propagation" schemes can be devised: steepest descent, "smart" minimization (the velocities which have opposite signs with forces are nullified), or Langevin dynamics [55],etc. For instance, the steepest descent algorithm consists in minimizing $E_{\rm pot}(\{\mathbf{R}\})$ along a direction of a gradient, once the minimum is reached, the gradient is recalculated, a new minimum is sought along the new direction of the gradient. Another application of MD is to find the global minima using the simulated annealing technique. The system is initially heated up to high temperatures, then the kinetic energy is gradually removed from the system to reach hopefully the global minimum. The details can be found in Ref. [55]. In some particular simulations we used a damped dynamics at low damping. For these purposes we implemented Ermak's algorithm for Langevin dynamics [55]. The structure relaxation at 0 K is performed by "smart minimization". Further details can be found in Appendix A.

2.1.1 Ensembles and temperature control

In the classic MD technique (the simultaneous integration of Newtonian equations of motion) the system total energy is naturally conserved. By maintaining the volume constant, the simulation will produce a microcanonical ensemble (NVE), often referred to as Newtonian MD. Other important statistical ensembles are the isoenthalpic-isobaric (NPH) developed by Andersen [56], isobaric with variable cell (NPT) in framework of Parrinello-Rahman method [57], and the canonical (isokinetic) (NVT) ensemble. One way to implement the latter is to couple the system to an external thermal bath and control the temperature through the so-called Nosè-Hoover thermostat [58]. More commonly, the temperature control is accomplished simply by velocity-rescaling:

$$\mathbf{v}_{new} = \mathbf{v}_{old}\sqrt{T_{inst}/T_{old}} \tag{2.3}$$

We carried out both microcanonical and canonical simulations. In canonical (NVT) runs, temperature was controlled by velocity-rescaling [59] and only rarely by a Nosè-Hoover thermostat. We did not resort to (NPT) runs since we deal with surfaces. Moreover our simulations were mainly conducted in the vicinity of melting point where fluctuations become large and isobaric ensemble has much bigger errorbars than the isochoric one.

Despite the size and time limitations imposed by long range forces, great care was taken to run simulations long enough for a clear equilibration, typically 100÷300 ps, but longer when required.

2.1.2 Boundary and initial conditions

One of the delicate questions in MD simulations of charged systems are the choice of boundary conditions (BC). One can highlight three types: (a) *Rigid/fixed* BC. The boundary atoms coordinates are fixed / the forces acting on them are nullified. It is usually supposed that the number of the fixed atoms is a negligible fraction of the total system. Therefore the simulation supercell's size should be large. (b) *Free* BC. The boundary atoms are permitted to move accordingly to their dynamics. In this case the system is treated as a cluster in vacuum. (c) *Periodic* BC. The atoms are placed in periodically repeated supercell, keeping the total number of atoms constant per cell. This treats the system as a periodic solid.

The periodic boundary conditions(PBC) exclude the existence of the long wavelength fluctuation (for instance, it is not possible to model the critical point of the liquefied gas) and might have some artificial effects on the dynamics of liquid systems nevertheless it is the best way of modelling the macroscopic bulk systems with a moderate computational effort.

In our simulations we used periodic boundary conditions(PBC) with minimum image convention(MIC), i.e. each atom of the 'central' supercell interacts only with the closest image of all other particles in neighboring cells. Simulation of surfaces are commonly done in a slab geometry with periodic boundary conditions in x, y and free motion along z. In order to minimize spurious slab effects at high temperatures, the lateral box size must be adjusted to match the mean lattice parameter at any desired temperature. The first few bottom layers can be assumed to be rigid in their bulk-like positions to mimic the contact with a semi-infinite slab. In our case, we will repeat slabs periodically along z, separating them with a suitable amount of vacuum, as specified later below. In some slab simulations in order to mimic semi-infinite bulk we have used rigid boundaries.

The velocities initialization is done using the Maxwell-Boltzmann distribution at the desired temperature. The total linear and angular moments are set to zero:

$$\begin{aligned} \mathbf{P} &= \sum_{i}^{N} m_i \mathbf{v}_i = 0 \\ \mathbf{L} &= \sum_{i}^{N} m_i \mathbf{r}_i \times \mathbf{v}_i = 0 \end{aligned}$$

The atomic initial positions are randomized from the idealized lattice positions before starting the dynamics to speed up the equilibration process.

2.1.3 Model potentials for alkali halides

Alkali halides are among the simplest solids and have been therefore studied for a very long time. Born [60] and followers established quite early that many properties of these crystals could be basically understood by means of simple two-body potentials. The basic ingredients of these potentials are (1) the long-range Coulomb interactions between ions, (2) the short-range repulsion between the ion cores when they get too close. The straightforward implementation of these ingredients was introduced by Born and Mayer [61]. A significant improvement of the basic model was achieved by Born, Mayer and Huggins [62], who added Van

der Waals and dipole-quadrupole induced terms. All alkali halides were carefully parameterized by Fumi and Tosi [63]. A more realistic but computationally expensive description is done by introducing polarizable potentials that eliminate some of the residual unrealistic features of the rigid ion potentials. There is a vast literature on the bulk properties for solid and liquid alkali halides [64, 65, 66].

In a first approximation alkali halides are two-component mixtures of atomic anions and cations which interact through a spherically symmetrical potential. The unusual features of ionic crystals are the infinite range of the potential interactions, which causes the long-range structural correlations, and the strength of the attractive cation-anion interaction, which cause the presence even in liquids sharp peaks in the corresponding radial distribution function (i.e. long-lived cage structure around each atom). The simplest model for a molten salt is the *restricted primitive model*, in which ions are modelled by hard spheres, all with the same diameter, and with unit positive or negative charges Z_i at the center of each sphere:

$$v^{RPM}(r_{ij}) = \frac{Z_i Z_j}{r_{ij}} + v^{HR}(r_{ij})$$

$$v^{HR}(r) = \begin{cases} \infty & (r < \sigma) \\ 0 & (r \geq \sigma) \end{cases}$$

The first term is simply a Coulomb potential, the second term is the hard-sphere potential. The RPM model was studied among others by Dietrich [67], Bresme [68] and Fisher [69]. More sophisticated rigid ion models are the Pauling potentials, the (BMH) Fumi-Tosi potentials (see below), the Varshni and Shukla [70] type of potentials.

Born-Mayer-Huggins rigid ion potentials

It would be nice to use the best available potentials—those that include polarization effects—for our simulations. However polarization forces, though not negligible for the quantitative description of molecules, low-density ionic fluids, and other properties, appear to be less relevant in the context of the melting transition [71]. This is fortunate, because studies related to melting require simulations sizes and times that are difficult to attain with polarizable potentials. Here we adopt the Born-Mayer-Huggins-Fumi-Tosi (BMHFT) model, whose greater simplicity allows a much more extensive computational exploration of the melting and wetting properties. Consequently NaCl was modelled by the classic pair-

wise BMHFT rigid ion potential [63]:

$$V(r_{ij}) = \frac{Z_\alpha Z_\beta}{r_{ij}} + A_{\alpha\beta}\exp(-Br_{ij}) - \frac{C_{\alpha\beta}}{r_{ij}^6} - \frac{D_{\alpha\beta}}{r_{ij}^8}. \tag{2.4}$$

The α and β stand for either $+$ or $-$, Z_α and Z_β are the ionic charges ($+1$ for Na and -1 for Cl), the first term is the Coulomb interaction energy, the second is the short-range Pauli repulsion, and last two terms are induced dipole-dipole and dipole-quadrupole van der Waals interactions. The parameters for Na and Cl are reported in the table 2.1.

	Na-Na	Cl-Cl	Na-Cl
A (eV)	424.097	3488.998	1256.31
B ($Å^{-1}$)	3.1545	3.1545	3.1545
C (eV $Å^6$)	1.05	72.5	7.0
D (eV $Å^8$)	0.499	145.427	8.676

Table 2.1: Fumi-Tosi parameters of Born-Mayer-Huggins potential for NaCl. From Ref. [66]

Polarization effects

Polarization effects are normally incorporated into the simulations of ionic systems via the shell model. The electron cloud is treated as a spherical shell connected to the center of mass of an ion with a spring. More elaborated models developed recently employ potentials which include the polarization effects using either multipole expansions [71] or the distortable ion model [73]. One effect of ionic polarization in a vibrating crystal is to reduce the splitting of the longitudinal and transverse optic bands. The difference arises from the fact that the longitudinal and transverse modes give rise to different long-range fields in the limit $\mathbf{k} \to 0$. In a primitive model of the crystal the LO-TO splitting at the Brillouin zone center obeys by the Lyddane-Sachs-Teller relation:

$$\frac{\omega_{LO}^2}{\omega_{TO}^2} = \frac{\epsilon_0}{\epsilon_\infty} \tag{2.5}$$

where ω_{LO} and ω_{TO} are the longitudinal and transverse optic mode frequencies in the limit $\mathbf{k} \to 0$, ϵ_∞=1 for the rigid ion potentials, whereas for crystalline NaCl ϵ_∞=2.33 [74]

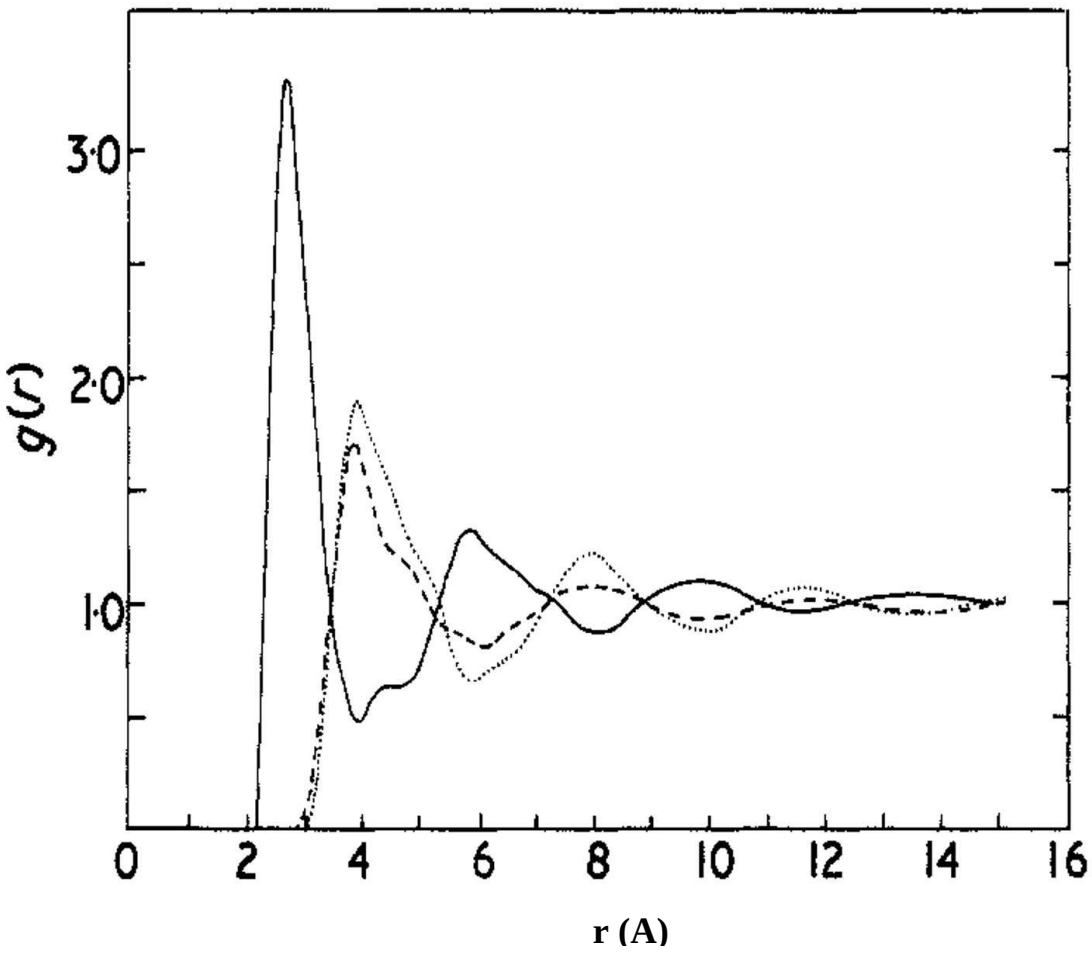

Figure 2.3: Experimental radial distribution function: g_{++} (dashed), g_{+-} (solid),g_{--} (dotted) of liquid NaCl. From Ref. [72]

Below we present a brief comparison of calculated surface energies and relaxation effects on NaCl(100) obtained within different approximations at 0 K (see Table 2.1.3). One can see in particular that the Fumi-Tosi potential provides a good estimation of γ_{SV} although the relaxation effects due to the polarization are absent.

Despite their good quality the main disadvantages of the RPM and rigid ion potentials are their inability to reproduce dynamical features such as the phonon dispersion curves in ionic crystals, and the artificial similarity of like pair distribution functions g_{--} and g_{++} in fluids absent in experiments (see Fig. 2.1.3). That may be cured by the implementation the more sophisticated ion potentials calculated from first principles, e.g. shell models or multipole expansion models.

2.1.4 Pressure and surface stress calculation

The pressure tensor of a fluid is the negative equilibrium average of the microscopic stress tensor. It is composed of two parts: a kinetic part that arises from the linear momentum of the molecules and a configurational part that arises from interatomic forces. The system pressure is calculable through the Clausius virial theorem:

$$pV = Nk_BT + \frac{1}{3}\left\langle \sum_{i=1}^{N} \mathbf{r}_i \cdot \mathbf{F}_i \right\rangle \tag{2.6}$$

$$\tag{2.7}$$

For a pairwise interaction potential $U(r_{ij})$ the above expression becomes:

$$pV = Nk_BT - \frac{1}{3}\left\langle \sum_{i=1}^{N} \sum_{j>i} r_{ij} \frac{dU(r_{ij})}{dr} \right\rangle \tag{2.8}$$

In the case of many-body interactions the pressure profiles can be calculated by a method of planes [77], or by a modified virial approach [78].

Surface stress and surface free energy at fluid interfaces

The surface excess quantities deal with *mechanical* equilibrium (balance of forces) and *chemical* equilibrium (balance of mass transfer) and should be independent on the choice of the dividing surface. In this thesis we will often refer to the surface tension γ of a homogeneous liquid. Following by Ono and Kondo [79] it is useful to review its several determinations (valid for liquids):

Mechanical:

$$\gamma = \int_{-\infty}^{\infty} (p_\perp - p_{||}) dZ$$

Physical value	BMHFT	Madden	Ab initio	Experiment
$\gamma_{\mathrm{SV}}(\mathrm{mJ/m^2})$	191	242	171	∼276
Δ Cl-Na (Å)	0.028	0.061	0.0869	0.0874

Table 2.2: NaCl(100) at 0 K. Our calculation of surface free energy and $\Delta = z_{Cl} - z_{Na}$ buckling, according to ab-initio, BMHFT and polarizable potentials [71, 75] and experiment [76].

where $p_{||}$ and $p_{\perp}$ are the tangential and normal components of the pressure tensor. Isotropy in the xy-plane implies $p_{||} = p_x = p_y \neq p_{\perp}$.

Statistical:

$$\gamma = -\frac{1}{4}\int_{-\infty}^{\infty} dZ \int d^3\mathbf{r} \sum_{\alpha\beta} \frac{x^2 + y^2 - 2z^2}{r} f_{\alpha\beta}(r) g^{(2)}_{\alpha\beta}(\mathbf{r}; Z)\rho(Z)$$

where $f_{\alpha\beta}(r)$ is the pairwise force between α and β species at relative position r. The surface tension evaluation in this case completely depends on the two body distribution function $\mathrm{g}^{(2)}_{\alpha\beta}(\mathbf{r}, Z)$ in the interface region.

Numerical simulation: Straight implementation for the surface stress calculation in MD simulations.

$$\gamma = -\frac{1}{4L_xL_y}\left\langle \sum_{i,j} \frac{x_{ij}^2 + y_{ij}^2 - 2z_{ij}^2}{r_{ij}} f(r_{ij}) \right\rangle \tag{2.9}$$

where L_x and L_y are the in-plane simulation cell sizes.

Surface stress and surface free energy at solid interfaces

In contrast to the fluid case, surface free energy and surface stress are not identical in solids. The work done dW in creating a new surface dA by applying uniform stress σ on area A is simply

$$dW = \sigma dA = d(\gamma A) = dA(\gamma + \frac{\partial \gamma}{\partial A} A)$$

where γ is the solid surface free energy. Therefore the thermodynamic relation between surface free energy and surface stress per unit area can expressed as:

$$\sigma = \gamma + \frac{\partial \gamma}{\partial A}$$

as first was established by Shuttleworth [80]. Liquids do not support shear, hence their surface stress is unaffected by any bulk deformations. On the other hand, solids are rigid and a bulk strain generally changes the surface properties too, whence $\frac{\partial \gamma}{\partial A} \neq 0$. As a consequence, all methods given above do not work for a solid. As will be explained later, we will recourse to thermodynamical integration to calculate γ_{SV}.

2.1.5 Ewald summation

The presence of Coulomb long-range forces severely limits the sizes of our simulated systems (upper limit is $\sim$ 30000 atoms). Since long range forces are crucial, we rejected the possibility of spherical truncation [81] and implemented the Ewald summation technique [82]—the most accurate and widely used method nowadays.

In our case we have an electrically neutral system with a certain distribution of point charges q_i in real space. The total charge density can be expressed:

$$\rho(\mathbf{r}) = \sum_{\mathbf{n}} \sum_{i} q_i \delta(\mathbf{r} - \mathbf{r}_i - \mathbf{n})$$

yielding to the total electrostatic energy

$$V(\mathbf{r}) = \sum_{\mathbf{n}} \sum_{i<j} \frac{q_i q_j}{|\mathbf{r}_{ij} - \mathbf{n}|}$$

over the simulation cell and its image neighbors, where $\mathbf{n} = (n_x L, n_y L, n_z L)$, L is the supercell's size and n_x, n_y, n_z are integers. The Ewald summation [83, 54] method allows to recast Coulomb interactions into two rapidly converging series: one—in real space and the other—in Fourier(reciprocal) space. In real space the point charges q_i are screened by the electrostatic clouds of opposite charge placed on the ions. The new distribution is short-range rapidly convergent series. In reciprocal space the charged clouds with the same charge as the original point charges are artificially added to compensate the effect of real space electrostatic clouds. Finally the self-interaction correction term due to the point charge-compensating cloud repulsion is substracted. The surrounding cloud has a form of a gaussian:

$$\rho_\star(\mathbf{r}) = -q_i \left(\frac{\alpha}{\pi}\right)^{3/2} e^{-\alpha r^2} \tag{2.10}$$

Parameter α controls the efficiency of the method. The total electrostatic energy is given by the following formula:

$$\begin{aligned} V_{\text{Ewald}}(\mathbf{r}) &= \frac{1}{V} \sum_{\mathbf{k}\neq\mathbf{0}} \frac{\exp(-k^2/4\alpha^2)}{k^2} \left[\sum_j q_j \exp(-i\mathbf{k}\cdot\mathbf{r}_j)\right] \left[\sum_j q_j \exp(i\mathbf{k}\cdot\mathbf{r}_j)\right] \\ &+ \frac{1}{4\pi} \sum_i \sum_{j>i} \frac{q_i q_j}{r_{ij}} \text{erfc}(\alpha r_{ij}) - \frac{\alpha}{4\pi^{3/2}} \sum_i q_i^2 \end{aligned} \tag{2.11}$$

The first term corresponds to the reciprocal-space summation over **k**-vectors. The second term is the direct-space summation; $\text{erfc}(x)$ is the complementary error

function:

$$\text{erfc}(x) = 1 - 2\pi^{-\frac{1}{2}} \int_0^x e^{-t^2} dt$$

The last term represents the self-correction. The scaling with particles number is $\mathcal{O}(N^{3/2})$.

An effective modification of the method is an extensive optimization technique particle-mesh Ewald (PME) [84]. It developed to perform fast and reliable simulations rely upon an evaluation of the reciprocal-space term using a fast Fourier transform (FFT). A 3D grid filling the supercell Cartesian space is constructed. The point ionic charges are interpolated over the grid and the corresponding charge distribution $\rho(\mathbf{r})$ is computed. Employing FFT, the transform of the charge distribution $\rho(\hat{\mathbf{k}})$ is obtained. Next, the long-range contribution of the electrostatic potential is estimated $\hat{V}(\mathbf{k}) = \hat{G}(\mathbf{k})\hat{\rho}(\mathbf{k})$ at the various points of the 3D grid, where $\hat{G}(\mathbf{k})$ is the so-called influence function defined by $\hat{G}(\mathbf{k}) = \hat{\lambda}(\mathbf{k})/k^2$ in which $\lambda(\mathbf{r})$ is a distribution that depends upon the sole geometrical characteristics of the simulation cell. Electrostatic forces are determined by numerical derivation of the potential. Finally the electric field and the potential are interpolated back from the grid towards the position of the particles. This scheme has a computational effort of $\mathcal{O}(NlnN)$.

For the slab geometry which we generally use the conventional Ewald summation technique is not valid anymore since there is no periodicity in one of the three dimensions. Parry *et al* [85] introduced a 2D Ewald summation technique(EW2D), whose direct use is found to be computationally expensive [86]. The other algorithms like precalculated tables [87] essentially improve that performance but are not suitable for our type of problem where we need careful comparison and substraction between bulk and slab systems (see Section 4.2.1).

Another solution is to apply the conventional EW3D to a simulation cell elongated in z direction so that a sufficiently large empty space between periodic replicas in z is created. The inclusion of empty space between slabs into the unit cell is necessary to avoid an artificial influence from the periodic images in z direction. Spohr [87] compared the results from the simulations that used EW3D method with those from the EW2D method. He concluded that the EW3D converges to EW2D when the vacuum thickness in the simulation cell is rather large. However the correlated fluctuations of surface dipole moment remain important source of errors.

A good solution was found by Yeh and Berkowitz [83]. The so-called 3D Ewald

sum with surface dipole moment correction (EW3DC) $\frac{2\pi}{3L^3}\left|\sum_i q_i \mathbf{r}_i\right|^2$ reduces the conventional 3D Ewald sum to the 2D Ewald sum. If the surrounding medium has an infinite dielectric constant ($\varepsilon(\omega) = \infty$) the surface term vanishes. It is equivalent to the "tin foil" or conducting boundary condition. Instead if the dielectric constant is finite ($\varepsilon(\omega)$ = 1 like in vacuum) the surface term becomes essential and vacuum boundary conditions take place.

In our repeated slab 3D Ewald scheme, a large vacuum thickness of order 100Å separating the slabs is used in order to reduce spurious electrostatic couplings of instantaneous fluctuating dipoles in liquid surfaces facing one another across the vacuum gap. Moreover, we use EW3DC method for better convergence with conducting boundary conditions in the tangential directions and with insulating or vacuum boundary conditions in the direction normal to the surface (see Ref. [54]). In development version of the code we have also used PME method [84].

2.1.6 Velocity autocorrelation function and effective harmonic approximation

In a solid the main contribution to the entropy comes from the vibrational entropy. In bulk as well as in the surfaces the vibrational free energy is of essential importance for phase transitions. It can be calculated approximately within the quasi-harmonic approximation [88] or self-consistent phonon approximation [89, 90]. The harmonic or quasi-harmonic approximations are such that each atom is moving in a parabolic potential well whose curvature is a variational parameter, calculated variationally with all other atoms rigidly fixed to their mean lattice sites. In the self-consistent phonon method the concept is the same, but the parabolic well is calculated by regarding the other atoms as moving. By the Gibbs-Bogoliubov inequality the free energy of the model lattice is always greater than the true free energy but the fitted best parameters are obtained from the minimum free energy difference. The details can be found in [60].

In our study we needed calculate a surface vibrational entropy of solid NaCl. For this purpose we developed a slightly different approach—an *effective* harmonic approximation. Unlike the quasiharmonic, or self-consistent harmonic methods, our approach is not self consistent, but uses input from simulations (Fig. 3.3) that makes it certainly much more accurate. From the simulations we extracted the vibrational spectrum as the velocity autocorrelation temporal Fourier transform [91]. Treating this spectral density $D(\omega)$ as a set of the quantum os-

cillators and calculated the free energy the F^{vibr} in the harmonic approximation, which finally yields:

$$F^{vibr}(T) = k_B T \int d\omega D(\omega) \log[2 \sinh(\hbar\omega/2k_B T)] \tag{2.12}$$

2.1.7 Free energy and thermodynamic integration

The thermodynamic potentials such as the free energy, which determine the principal thermodynamic properties unfortunately cannot be directly extracted from MD evolution, which provides just mechanical quantities. In particular, the internal energy is a mechanical quantity, but entropy is not. To evaluate thermodynamical potentials it is necessary to apply a specific algorithm like weighted histograms [92], thermodynamic integration [54] and more recent metadynamics [93]. The thermodynamic integration in particular is a very common, widely used technique and has found many applications in computational physical chemistry. The necessary components of the thermodynamic integration are the free energy of a *reference state* F^{ref} (e.g., the free energy of ideal gas for liquids or Einstein harmonic crystal for solids at low temperatures) and the free energy *difference* between the reference state and the desired state F^{fin}. This difference is expressed as an integral of a certain coupling parameter λ varying from 0 ($F(\lambda = 0) = F^{ref}$) to 1 ($F(\lambda = 1) = F^{fin}$):

$$\delta F = \int_0^1 d\lambda \left\langle \frac{\partial E(\lambda)}{\partial \lambda} \right\rangle_\lambda \tag{2.13}$$

where $E(\lambda)$ is the system energy. An important requirement is the reversibility of the integration path. Some typical examples are the calculation of energy barrier in chemical reaction [94], or the free energy difference at structural transitions [95], or the two-phase coexistence point [96]. In this thesis we exploited the thermodynamic integration technique in order to calculate the solid surface free energy near the melting point. We calculated γ_{SV} through thermodynamic integration [54] using the following general relation:

$$\left(\frac{\partial(F/T)}{\partial(1/T)} \right)_{N,V} = E, \tag{2.14}$$

where F is the free energy and E the internal energy. Further in Section 4.2.1 we will discuss the method and the main results in detail.

Chapter 3

Bulk NaCl properties molecular dynamics simulation

3.1 Description of solid alkali halides

With the choice of potentials and techniques described in Ch.2, we proceeded to conduct MD simulations of NaCl as a function of temperature. Bulk systems were studied at constant volume with cubic simulation cells comprising up to 10000, but more typically 3000÷5000, NaCl molecular units. First of all, we verified how faithfully the bulk properties of solid and liquid NaCl are reproduced by the BMHFT potentials. Thermal expansion of the solid is dictated by the increase of equilibrium lattice spacing at zero pressure as a function of temperature. We performed several simulations at constant temperature and volume, and computed the equilibrium lattice spacing by seeking the cell size that yielded vanishing pressure at each given temperature. The overall interpolated result is shown in Fig. 3.1, where it is compared with experimental data from various sources [97]. The temperature dependent cell size obtained in this manner was enforced in all subsequent simulations involving solid NaCl. The calculated room temperature equilibrium lattice spacing and linear expansion coefficient $\alpha = (3V)^{-1}dV/dT$ were 5.683 Å and 40.5·10^{-6} K^{-1} respectively (5.635 Å and 38.3·10^{-6} K^{-1} are the experimental values [97]).

At higher temperature, notably above 600 K, the anharmonicity is seen to get stronger, and expansion becomes somewhat nonlinear. Of course, our procedure continues to work, and is in fact very accurate at these higher temperatures. The

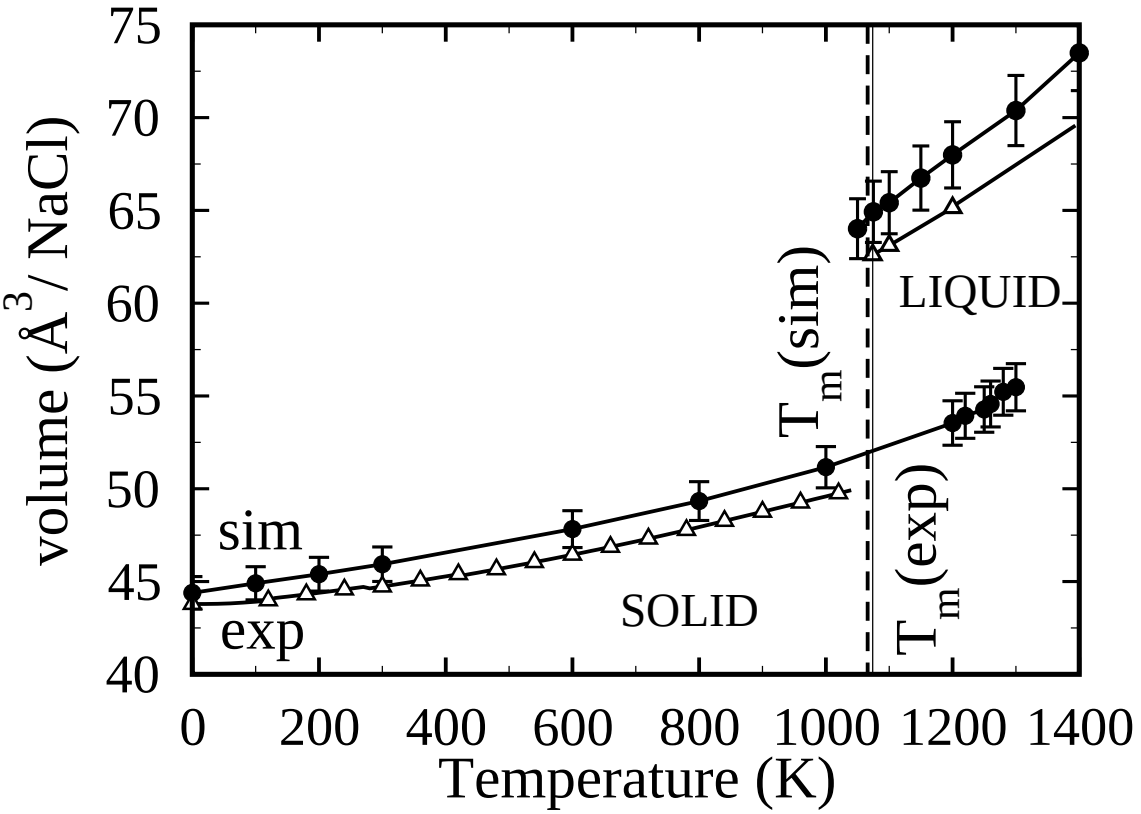

Figure 3.1: NaCl volume expansion vs temperature. The data from our simulations (filled circles) interpolated (solid line) up to the melting temperature T_{M} and above are very close to the experimental ones (empty triangles). The BMHFT volume change and the melting temperature are in perfect agreement with experimental data from Ref. [97].

simulated bulk solid remains locally stable and does not spontaneously melt (at least for our cell sizes and for times within 200 ps) until a maximum temperature $T_{\mathrm{S}} \sim 1305$ K. This maximum bulk metastability temperature, necessarily higher than the ordinary melting temperature T_{M}, approximates the "spinodal" temperature of bulk NaCl, defined as the point where the solid phase ceases to be a local free energy minimum (for example by losing its mechanical stability). As we will see further below, this bulk spinodal temperature is indeed well above the melting temperature, precisely $T_{\mathrm{S}} \sim T_{\mathrm{M}}$ + 240 K in the BMHFT model.

Root mean square displacements $(\overline{\Delta r^2})^{1/2}$ (RMSD) of Na^+ and Cl^- ions were extracted from the high temperature bulk NaCl solid simulations. As shown in Fig. 3.2 the value at 1066 K is 0.61 Å for Na and 0.59 Å for Cl, comparable with experimental estimates of 0.5 Å and 0.48 Å at the melting point [98]. The corre-

sponding calculated Lindemann ratios (see Section1.2)at 1066 K $\delta = (\overline{\Delta r^2})^{1/2}/a$, ($a$ is the interatomic distance) are 20% and 22% , compared with experimental estimates at T_{M} obtained from Debye-Waller factors of 17% and 20% [98]. BMHFT potentials appear to slightly overestimate the thermal vibration amplitudes, but we note that the uncertainties in the experimental procedure where RMSDs were extracted seem much larger than this discrepancy. In any case the RMSD values are very much larger than the typical values between 10% and 15% of the Lindemann ratio for most solids at T_{M}. This large overshoot of the alkali halide bulk Lindemann ratios can be rationalized by noting that whereas large thermal vibrations may very effectively destabilize atoms inside its bulk solid cage when interatomic forces are short ranged, they will much less effectively do so when forces are long range as is the case in strongly ionic solids. Simulations show that high temperature NaCl is in the BMHFT model a strongly vibrating, strongly anharmonic, and yet unusually stable solid. As we shall show later, the same is true of the NaCl(100) surface.

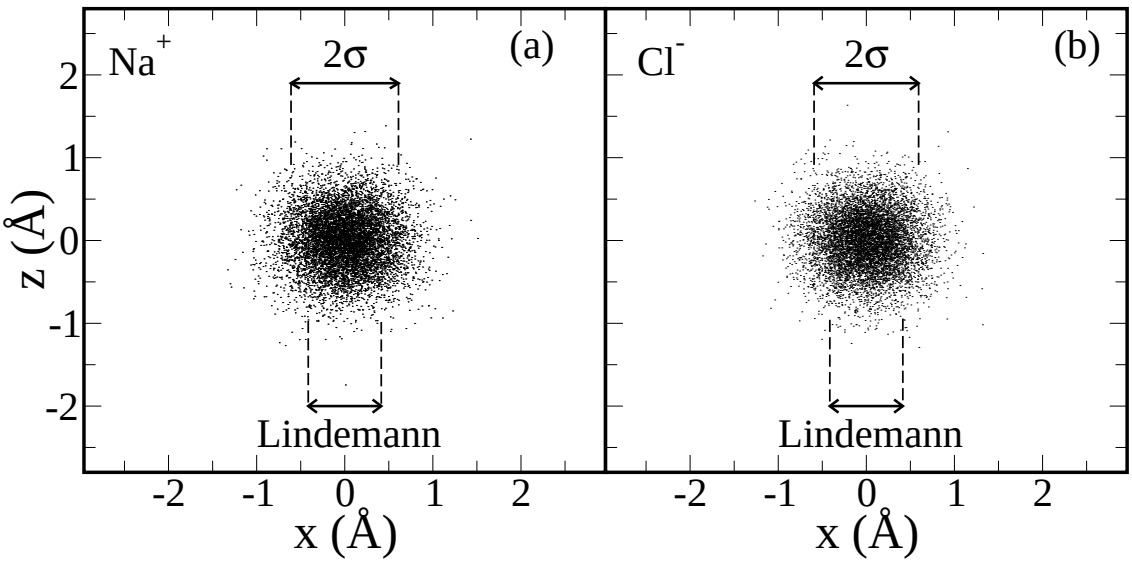

Figure 3.2: The instantaneous displacements of the Na^+(a) and Cl^- (b) ions in simulated bulk NaCl at 1066 K (bulk melting point of the Tosi-Fumi model). The displacement distributions are well fit by gaussian distributions whose widths are $0.22 \times a$ and $0.2 \times a$ where a is the interatomic distance. Much smaller widths are expected from the Lindemann melting criterion $(\overline{\Delta r^2})^{1/2} \sim 0.15 \times a$.

Following the procedure discussed in Section 2.1.6. The vibrational spectral properties of warm NaCl can also be easily extracted, by Fourier transforming

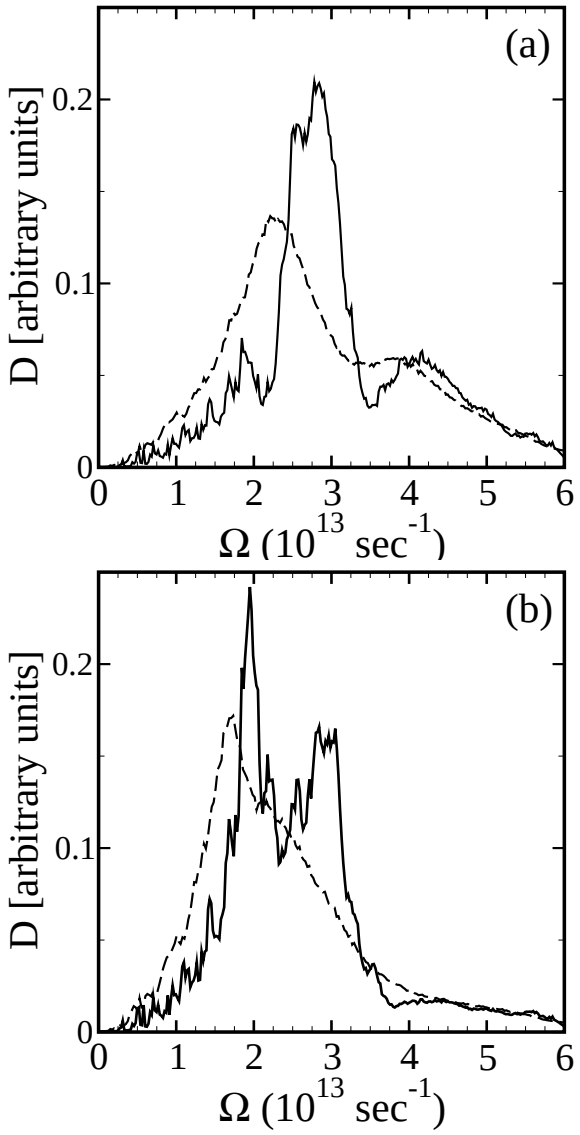

Figure 3.3: Vibrational density of states of bulk solid NaCl for (a) Na^+ and (b) Cl^- ions. Comparison between 300 K (solid line) and 1000 K (dashed line) indicates a considerable vibrational softening.

the velocity-velocity correlation functions:

$$V_{\mathrm{Na}}(\omega) = \frac{1}{2\pi}\int_0^\infty dt\, e^{i\omega t}\,\langle \mathbf{v}_{\mathrm{Na}}(t)\cdot\mathbf{v}_{\mathrm{Na}}(0)\rangle\,, \tag{3.1}$$

and similarly for Cl. The two spectral densities $V_{\mathrm{Na}}(\omega)$ and $V_{\mathrm{Cl}}(\omega)$ extracted at 300 K and at 1066 K are shown in the Fig. 3.3.

Generally, we note that our simulated vibrational spectra do not compare well in the details – even if not unreasonably in their gross features – with the more re-

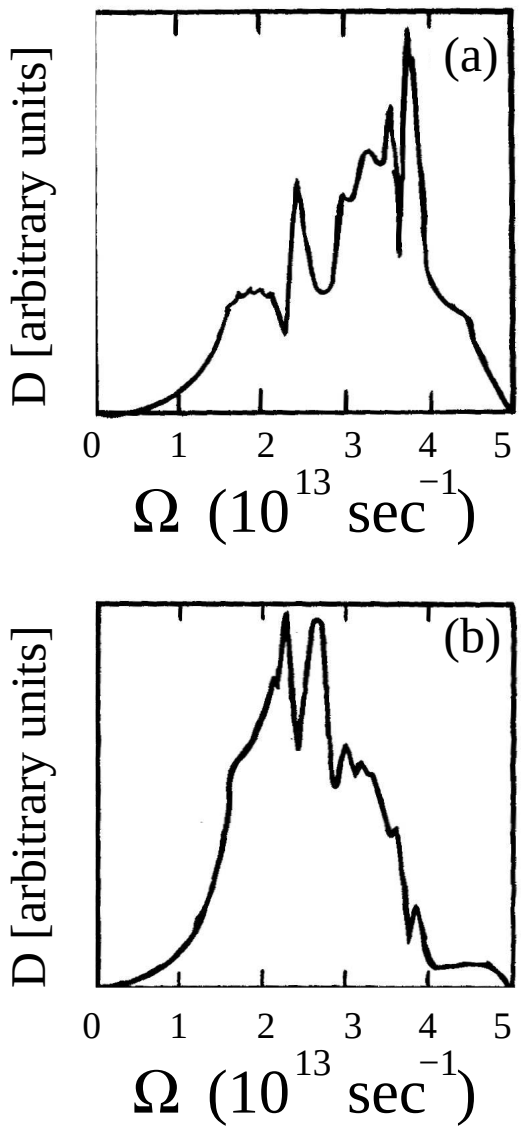

Figure 3.4: Realistic vibrational density of states of solid NaCl at low temperatures projected on (a) Na^+ and (b) Cl^- ions. From Ref. [99]

alistic spectral densities of Ref. [99] taken from the literature, and corresponding to very accurate shell model fits to experimental phonon spectra (Fig. 3.4). The rigid ion model is notoriously too crude to reproduce fine features as the detailed vibrational spectra, heavily affected by non rigid ion effects [100]. Nonetheless it is not unreasonable to believe that the overall temperature evolution of spectral densities can still be taken as representative of the real situation. The high temperature spectra show a considerable anharmonic softening and broadening relative to the room temperature ones.

3.2 Bulk liquid NaCl: the structure of the molten salt

Simulations of bulk liquid NaCl were conducted in close analogy to those of solid NaCl. In particular, the cell volume was adjusted isotropically to ensure vanishing pressure at every temperature. Our overall description of the liquid is very similar to that provided by many long standing studies [24]. The calculated liquid molecular volume is shown along with experimental values in Fig. 3.1. The calculated volume expansion of 27% at melting compares very well with 26% from experiment. The internal structure of the liquid, notably the Na-Cl, Na-Na and Cl-Cl radial distribution functions:

$$g(r) = \rho^{-1} \left\langle \sum_{ij} \delta(\mathbf{r} - \mathbf{R}_{ij}) \right\rangle, \tag{3.2}$$

quantities that are long well known, are well reproduced (Fig. 3.5) by the simulation. They exhibit the charge correlation typical of molten salts, the first peak of $g_{+-}(r)$ giving a typical Na-Cl distance in the liquid of 2.6 Å, about 10% shorter than in the solid.

From the pair correlation functions, we may calculate the bulk liquid coordination number:

$$N_{\pm} = \rho \int_0^{r_m} 4\pi r^2 g_{+-}(r) dr, \tag{3.3}$$

where the upper integration limit corresponds to the first local $g_{+-}(r)$ minimum, $r_m = 4.0$ Å. We find a coordination number N = 4.6 in liquid NaCl at 1066 K, to be compared with the much higher N = 6 coordination in the defect-free bulk solid. Experimental estimates of the liquid coordination number vary in a broad range from N = 4.7 [39] to N = 5.8 [65]. According to our simulation an ion in the liquid is surrounded by a cage consisting of only 4.6 ions of the opposite charge, albeit considerably closer than in the solid. For better understanding the nature of the effective ion cage in the liquid we studied the Na-Cl-Na and Cl-Na-Cl angular distribution in the bulk liquid:

$$P(\theta) = \left\langle \sum_{ijk} \delta \left(\theta - \arccos \frac{\mathbf{R}_{ji} \cdot \mathbf{R}_{jk}}{|\mathbf{R}_{ji}||\mathbf{R}_{jk}|} \right) \right\rangle, \tag{3.4}$$

where $|\mathbf{R}_{ij}|, |\mathbf{R}_{jk}| < r_m$. The result shown in Fig. 3.6 exhibits a main peak at 90° and only a weaker shoulder around 150°. A similar result for angular distribution function were obtained for KCl by Amini and Hockney [101, 102]. The dominant 90° peak indicates in particular that the local ionic cage surrounding an ion of

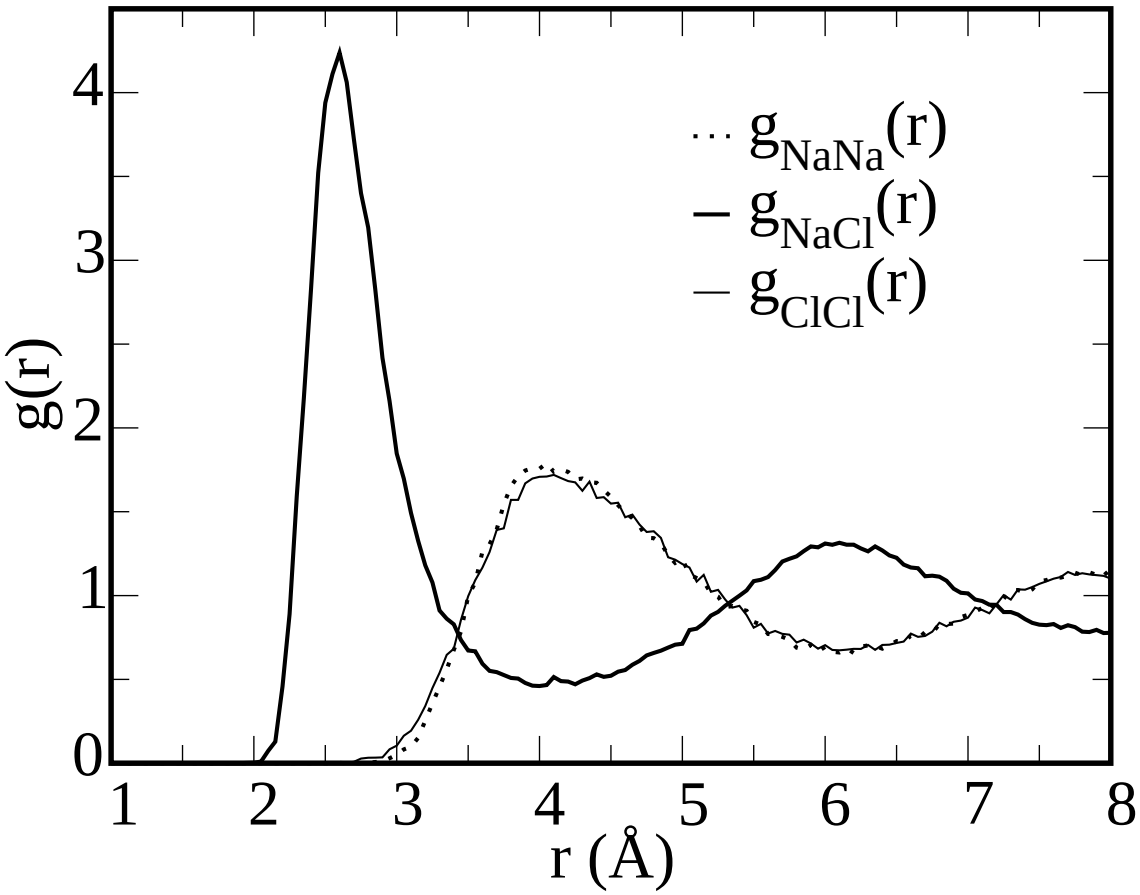

Figure 3.5: The partial radial distribution functions at T_{M}= 1066 K.

the opposite charge is, even in the liquid, still roughly cubic, or more precisely octahedral, as in the solid. The octahedral cage linear size is smaller by about 10% than that of the solid. The 4.6 surrounding ions are distributed on the 6 corners of this cage, which therefore contains on average about 1.4 vacancies.

The diffusion coefficient:

$$D = \lim_{t\to\infty} \frac{1}{6t} \left\langle \sum_i |\mathbf{R}_i(t) - \mathbf{R}_i(0)|^2 \right\rangle, \tag{3.5}$$

was also computed during simulations in order to check the general quality of description of the liquid. We found D = 10.53 $\cdot$ 10^{-5} cm^2/s at T = 1300 K, which compares well with experimental values like D = 8.6 $\cdot$ 10^{-5} cm^2/s at T = 1121 K [103], as well as with those from previous MD simulations, such as D = 9.5 $\cdot$ 10^{-5} cm^2/s at T = 1267 K [24].

Based on all the above we conclude that the BMHFT potential description of

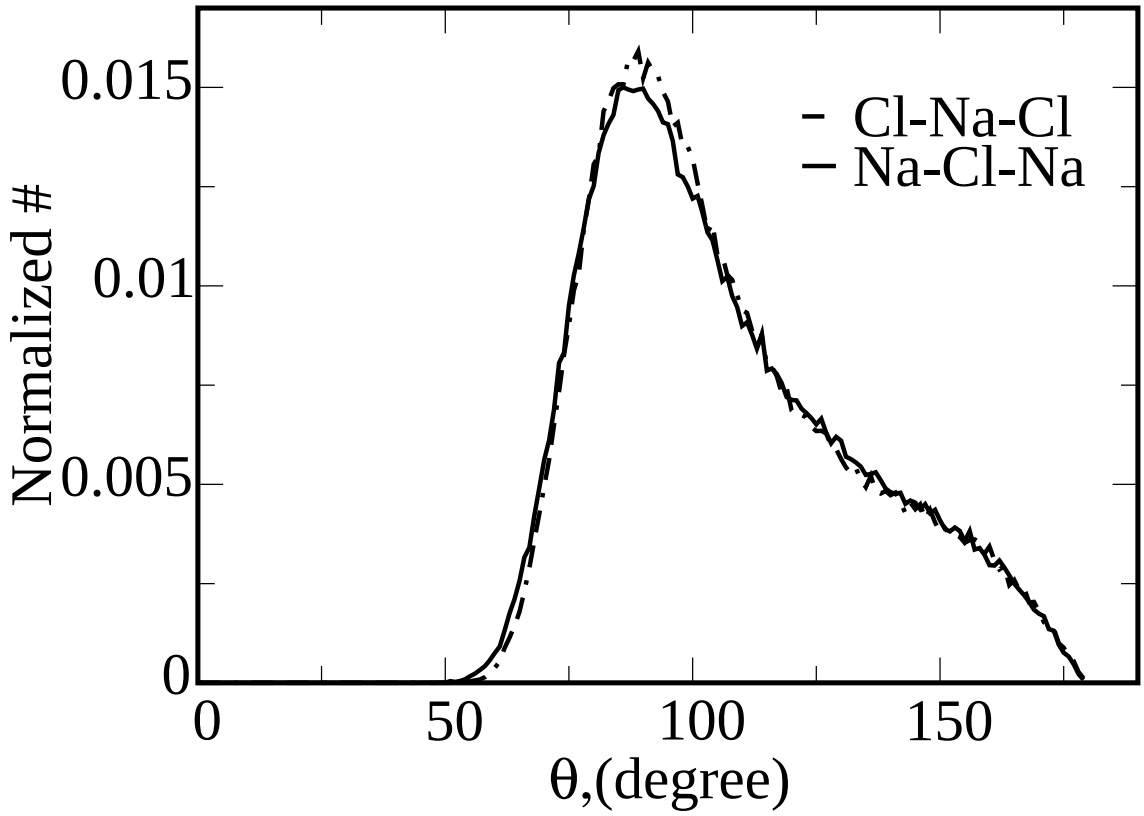

Figure 3.6: The angular distribution function of simulated liquid NaCl at T_{M}.

bulk liquid NaCl is on the whole very good.

3.3 Melting point

The melting temperature of the BMHFT model of bulk NaCl is obtained directly from simulations of solid-liquid coexistence at zero pressure. Strictly speaking the zero pressure melting temperature differs from the triple point temperature, which is slightly higher due to the finite triple point pressure. The triple point pressure is however only about 0.45 10^{-6} kbar, which for $dP/dT \sim 0.03$ kbar/K yields extrapolated difference of only about 10^{-5} K between the triple point temperature and the zero-pressure melting temperature, utterly negligible. At constant temperature, the interface in a bulk system which is roughly half solid and half melted (actually there are two SL interfaces because of periodic boundary conditions) will drift with simulation time one way or the other so long as the system is away from the melting temperature T_{M}, and will only remain station-

ary at $T = T_{\rm M}$. At constant energy, the average temperature $\langle T \rangle$ will instead slowly drift toward the melting temperature $T_{\rm M}$ [104, 105].

We started with a crystalline bulk made up of 2880 molecular units, a geometry comprising 6×6×20 conventional 4-molecule cubic NaCl cells along (x, y, z) respectively. Periodic boundary conditions (PBC) were assumed in all directions, and the volume was constant during each simulation. However, the cell size was adjusted with temperature, so as to enforce zero stress at each temperature, as detailed below. After equilibration in proximity of the presumed melting point ($T \approx 1100$ K) about one half of the 20 layers were melted by bringing them selectively at a higher temperature, while the remaining atoms in the solid phase are kept fixed on their positions. The liquid and the solid halves initially out of equilibrium were subsequently let evolve to their mutual equilibrium. The in-plane cell size, and with it the in-plane solid lattice spacing were kept fixed at their solid equilibrium value previously established for that temperature as shown in Fig. 3.1. The linear cell size in the z-direction perpendicular to the solid-liquid interfaces was subsequently adjusted after each equilibration so as to cancel the uniaxial stress normal to the interfaces, compensating in particular the solid-liquid volume expansion. When the system was finally equilibrated by means of canonical MD runs (see Fig. 3.7), we observed the anticipated drift of the solid-liquid interfaces in opposite directions at 1050 K and 1070 K, indicating that the melting temperature must fall in between (Fig. 3.8a).

To sharpen up our estimate of $T_{\rm M}$ we then carried out delicately selected microcanonical simulation runs between $E = -7.25$ and -7.2 eV/molecule. Our final result was $T_{\rm M}$= 1066 ± 20 K (Fig. 3.8b). The conservatively large error bar quoted is mainly due to a residual pressure uncertainty of ∼0.5 kbar. The real uncertainty is probably smaller, since we also found later that systems with free surfaces, and thus with a pressure more accurately close to zero, melt in bulk within 5 K of 1066 K. We also estimate that the error of $T_{\rm M}$ due to other factors, including small system size, and fluctuations, to be smaller than 20 K. For instance, the melting temperature of an unrealistically small system made of 6×6×4 molecules was found to be ∼ 1050 K. Finally our value of the melting temperature, obtained in a totally unbiased manner [106], is in essentially perfect agreement with $T_{\rm M}$ = 1064 ± 14 K independently obtained by thermodynamic integration by Frenkel's group [96].

The latent heat (enthalpy of melting) is estimated as the change of the internal energy at $T_{\rm M}$ and found to be 0.29 eV/molecule. The calculated entropy jump

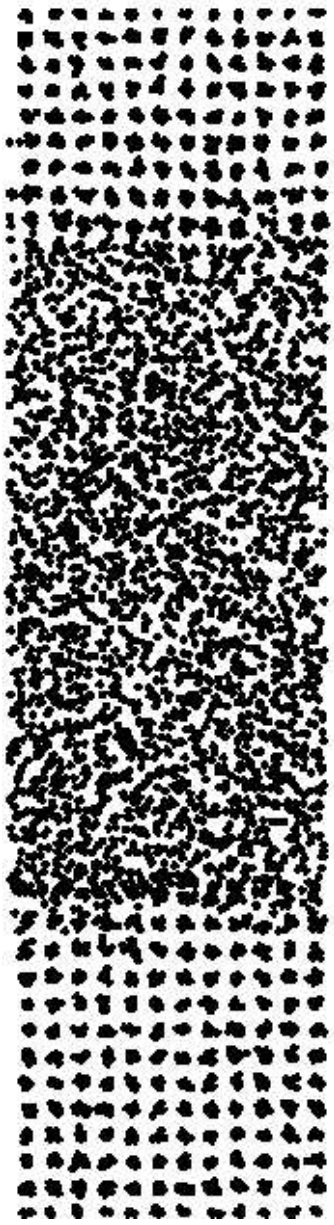

Figure 3.7: Simulated coexistence of bulk solid and liquid. Periodic boundary conditions on all sides.

at melting is thus $\Delta S_m = L/T_{\mathrm{M}} = 6.32 \pm 0.1\ k_B$/molecule. A slope of the melting line (Clausius-Clapeyron relation) $\frac{dP}{dT} = \frac{L}{T_{\mathrm{M}}(v_l - v_s)}$ of 0.0311 kbar/K is then obtained. All these calculated results are in quite good agreement with experimental data. The Section 3.5 yields a brief summary of the calculated values and their comparison with experiment.

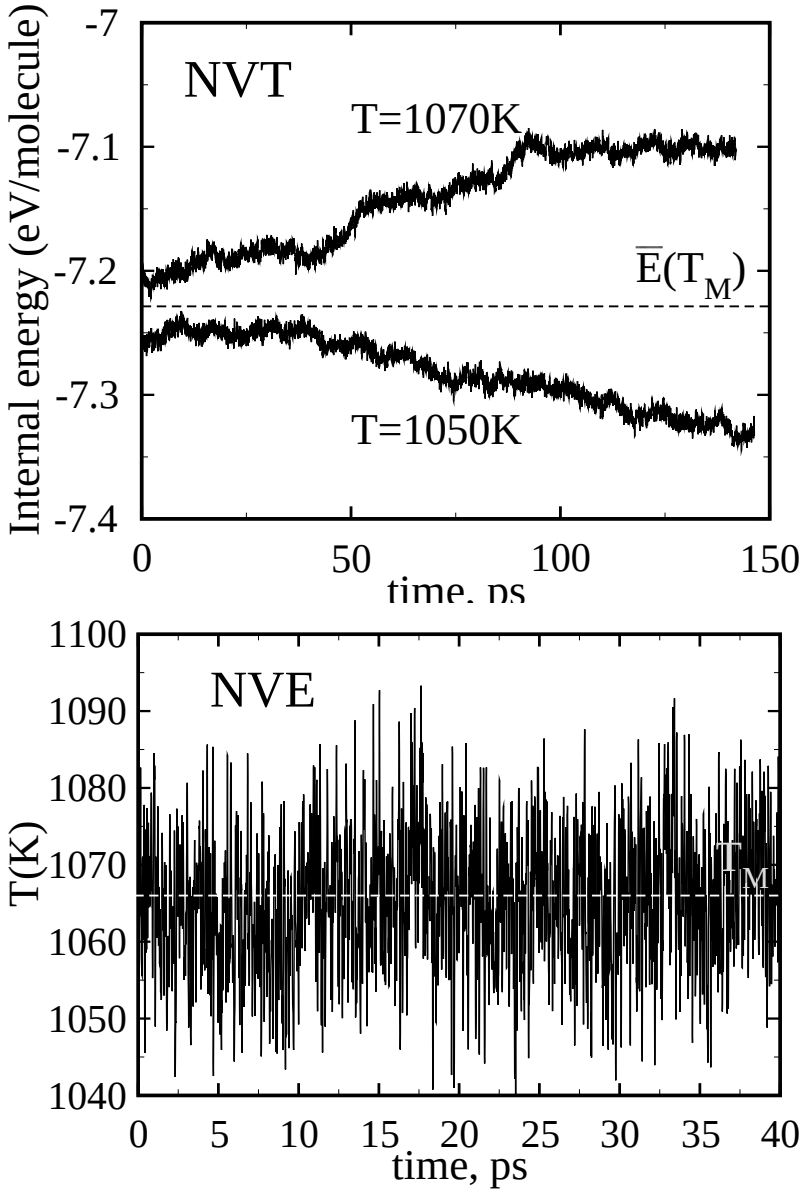

Figure 3.8: (a) Canonical evolution of the internal energy at liquid-solid coexistence. The decrease of internal energy at T = 1050 K indicates that the SL interface moves toward recrystallization. Conversely, the increase of internal energy at T = 1070 K indicates that the liquid phase grows at the expenses of the solid phase. The internal energy for the BMHFT melting point of bulk NaCl lies in between. (b) Final microcanonical run showing the exact location of the melting temperature.

3.4 Alkali halide vapors and sublimation

The highly ionic nature of alkali halides make them peculiar even in vapor. Diatomic alkali halide molecules have large dipole moments and therefore tend to

form associated vapor species. Molecular dimers have been detected in vapors of all the alkali halides; trimers and tetramers have been detected in some [107]. The presence of associated species leads to deviations from ideal gas laws which are too large to be described readily in terms of a virial expansion. The most successful treatment of alkali halide vapors considers them as ideal mixtures of different vapor species so that the total pressure p is the sum of the partial pressures of $i$mers p_i: $p = \sum_1^\infty p_i$ where i denotes the number of monomer units in the species. The total density of salt vapor is $(n/V)RT = \sum_1^\infty ip_i$ where n is the number of moles in the volume V. At $T_{\rm M}$ the NaCl vapor experimentally consists for 69% of molecules (N=1), 31% of dimers, (N=2) and a trace of trimers [107]. The corresponding vapor average is $\langle N_{\pm_V} \rangle \simeq 1.3$. The experimental equilibrium vapor pressure of NaCl at $T_{\rm M}$ is 345 μHg. As a consequence, NaCl(100) will sublime. Surface vacancies will form and existing surface steps will flow due to evaporation (and to re-condensation when working at solid-vapor equilibrium).

We did not carry out simulations for NaCl vapor, as it was not necessary and would have been impossible with the present method. The NaCl vapor would not be described well by the BMHFT potential (for instance the experimental equilibrium interatomic distance is 2.3609Å in monomers [108], while the BMHFT gives 2.30Å). We note that the time scale for evaporation or sublimation from the surfaces in simulation is a much slower one than that addressed here. The experimental rate of evaporation found from the empirical expression[109] valid for a variety of materials,

$$\log W = -4.234 + \log P_\mu + 0.5 \log \frac{M}{T} \tag{3.6}$$

where W - rate of evaporation in grams per square centimeter per second, M - gram-molecular weight, P_μ - vapor pressure in microns of Hg. For our typical 10×10 sized surface (200 surface NaCl units) of area around 3500 Å^2, and using an experimental vapor pressure the estimated evaporation rate is $\sim 1.7 \cdot 10^5$ sec^{-1}. It indicates a typical evaporation time many orders of magnitude larger than our simulation time. That explains why in practice we never even observed in simulation a spontaneous evaporation event off the solid surface. This however does not invalidate the significance of simulation results. At any given instant of a realistically long time evolution of NaCl(100), there will be of course molecular evaporation and step flow, but that will still leave defect free terraces much larger on average than those we simulated.

	Simulation	Experiment
T_{M}(K)	1066±20	1074
ΔV	27%	26%
L (eV/molecule)	0.29	0.29
ΔS_m (k_B)	6.32	6.38
dP/dT (kbar/K)	0.0311	0.0357 [110]
α (10^{-6} K^{-1})	40.5	38.3
RMSD (Å)	0.60	0.49
δ	20–22%	17–20% [98]

Table 3.1: High temperature properties of NaCl. T_{M} is the melting temperature; ΔV is the volume jump at the melting point; L is the latent heat of melting; ΔS_m is the entropy variation at the melting point; dP/dT is the resulting Clausius-Clapeyron ratio at the melting point. α is the linear thermal expansion coefficient; RMSD is the root mean square displacement of atoms in the bulk solid at the melting point; δ is the RMSD over the Na–Cl distance, for the Lindemann melting criterion.

3.5 Summary

In this Chapter we carefully studied by MD simulations the main bulk properties of NaCl in wide temperature range. We found a very good correspondence between simulation results and experimental bulk melting (see Table 3.1), while the vibrational properties showed poorer agreement due to the rigid ion potential (see also Section 2.1.3)

Most of these results are well known and have been already discussed in earlier fundamental studies[64, 24, 101, 102]. Nevertheless we have obtained a very accomplished catalogue for the most properties, that will be directly needed in the surface studies in next Chapters.

Chapter 4

Alkali halide surfaces

4.1 Crystalline NaCl(100): a nonmelting anharmonic surface

Satisfied with the above description obtained for bulk NaCl, we moved on to study the NaCl surfaces, by simulating slabs as described earlier (see Chapter2). Surfaces were studied with periodically repeated slabs – consisting of $12 \div 24$ planes – separated by about 80 Å of vacuum. In slab simulations, we found the defect free NaCl(100) to warm up uneventfully, and to remain solid and totally dry up to $T_{\rm M}$. The root mean square displacements (RMSD) of the first layer Na^+ and Cl^- ions at $T_{\rm M}$ were extracted and are shown in Fig. 4.1 and Fig. 4.2.

Unsurprisingly, the surface ions vibrate more than bulk ions. The ratio of surface/bulk RMSD at $T_{\rm M}$ is here 1.5. For comparison, in the Pietronero-Tosatti model [20] the critical surface melting value of this ratio is ~ 1.6. Moreover, vibrations are somewhat more extended in direction perpendicular to the surface than in the in-plane direction.

We subsequently verified that even *above* $T_{\rm M}$ the NaCl(100) surface remained crystalline in a metastable state for at least 200 ps. In this overheated surface regime, solid NaCl(100) was found to possess a thick nucleation barrier against melting up to about T^* = 1115 K $\sim T_{\rm M}$ + 50 K, in the following sense. When a thin surface film consisting of ℓ atomic layers was artificially melted, and then let evolve to equilibrium at a grid of temperatures $T \geq T_{\rm M}$, the melted film was seen to spontaneously recrystallize for $\ell \leq \ell_{crit}(T)$, with $\ell_{crit}(T) \geq 1$ for $T \leq T^*$. That

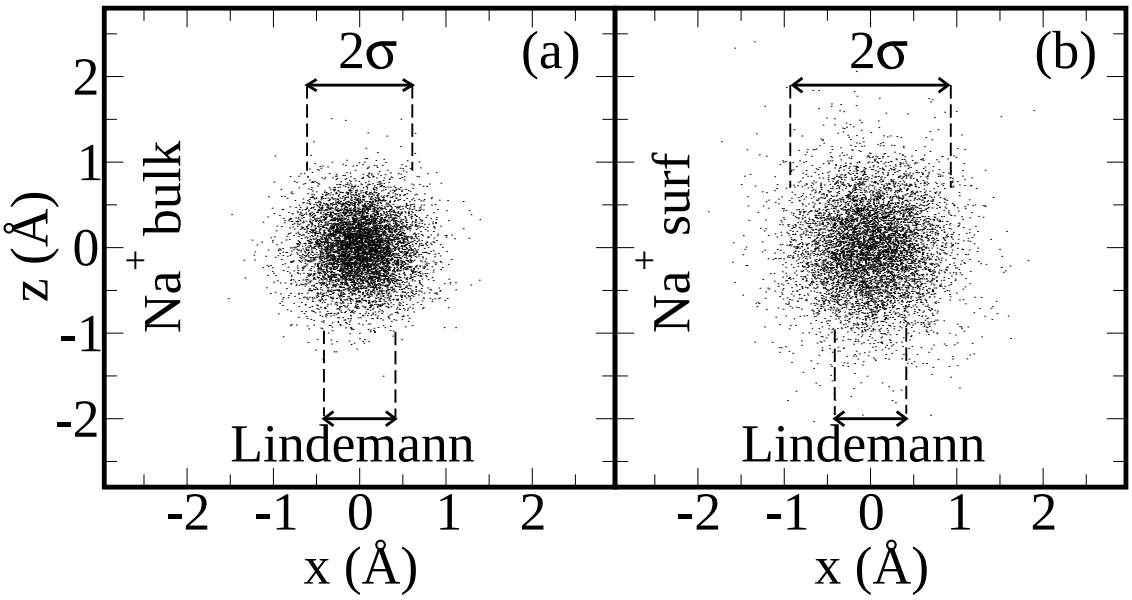

Figure 4.1: Solid NaCl instantaneous displacements of Na^+ ions in (a) bulk and (b) first surface layer at $T_{\rm M}$. Abscissa: (100) direction (in plane). Ordinata: (001) direction (out of the surface plane). The displacement distributions are well fit by gaussian distributions whose widths are $0.22 \times a$(a) and $0.33 \times a$(b) where a is the interatomic distance. The much smaller widths predicted by the Lindemann melting criterion $(\overline{\Delta r^2})^{1/2} \sim 0.15 \times a$.

indicates that in this temperature range the overheated solid slab is locally stable, with a free energy barrier against overall melting [5].

Above T^*, overheating of crystalline NaCl(100) persisted until a higher "surface spinodal temperature" $T_{\rm SS} \simeq$ 1215 K $\simeq T_{\rm M}$+ 150 K, now however with only a thin nucleation barrier $l_{crit}(T)$ of a monolayer. Only at $T_{\rm SS}$, as high as 150 K above $T_{\rm M}$, does solid NaCl(100) become locally unstable and melt spontaneously. We find the pronounced metastability of this solid surface to persist at least up to T^*, or $\sim$ 50 K above $T_{\rm M}$ even in presence of common surface defects, such as molecular vacancies or steps. We have thus characterized NaCl(100) as a clear case of surface non-melting. This is a prediction that deserves to be tested in experiment. For a short enough time, it should be possible to raise the temperature of NaCl(100) by at least 50 K above $T_{\rm M}$, without any liquid spontaneously nucleating at the surface. Of course, the solid surface will sublime very strongly at these temperatures (see Section 3.4).

The above considerations suggest that surface non-melting in alkali halides

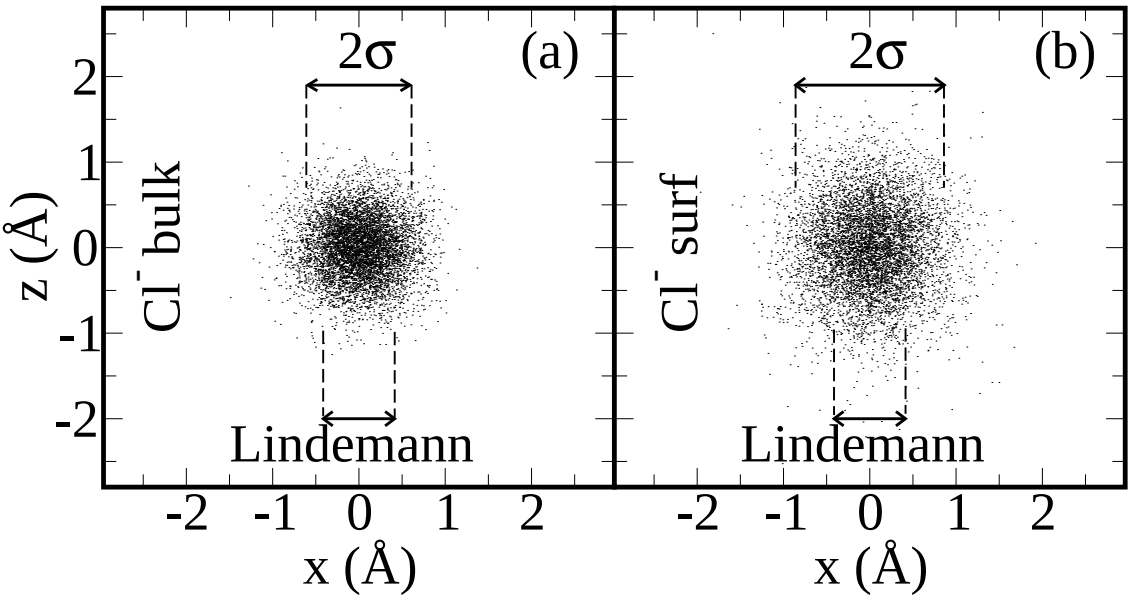

Figure 4.2: Solid NaCl instantaneous displacements of Cl^- ions in (a) bulk and (b) first surface layer at T_M. Abscissa: (100) direction (in plane). Ordinata: (001) direction (out of the surface plane). The displacement distributions are well fit by gaussian distributions whose widths are $0.2 \times a$(a) and $0.3 \times a$(b) where a is the interatomic distance. The much smaller widths predicted by the Lindemann melting criterion $(\overline{\Delta r^2})^{1/2} \sim 0.15 \times a$.

could not easily be pursued with static or nearly static experimental probes, because sublimation and condensation will influence and possibly spoil the outcome. Perhaps the fast laser tools already employed for metals [31] could be brought to bear on this case too. The vapor pressure also suggests techniques that do not rely on ultra-high vacuum [32].

4.2 Solid surface free energy

4.2.1 Thermodynamic integration

In order to prepare for our thermodynamical assessment of the wetting of NaCl(100) by liquid NaCl, we eventually need to know according to Young's equation the solid-vapor interface free energy γ_{SV} at the melting point. We do that by thermodynamic integration.

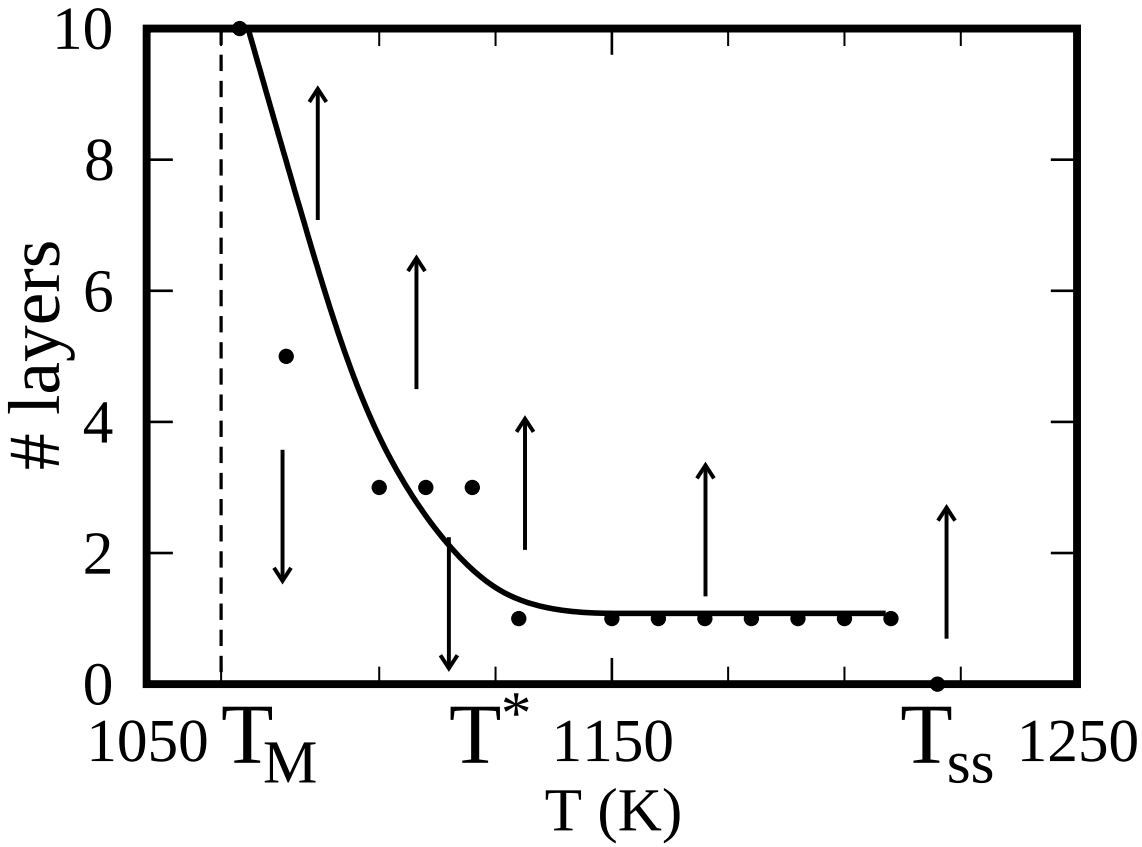

Figure 4.3: Critical liquid film thickness vs temperature for metastable solid NaCl(100) above $T_{\rm M}$. This corresponds to the effective thickness of the free energy barrier for the nucleation of the NaCl melt at the solid surface.

For this purpose, we simulated a 2880 molecule bulk system and independently a slab comprising 1440 molecules and an equivalent volume of vacuum. We kept in this manner the all-important Ewald sum convergence unchanged, (we judge the implied extra error due to size effects to be negligible by comparison). By integrating the internal energy over $(1/T)$ up to temperature T we separately obtained the bulk and the slab free energies per molecule up to $T_{\rm S}$ and to $T_{\rm SS}$ respectively. We did not explicitly include quantum freezing effects at low temperatures, because they represent a small correction in comparison with large thermal effects at the melting point. Nevertheless since quantum freezing takes place at temperatures $T \lesssim (1/4)\theta_D$, (θ_D is the Debye temperature), we started integration at $T_i = (1/4)\theta_D$ which is $\simeq$ 50 K for NaCl, therefore using the T = 50 K state as a reference.

$$\frac{F(T)}{T} - \frac{F(T_i)}{T_i} = \int_{1/T_i}^{1/T} E(T')\, d\left(\frac{1}{T'}\right). \tag{4.1}$$

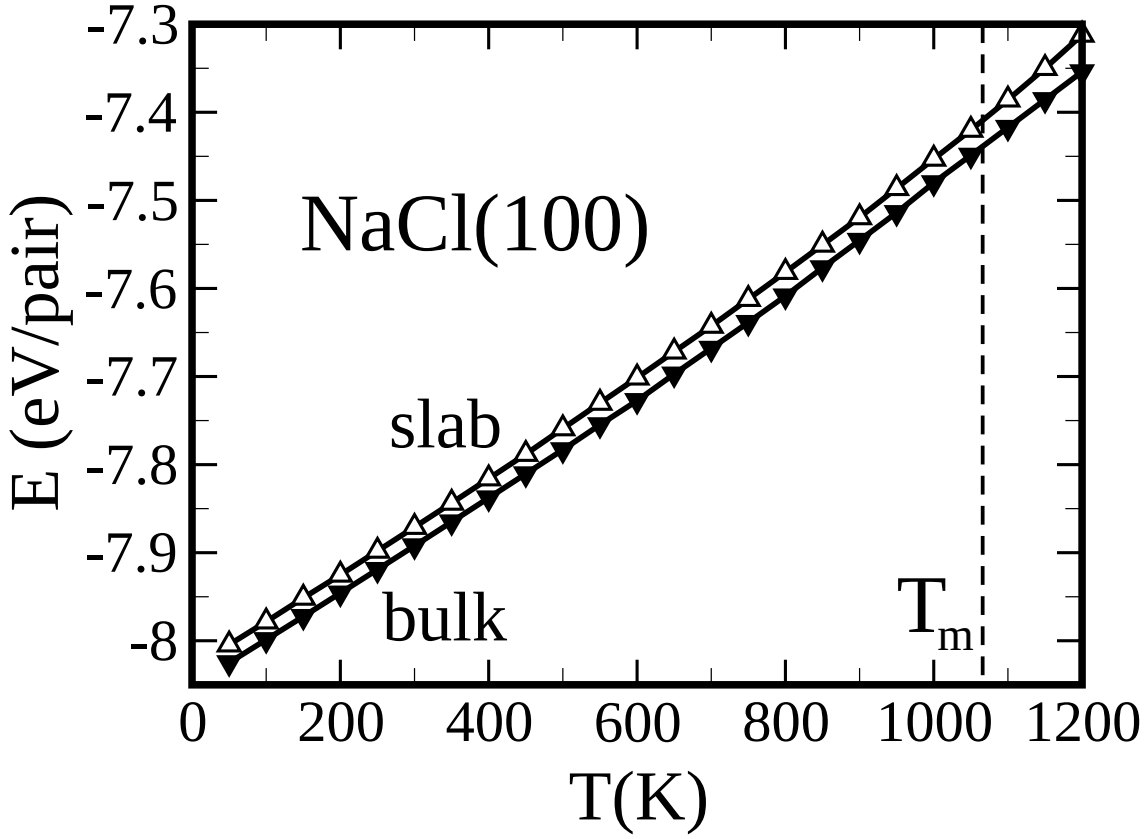

Figure 4.4: Bulk (filled triangles) and slab (empty triangles) internal energies as a function of temperature. The slab consisted of 1440 NaCl molecules.

The bulk and slab internal energies as a function of temperature, are shown in Fig. 4.4. After integration, the difference between slab and bulk free energies per unit surface area (accounting the presence of two surfaces) equals the surface excess free energy.

The NaCl(100) surface free energy calculated in this manner is displayed in Fig. 4.5. Starting at low temperature, we note from the start a low surface energy, reflecting the excellent charge order of this surface. Upon increasing temperature, there is an important thermal drop of the surface free energy, especially fast for $T \gtrsim 600$ K, indicating considerable additional anharmonicity of the solid surface relative to bulk solid NaCl. A good question is what part of that anharmonicity can be ascribed to temperature-dependent effectively harmonic vibrations, and what cannot.

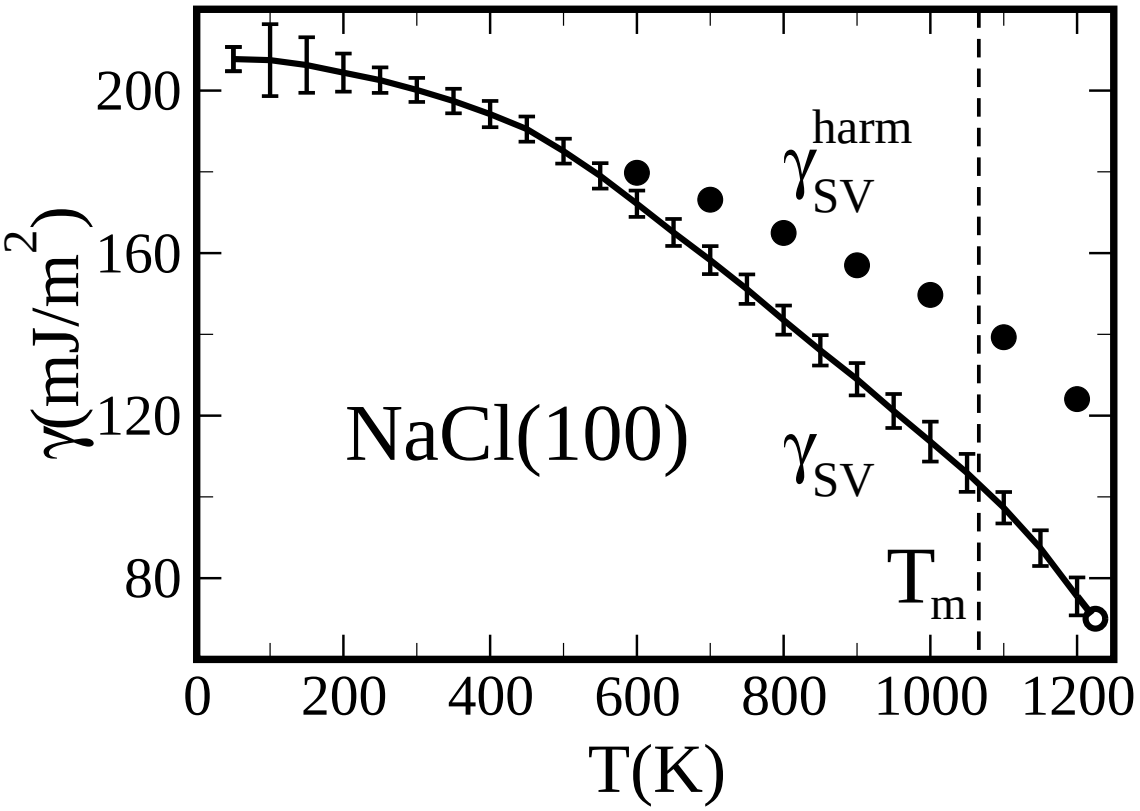

Figure 4.5: The solid surface free energy from thermodynamic integration (line) and from the effective harmonic approximation (dots).

4.2.2 Effective harmonic approximation

To judge on that, we computed separately the bulk and slab vibrational spectra as a function of temperature. Using simulation trajectories in a bulk and in a slab comprising exactly the same number of molecules, we extracted the Fourier transformed velocity autocorrelation functions of ions $V_{\mathrm{Na}}(\omega)$ and $V_{\mathrm{Cl}}(\omega)$. The vibrational spectra are obtained as:

$$A(\omega) = \frac{m_{\mathrm{Na}}}{k_B T} V_{\mathrm{Na}}(\omega) + \frac{m_{\mathrm{Cl}}}{k_B T} V_{\mathrm{Cl}}(\omega). \tag{4.2}$$

By treating both the bulk and the slab spectra as a collection of harmonic oscillators (Section 2.1.6), we obtained an effective surface vibrational free energy by subtracting their respective harmonic free energies off one another, and dividing the outcome by two, for two surfaces.

For increasing temperatures, the surface component of the slab spectra displays a stronger anharmonic softening than the bulk. This as anticipated gives rise to

an "effective harmonic" drop of surface free energy, as shown by dots in Fig. 4.5. We conclude that whereas about half the total anharmonic free energy decrease can be ascribed to the effective surface vibrational free energy and in particular to the surface frequency softening with temperature, the remaining half cannot be accounted for in this way, representing "hard" anharmonicity.

In conclusion the surface free energy of NaCl(100) approximately halves its value from $\sim$ 206 mJ/m^2 at 50 K to $\sim$ 100 mJ/m^2 at $T_{\rm M}$. Such a large decrease of the already unusually small low-T surface energy results in an exceptionally stable solid surface. While the physical reason for a low surface energy at low-T is clearly the perfect charge ordering, that for its large thermal decrease is the ability of rocksalt and of its surface to sustain exceptionally large anharmonic vibrations without loss of mechanical stability.

4.3 The liquid NaCl surface

The the liquid-vapor interface were previously studied in RPM [111, 68] and BMHFT [40] models. The more sophisticated recent studies of Aguado et al. [71] of the liquid KI surface emphasize the role of polarization forces, and also summarize earlier work.

Notwithstanding that, our scope here is to pursue a homogeneous comprehensive study of all surface properties in a single simple model, and we therefore carried out a fresh study of NaCl in the BMHFT model, now with a larger size scale and better statistics than that of Heyes [40].

Starting with the same 6×6×12 solid slab used in the previous section for the study of NaCl(100), temperature was raised above the surface spinodal temperature causing the slab to melt. Subsequently, the liquid slab was gradually cooled down to $T_{\rm M}$, and equilibrated for about 50 ps, after which correlations were examined.

Because of the strong charge correlations in the bulk liquid, one might naively but not unreasonably have expected this liquid surface to be structured, maybe layered as in the metals [112], perhaps displaying a surface dipole [113]. The actual liquid local surface density profile $\rho_{+-}(z)$ obtained for both ionic species is shown in Fig. 4.6. All profiles are remarkably coincident and smooth, thus – as one could also see from earlier MD studies [40, 71]– totally devoid of structural

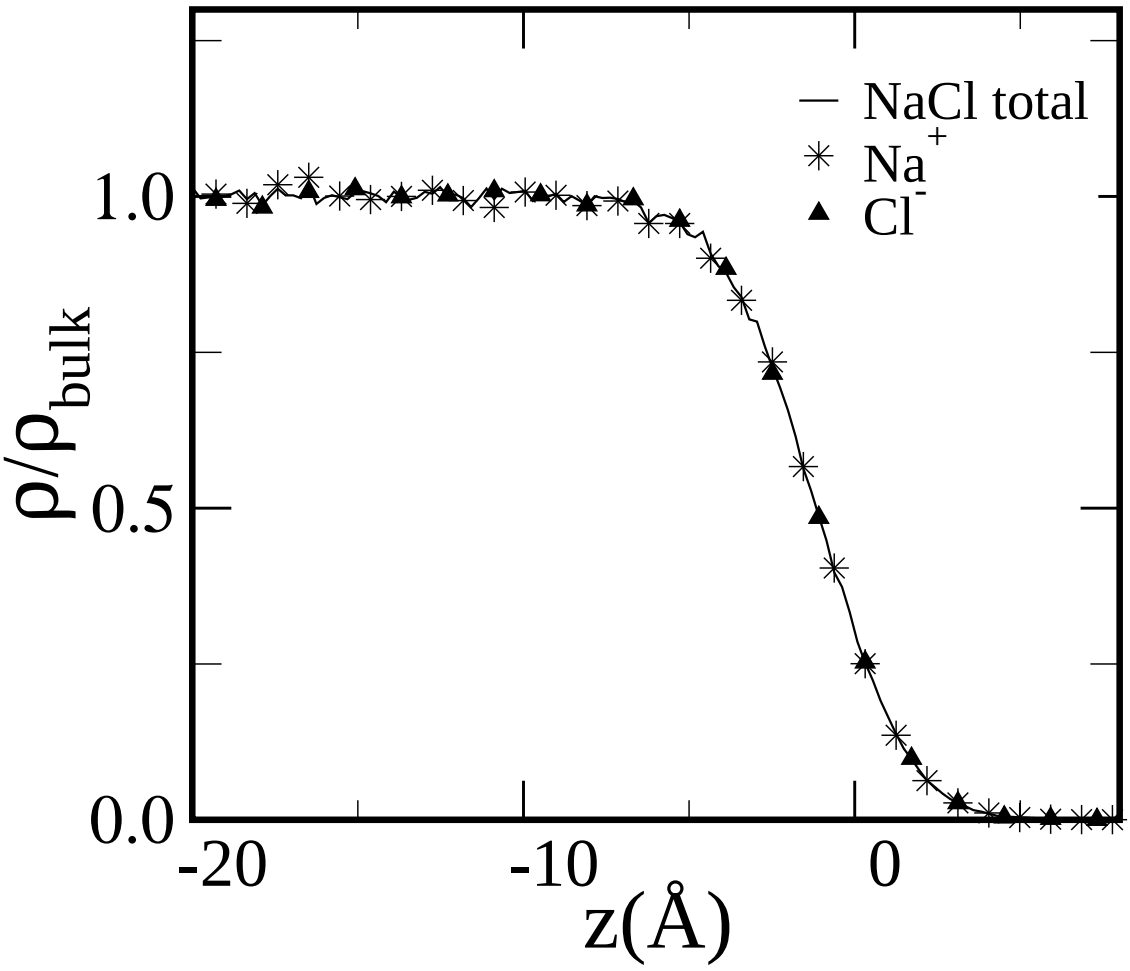

Figure 4.6: Na, Cl and total density profiles of the simulated liquid surface of NaCl at $T = T_{\mathrm{M}}$. Layering oscillations and surface dipoles are absent. Capillary fluctuations are very modest for our small cell size, and the large width of the liquid-vapor interface is a genuine local property of the surface.

layering. Moreover the Na and Cl profiles are superposable with very great accuracy, thus the liquid surface displays no static average dipole either, whereas the local time and space dependent dipole fluctuations are large.

We worried that the large apparent surface spatial width should really represent the local liquid surface structure, and not simply reflect long wavelength capillary fluctuations. For that purpose we carried out additional liquid slab simulations with alternatively a much smaller cell of size $4\times4\times4$, or a much larger one of size $10\times10\times15$. We found that the resulting surface density profiles remain essentially the same. We conclude that the additional capillary broadening of the

surface profile will only show up (logarithmically) for much larger sizes, and that the observed surface diffuseness is indeed intrinsic.

The nature of diffuseness of the NaCl liquid surface is clarified by the simulation snapshot of Fig. 4.7a, showing very pronounced local thermal fluctuations in the instantaneous surface profile. This picture, suggestive of a low surface tension, high entropy surface, is in apparent contradiction with the massive non-wetting of solid NaCl(100) by its own melt, the latter implying a relatively high liquid surface tension.

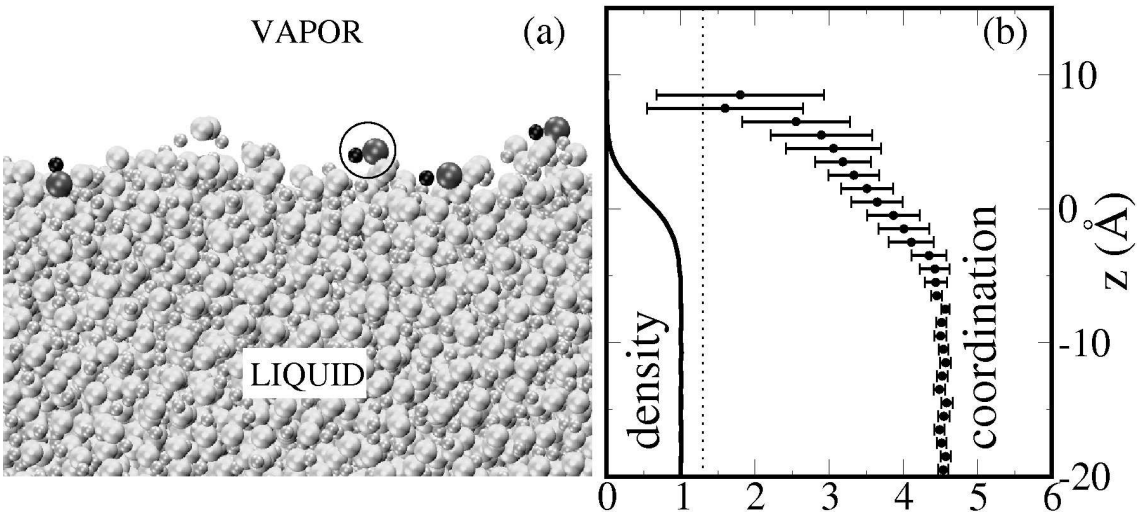

Figure 4.7: a) Simulation snapshot of the NaCl liquid surface at $T_{\rm M}$. Note the large thermal fluctuations, with some nearly molecular configurations highlighted in the outermost region; b) Coordination number $N(Z)$ and density profile, confirming a very smooth crossover from liquid (N=4.6) to molecular vapor (N=1.3 dotted line).

In order to clarify the situation, we undertook a direct calculation of the surface free energy $\gamma_{\rm LV}$, equal to the surface tension, of liquid NaCl. The calculation was done by evaluating the surface stress of the slab (which has two equivalent surfaces) via the Kirkwood-Buff formula:

$$\begin{aligned}\gamma_{\rm LV} &= -\frac{1}{8}\int_{-\infty}^{\infty} dZ \int d^3\mathbf{r} \sum_{\alpha,\beta} \frac{x^2+y^2-2z^2}{r}\big[\delta_{\alpha\beta} + \\ &+ \lambda(1-\delta_{\alpha\beta})\big] f_{\alpha\beta}(r) g^{(2)}_{\alpha\beta}(\mathbf{r};Z)\rho_\alpha(Z)\rho_\beta(Z) \qquad (4.3)\end{aligned}$$

where: $(\alpha,\beta) = (+,-)$, Z is the distance normal to the interface and $\langle\ \rangle$ denotes a canonical average and $\sum_{\alpha\beta}$ is over all species. Moreover **r**= (x,y,z) is the in-

teratomic distance, $f_{\alpha\beta}(r)$ is the force between atoms of species α and β, $g^{(2)}_{\alpha\beta}(\mathbf{r}; Z)$ are the Na-Cl, Na-Na, Cl-Cl pair correlation function measured in a slice centered at Z, $\rho_\alpha(Z)$ the average density of ion α near Z and finally λ is a parameter here equal to one, but inserted for later use.

The calculated liquid surface tension $\gamma_{\rm LV}$ is shown as a function of temperature in Fig. 4.13. The value at $T_{\rm M}$ is 104 ± 8 mJ/m^2, in fairly good agreement with the experimental surface tension of 116 mJ/m^2—and by chance essentially identical to that of the solid. A very large anharmonicity was shown earlier to explain the relatively low surface free energy of solid NaCl(100). The physical reasons that make the liquid surface tension so relatively high is less clear, and will be addressed below.

4.4 Liquid Surface Entropy Deficit: incipient molecular order in the liquid surface

Here we wish to understand the reasons for the relatively high surface free energy of liquid NaCl. A clue is provided by a comparison of solid and liquid surface excess *entropies*:

$$S_{\rm surf} = -d\gamma/dT. \tag{4.4}$$

Generally, one would expect that the much looser structure and greater freedom of ionic motion at a liquid surface should yield a larger liquid surface entropy than that of the solid surface. Strikingly, in NaCl the smaller calculated temperature dependence of surface free energies shows just the reverse. We find a factor 2.6 lower surface entropy $S_{\rm LV}$ compared with $S_{\rm SV}$ of the solid surface. It should be stressed that the value of $d\gamma_{\rm LV}/dT$ was known experimentally (and is close agreement with our calculated value) but that of $d\gamma_{\rm SV}/dT$ was not. Hence this comparison had not been possible so far. Let us focus on this inverted result, which indicates qualitatively speaking a liquid surface entropy deficit (SED). An entropy deficit is suggestive of some form of underlying surface short range order. The order is clearly not layering: so what is it instead?

The answer we found is that charge order, already very important in bulk, plays a newer and enhanced role at the molecular liquid surface. If surface thermal fluctuations are indeed very large, they are also revealingly *correlated*. For a Na^+ ion that instantaneously moves e.g., out of the surface, there is at least one accom-

panying Cl^-, also moving out; and vice versa. So while the large surface fluctuations smear the average liquid vapor density profile, bridging gently between the liquid and essentially zero in the vapor, (Fig. 4.6) the two-body correlations, described e.g. by the Na-Cl pair correlation function $g_{+-}(\mathbf{r})$, and by its integral, the ion coordination number N, drop from values typical of the bulk liquid at $T_{\rm M}$ to the *nonzero* value of the molecular vapor. For a quantitative characterization, we calculated a locally defined charge coordination number:

$$N_{\pm}(Z) = \frac{1}{2\delta z}\int_{Z-\delta z}^{Z+\delta z}\left\{dZ'\rho(Z')\int_{r<r_m} d^3\mathbf{r}\; g_{+-}(\mathbf{r};Z')\right\} \tag{4.5}$$

where $r_m = 4.0$Å corresponds to the first local minimum of $g_{+-}(\mathbf{r})$, and δz is a small interval. Starting with Z inside the liquid slab, where the environment is bulk-like, we recovered $N_{\pm_L} = 4.6$ Å at $T_{\rm M}$, as in the bulk liquid. Moving Z across the liquid-vapor interface we found $N_{\pm}(Z)$ to drop continuously from 4.6 downward (Fig. 4.7b).

In NaCl we know (even if simulation statistics is non-existing in the vapor) that $N_{\pm}(Z)$ for large Z is bounded below not by zero but by $N_{\pm_V} = 1.3$, the average value for the NaCl vapor at $T_{\rm M}$ (see Section 3.4). Here emerges the crucial difference between the molecular NaCl vapor and *e.g.*, the atomic LJ vapor, where $N_{\pm_V} \simeq 0$. The larger the coordination number of ions in the surface region, the less their configurational entropy, the higher the liquid surface tension. Hence incipient molecular order could provide the reason for the SED found for liquid NaCl.

In the bulk liquid an ion of a given sign does not have a well defined partner of the opposite sign, being surrounded by many more than one (in fact ~ 4.6 at $T_{\rm M}$). In the isolated molecule (Fig. 4.9) the same ion has one fixed partner instead. The surfaces lie halfway between these two extremes. So maybe partners have a longer life at surfaces. The bulk liquid it is similar to the group dancing where the partner's exchange does not ruin the general neutrality of the dance (see Fig. 4.8), whereas in couple dancing the presence of a fixed partner is crucial.

Figure 4.9: An old dancing couple.

To test this idea for SED, we repeated the same Kirkwood-Buff calculation of the surface tension done previously, now however by slightly and artificially altering in Eq. (4.3) the value of correlations g_{+-} at the surface. Specifically, we ar-

Figure 4.8: The ions in bulk liquid resemble the free African group dancing: no fixed partners, no strict order among dancers.

tificially reduced to zero the weight λ attributed to forces acting among Na^+ and Cl^- ions for that (extremely small) fraction of outermost surface atoms whose coordination number $N_{\pm} \lesssim N_{\pm_V} \simeq 1.3$, the mean vapor value. The contribution of these configurations to the pressure should provide a good measure of the influence of incipient molecular charge ordering to the surface free energy, in particular to the surface entropy. Through this highly artificial but in our view illuminating procedure, the surface internal energy (a mechanical variable) remains unchanged, and thus only surface entropy is affected.

We first identified the *surface* Na and Cl atoms in the simulation by means of

a simple algorithm. All ions are binned according to increasing Z and are represented by a sphere of finite radius (1.1 Å in our case). An ion is considered a surface ion when the projection on the (x, y) plane of its representative sphere is non overlapping with that of any other ion at larger z. For each so identified surface ion i, we extracted from the simulation the instantaneous electrostatic potential value V_i, a quantity related to the coordination number, but more convenient to calculate and to handle. As shown in Fig. 4.10 the overall electrostatic potential distribution of Na ions in the liquid slab is shifted toward the electrostatic potential value typical of the NaCl molecule, and away from that of the bulk liquid. This shift is evidently caused by the lower coordination of ions on the two surfaces of the slab, for the slab interior is bulk-like. The surface Na^+ ion potentials for example are shifted by ~ 0.1 eV on average relative to their bulk counterpart. The electrostatic potentials of Cl^- ions behave specularly, and are thus shifted by ~ -0.1 eV relative to their bulk counterparts.

As the next step we established the necessary connection between average electrostatic potentials (easily extracted from simulations, and at least in principle easily measurable) and coordination numbers (hard to extract from simulations,and probably harder to measure). The potential should vary monotonically with coordination, e.g., linearly for a fixed interatomic distance. Since in reality the Na-Cl distance increases with coordination, the overall dependence is somewhat less than linear as shown in Fig. 4.10. A raw histogram of electrostatic potentials against coordination numbers for the surface ions in the simulated liquid slab at T_{M} is shown in Fig. 4.11.

Finally, we computed a modified liquid surface tension by cutting off in the Kirkwood-Buff average in Eq. (4.3) the Coulomb part of the Na-Cl force contribution of surface Na ions, through a parameter λ of the form $\lambda = \theta(V_0 - V_i)$ where θ is the step function and V_0 is a cutoff potential value, selecting the type of correlations to be removed. For example, $V_0 = -6.8$ eV cuts off up to monomer correlations, $V_0 = -7.485$ eV cuts off up to dimer correlations, etc. In particular we choose $V_0 = -6.99$ eV, the value that cancels correlations for Na ions with $N \leq 1.3$, the vapor average.

With this tool, we are now able to examine more quantitatively the surface tension contribution due to the incipient surface molecular correlations causing $N_{\pm}(Z) \rightarrow N_{\pm_V} \simeq 1.3$, by correspondingly choosing the cutoff potential $V_0 = -6.99$ eV. This modification generally affects an exceedingly small fraction of surface ions. In particular, the Na^- ions affected are quite few, as highlighted

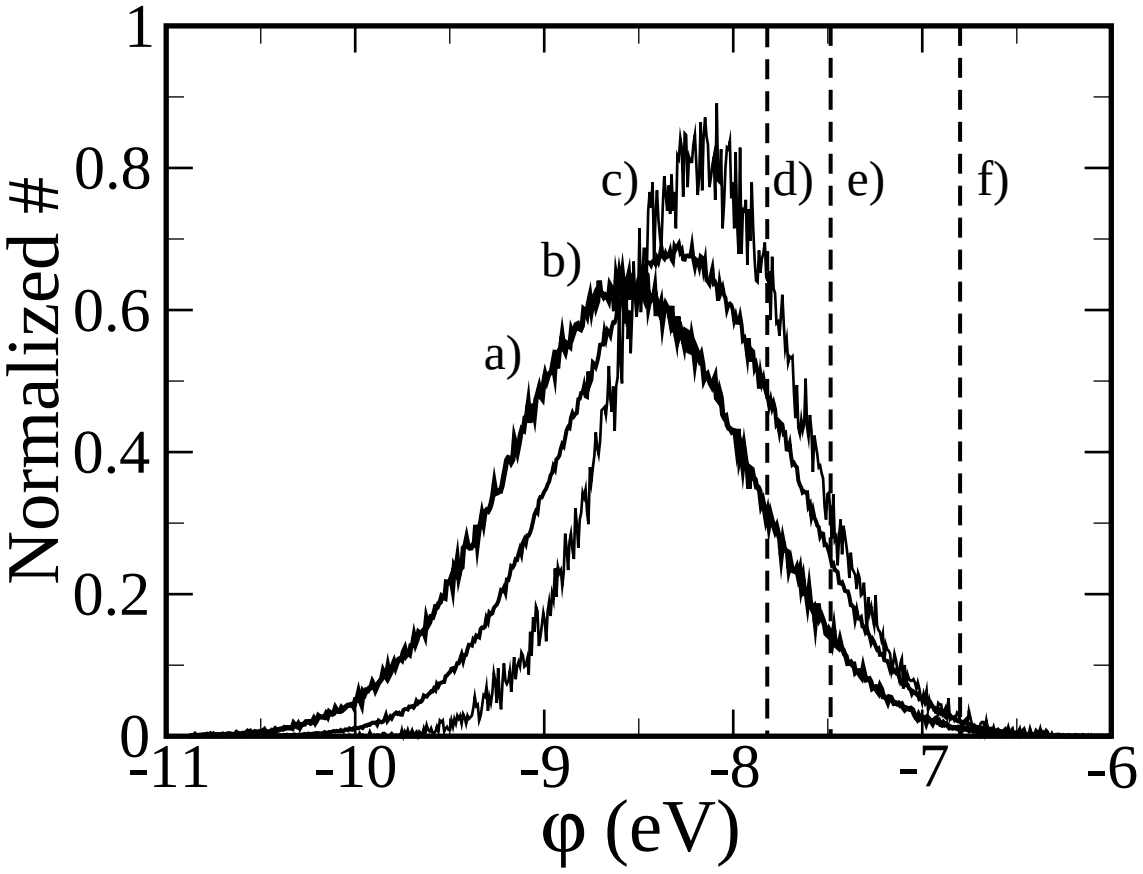

Figure 4.10: The electrostatic potential distribution at Na^+ ions in (a) bulk liquid NaCl; (b) solid bulk, and (c) slab liquid of thickness 70 Å, at $T_{\rm M}$. Comparison the potential at with BHMFT (d) trimers (e) dimers and (f) monomers is also provided. Precise values of the average ϕ are (a) -8.57 eV, (b) -8.32 eV, (c) -8.21 (d) -7.82 eV, (e) -7.485 eV, (f) -6.8 eV. The electrostatic distributions of Cl^- ions are just specular, that is identical to those of Na^+, with a plus sign.

in Fig. 4.7a. Nevertheless the partial removal operated of the surface tension contribution due to this molecular part of surface Coulomb correlations yields a very considerable overall surface tension decrease, with a large drop from $\gamma_{\rm LV} = 104$ mJ/m^2 to $\gamma^*_{\rm LV}$ to 53 mJ/m^2, as shown in Fig. 4.12, and Fig. 4.13.

This we interpret as a direct confirmation that incipient molecular surface correlations are indeed responsible for the liquid SED and for the resulting high surface tension. Remarkably, since now $\gamma^*_{\rm LV} + \gamma_{\rm SL} < \gamma_{\rm SV}$, the surface tension drop following the hypothetical removal of short range surface molecular correlations would actually suffice to drive a *complete* instead of partial, wetting of NaCl(100) at the melting point.

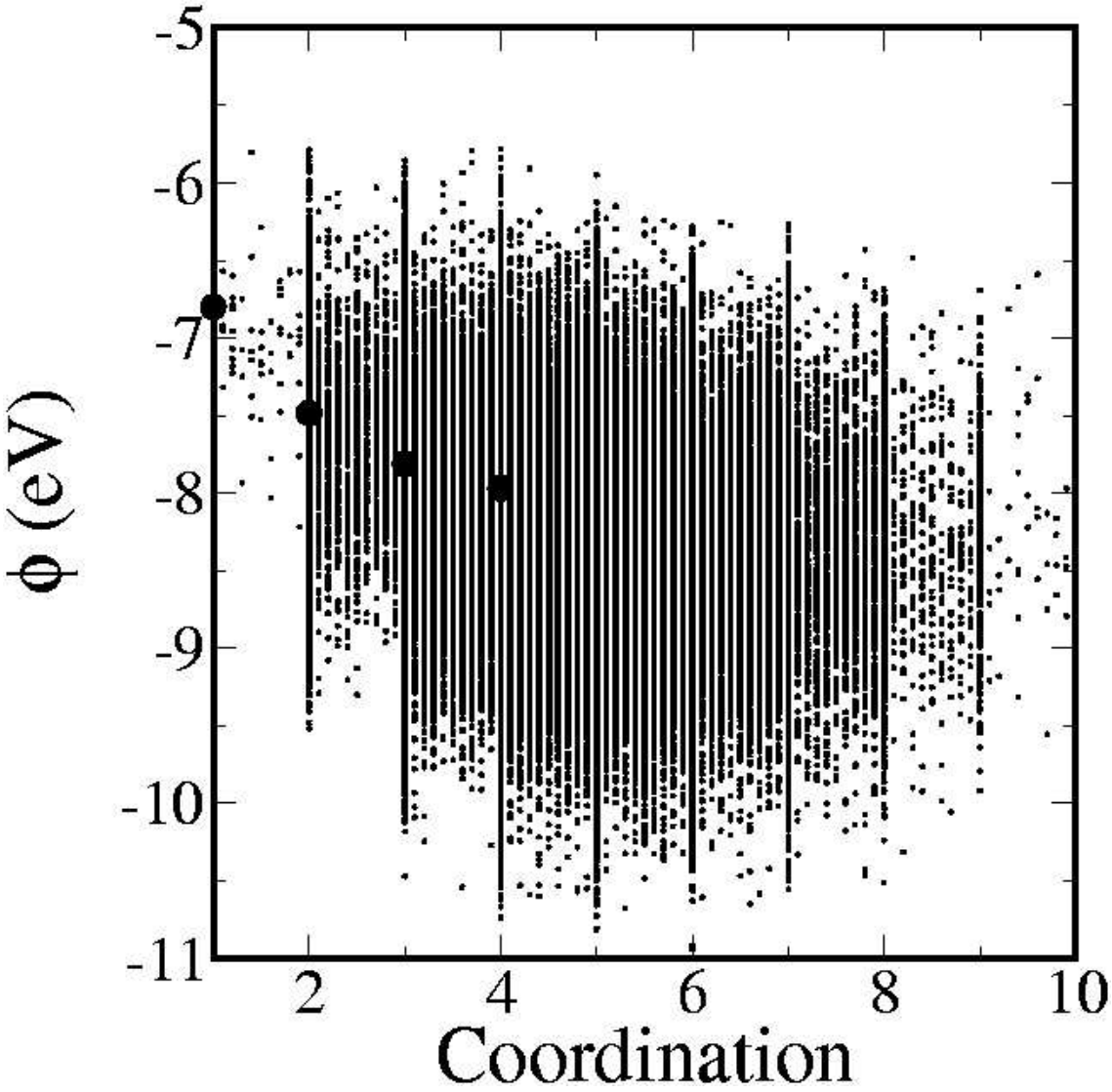

Figure 4.11: Electrostatic potential distribution of surface Na^+ ions, plotted versus their own instantaneous coordination number. Superposed is the molecular correlation between potential and coordination.

The increased temperature slope $|d\gamma^*_{\rm LV}/dT|$ confirms that the calculated surface tension drop is directly related to the restoring of a larger surface entropy, with removal of some of the SED through cancellation of molecular surface correlations. We found in fact that the drop from $\gamma_{\rm LV}$ to $\gamma^*_{\rm LV}$ at $T_{\rm M}$ corresponds exactly to the increased temperature slope $-d\gamma^*_{\rm LV}/dT$, that is to the surface entropy increase, therefore with no change of surface internal energy as expected.

Indirect confirmation of the surface molecular ordering can be found in the

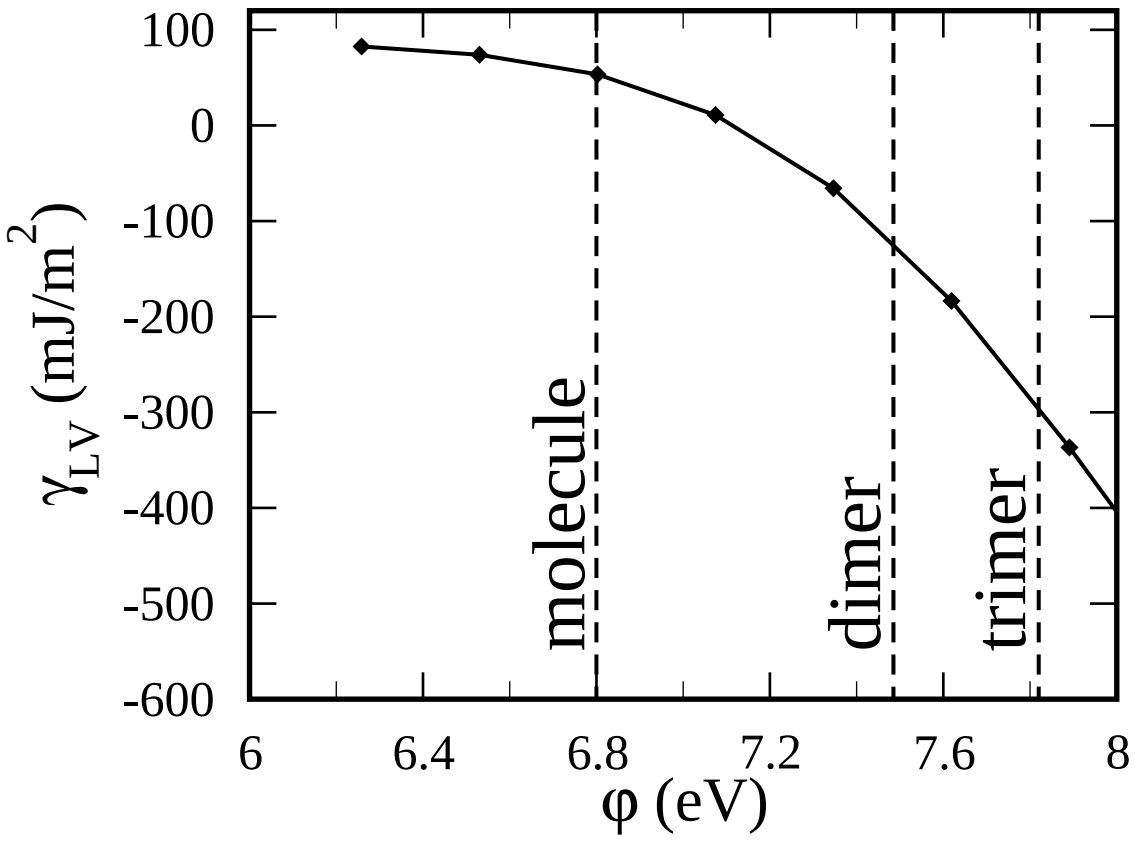

Figure 4.12: The decrease of fictitious liquid surface tension γ^*_{LV} at T_{M} with increasing surface correlation coordination cutoff.

Heyes's earlier simulations[40]. Applying a parallel to surface electric field of 0-1.44 V Å^{-1} he observed a higher ionic mobility in *bulk* than at the surface, this effect is highly unusual, but was left unexplained. However a diminished ionic mobility clearly follows if there is local molecular order for the neutral NaCl molecule.

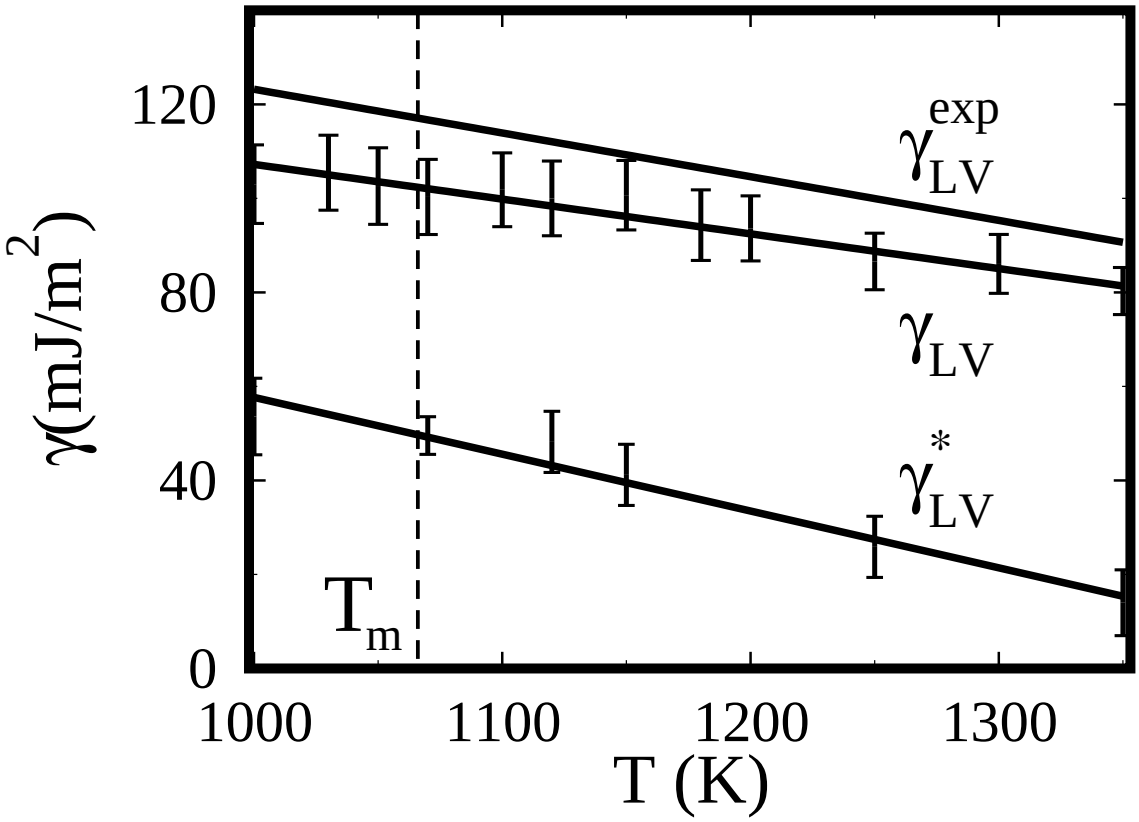

Figure 4.13: Liquid NaCl surface tension. Note the good agreement of the calculated $\gamma_{\rm LV}$ with experiment $\gamma_{\rm LV}^{exp}$. $\gamma_{\rm LV}^{*}$: artificial surface tension calculated by setting $\lambda = 0$ for outer surface atoms with coordination below 1.3 (highlighted in Fig. 4.7a). Once surface molecular order is removed in this way, surface entropy rises, surface tension drops, as shown. Solid NaCl(100) would be completely wet by this artificial liquid. The experimental data are from Ref. [39]

Chapter 5

Simulation of nanodroplet deposition on NaCl(100)

Up to this point of the three interface free energies γ_{SV}, γ_{LV} and γ_{SL}, we have calculated the first two. Although it is in principle possible to devise thermodynamics integration schemes to estimate the third one, γ_{SL} [114], we chose to follow a different route. If we could simulate the contact of a NaCl nanodroplet on NaCl(100), we can at the same time obtain a direct verification of Mutaftschiev's partial wetting, and also obtain γ_{SL} from Young's equation. Technically the droplet approach to the surface is still time consuming and delicate simulation whose final outcome is not guaranteed. Here we present a detail description of the numerical experiment which we actually performed on NaCl(100).

5.1 Preparing initial configuration

First we prepared a large 7200 atom crystalline slab, 8 atomic planes thick ($15 \times 15 \times 4(\mathrm{NaCl})_4$ conventional cubic cells). The slab was gradually heated up to the bulk melting point, keeping two atomic layers rigidly fixed at the bottom of the slab, however with a lattice spacing growing as usual with T, in order to simulate a thermally expanding semi-infinite solid. The slab did not melt due to nonmelting behavior of NaCl(100).

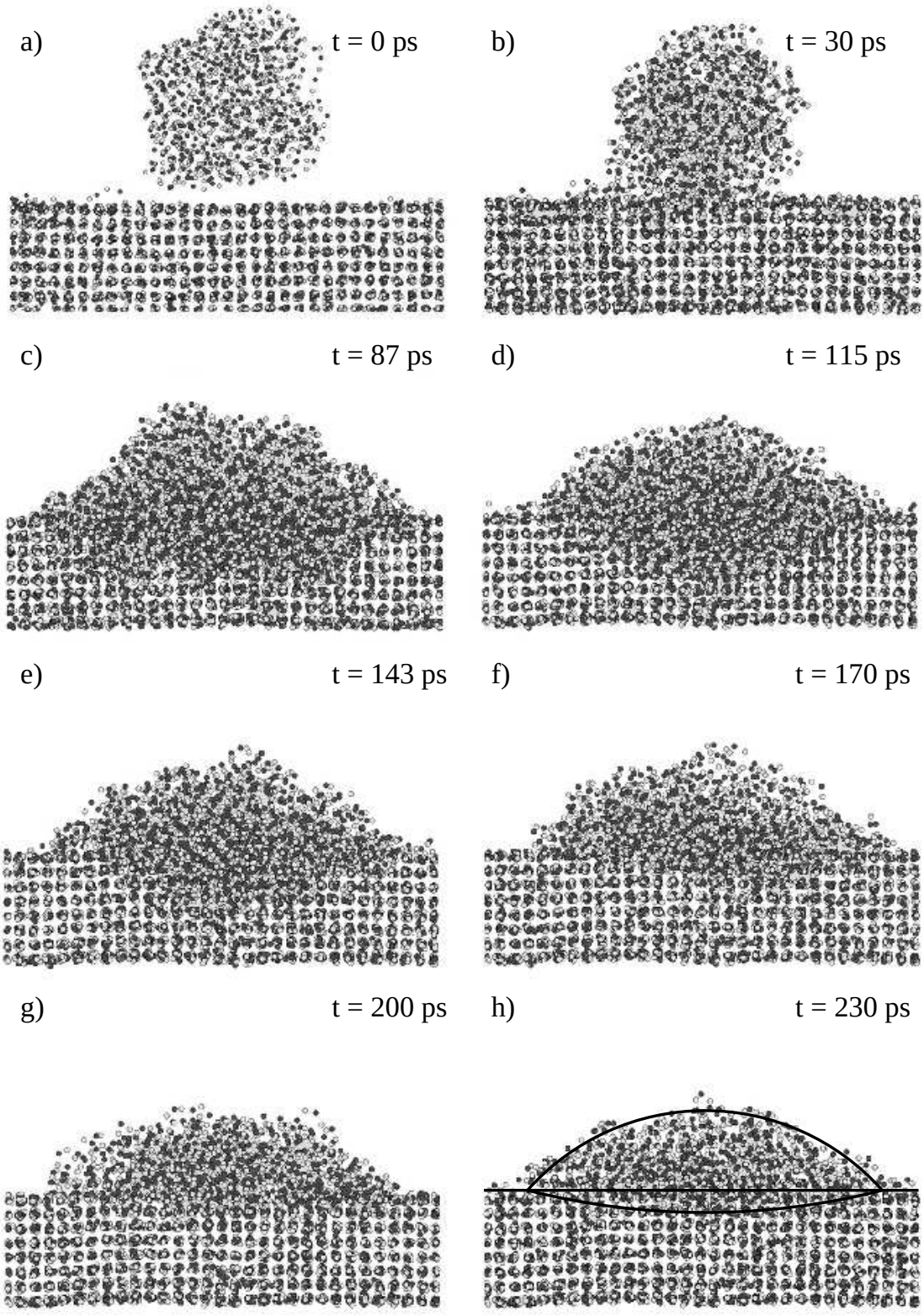

Figure 5.1: Time evolution of the liquid NaCl drop on NaCl(100). Dark and light circles stand for the Na^+ and Cl^- ions respectively.

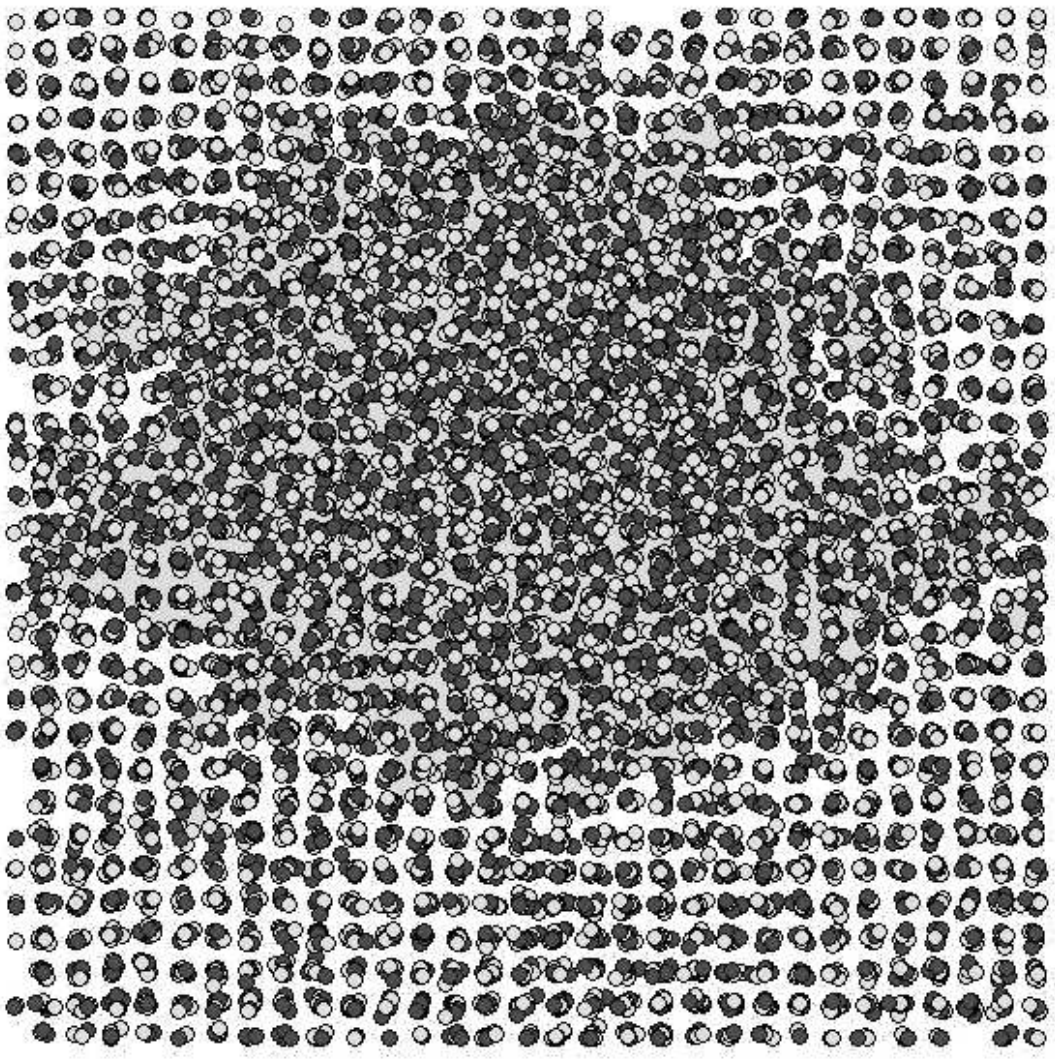

Figure 5.2: Top view of the liquid droplet on the NaCl(100) after 230 ps. Dark and light circles stand for the Na^+ and Cl^- ions respectively. The shape of the drop does not shows only temporary asymmetries or anisotropies.

Separately we prepared a small NaCl cluster consisting of 500 NaCl molecular units. The size of this cluster was large enough to yield after melting a near-spherical drop, and also a well-defined shape when the drop is deposited on the surface. The cluster was melted by heating above the bulk melting temperature and then it was equilibrated at T=T_{M} for 100 ps, yielding a well-defined spherical liquid droplet of radius 18 Å. Finally, we placed the drop near the solid NaCl(100) slab surface, the lowermost atoms of the drop a distance 4 Å from the surface (fig. 5.1a). Zero vertical velocity was assigned to the drop center of mass but the drop expanded anyway to touch the surface. As soon as the drop contacted the surface, attempts at equilibrating the system at the theoretical melting temperature (T_{M}) failed, and the whole solid NaCl slab melted very quickly. We succeeded finally in equilibrating the liquid nanodroplet on the solid surface at the intermediate temperature of 1050 K, which is only slightly below T_{M} of our model. This is described in the following section.

5.2 Droplet evolution

The nanodroplet and the solid slab were separately equilibrated at 1050 K. During the first 100 ps after contact, the droplet settled down on the substrate, gradually approaching the final shape (fig. 5.1b-d). In the next 130 ps, the droplet survived in a (not clear if metastable or unstable, but long lived) state without spreading appreciably (fig. 5.1e-f). At the end of our simulation, the droplet – substrate system looked like fig. 5.1h. The top view of fig. 5.2 shows that the drop spread almost circularly.

Before proceeding with further descriptions, it is important to specify the thermodynamics of this situation. Because we are below T_{M} (even if slightly) the final equilibrium state should consist of a flat solid NaCl(100) surface, i.e. the nanodroplet should completely spread and recrystallize. That however will take a very long time. While the nanodroplet exists, it will form an external wetting angle θ_{LV} (fig. 5.1), as well as an internal angle θ_{SL}. The latter θ_{SL} is irrelevant here, because it depends critically on the temperature and on the time. In particular at short times and not too far from T_{M} we expect $\theta_{\mathrm{SL}} \approx 0$. The external angle θ_{LV} is instead significant, as it should equal the macroscopic wetting angle measured in the bubble experiment[1, 3], and is slowly varying function of the temperature.

At a much lower temperature than T_{M} (1000 K) on the contrary, the substrate

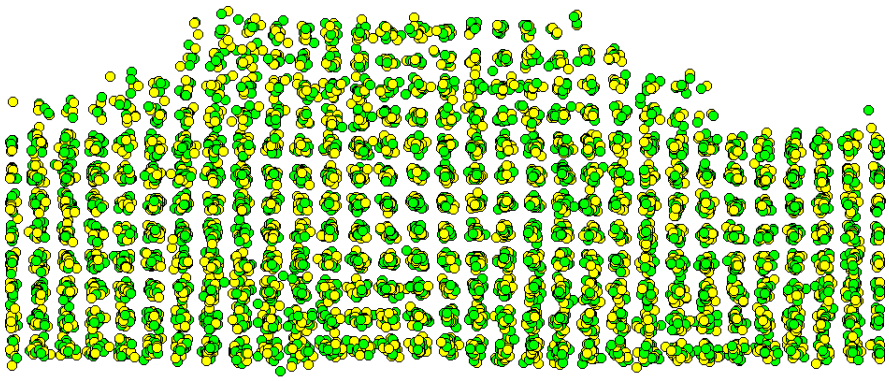

Figure 5.3: The crystallization of liquid drop on NaCl(100) to a "Maya pyramid" ∼150 K below T_{M}. Dark and light circles stand for the Na^+ and Cl^- ions respectively.

remained solid, while the drop spread slightly only at the beginning but then crystallized, giving rice to a truncated "stepped" pyramid (see Fig. 5.3), made up of (100) facets. These "Maya pyramids" are reminiscent of hillocks observed by Szymonski *et al* [115] and Gnecco *et al* [116] on ion bombarded NaCl(100).

Assuming quasi equilibrium for the liquid nanodroplet in the sense specified above, this angle will obey Young's equation (see Fig. 1.4) $\gamma_{\mathrm{SL}} + \gamma_{\mathrm{LV}} \cos\theta_{\mathrm{LV}} = \gamma_{\mathrm{SV}}$ where the γ's are the interface free energies. To determine the external wetting angle θ_{LV} of the nanodroplet we analyzed 100 configurations in last 100 ps. The instantaneous atomic positions were plotted in cylindrical coordinates (r and z, where r is parallel to the surface), and from the profile of the drop, we determined the best approximation to a portion of a sphere, by determining the center position and the radius. The contact angle follows immediately by simple geometry from these two quantities. Our best estimate slightly below T_{M} is $\theta_{\mathrm{LV}} = 50^\circ \pm 5^\circ$ which is in excellent agreement with the experiment value 48° at the melting point [1]. At the end of the simulation the internal solid-liquid interface was still relatively sharp and flat, consistent with our assumption $\theta_{\mathrm{SL}} \approx 0$.

5.3 Solid-liquid interface free energy

The knowledge of the detected contact angle and solid and liquid surface free energies allow us to calculate via Young's equation a solid-liquid interface free energy γ_{SL} = 36±6 mJ/m^2. A solid-liquid interface free energy of more than one third the surface tension γ_{LV}(= 104 mJ/m^2) is unusually large. Here, that is clearly attributable to an unusually large difference of density, as well as of correlations, between the solid and the liquid at the melting point. Corresponding to that, the solid-liquid interface is spatially rather abrupt, as seen by Fig. 5.1 and Fig. 3.7.

Further we can try to relate the wetting angle θ_{LV} to more microscopic quantities. The free energy gain upon crystallizing the surface at $T = T_{\mathrm{M}}$, $\Delta\gamma_\infty = (\gamma_{\mathrm{LV}} + \gamma_{\mathrm{SL}}) - \gamma_{\mathrm{SV}}$ is related to the partial contact angle through Young's equation that can be rewritten as

$$\cos\theta_{\mathrm{LV}} = 1 - \frac{\Delta\gamma_\infty}{\gamma_{\mathrm{LV}}} \tag{5.1}$$

When we plug in our calculated value of $\gamma_{\mathrm{LV}} \simeq 104$ mJ/m^2 and $\theta_{\mathrm{LV}} = 50^\circ \pm 5^\circ$, we obtain $\Delta\gamma_\infty = 37$ mJ/m^2.

A further connection between $\Delta\gamma_\infty$ and the surface spinodal temperature T_{SS} was made by assuming a phenomenological SL-LV interface interaction of the form [15]:

$$\Delta\gamma_\infty \simeq \rho L a \left(\frac{T_{\mathrm{SS}}}{T_{\mathrm{M}}} - 1\right). \tag{5.2}$$

With our value of $\Delta\gamma_\infty$, and L = 4.813 · 10^9 erg/g, a = 5.9 Å we predict T_{SS} = 1210 K, quite close to that seen in simulations.

5.4 Discussion

The formation of the partially wetting drop on a generic substrate is a common phenomenon. The drop's shape on a substrate is given by the total free energy minimum under the constraint of the constant volume of the drop. In our case when the drop and the surface are composed of the same material the drop volume is no more constant and only the chemical potential remains constant. Therefore the final form and fate of the drop are not easily predictable. If we neglect the anisotropy of solid-liquid interface we found that the lens like form (see Fig. 1.4) as indicated by Nozieres [117] reasonably well describes our results.

In conclusion, molecular dynamics simulations indicate that metastable liquid NaCl nanodroplets on solid NaCl(100) can exist for some time close to T_{M}. They are found to exhibit an unusually large partial wetting angle, whose value is in agreement with the large macroscopic wetting angle observed in the bubble experiment. Thermodynamically this appears to be caused by an unusual small value of the solid-vapor interface free energy, as well as by a large solid-liquid interface free energy. The free energy differences extracted via Young's equation can also be connected well with other properties, such as the solid surface spinodal temperature.

Conclusions of part I

We studied the physics of the solid NaCl(100) surface and its wetting relationship with liquid NaCl at and near the melting temperature of bulk NaCl. Molecular dynamics simulations performed with classical BMHFT potentials were first of all shown to yield quite an accurate description of high temperature solid and liquid bulk. The NaCl(100) surface was subsequently studied, and found to be a non-melting surface, one that should in principle be possible to overheat well above T_{M}. The solid surface free energy was calculated by thermodynamic integration and seen to drop very considerably at high temperature due to large anharmonicities. The liquid NaCl surface was also studied, and found to be very diffuse, strongly fluctuating, and devoid of static structure such as layering, or surface dipoles. However, calculation of the liquid surface tension still gave a relatively large value, similar to the solid surface free energy at the melting point. The high surface tension signifies an unusual liquid surface entropy deficit, here ascribed to short range molecular order. In addition, the solid-liquid interface free energy was also found to be relatively large, about one third the liquid surface tension, consistent with the large density difference between solid and liquid. Direct simulation of a NaCl droplet deposited onto NaCl(100) demonstrated very realistically the incomplete wetting, implied by the clear satisfaction of Young's equation. At T_{M}, we obtained the solid, liquid and solid-liquid surface free energies shown in Table 5.1 quantitatively explaining the surface nonmelting of NaCl(100).

The present work is meant as a prototype study, ideally repeatable for other elemental and molecular systems including perhaps water and the surface of hexagonal ice [118].

γ	$\mathrm{mJ/m^2}$
γ_{SV}	103±4
γ_{LV}	104±8
γ_{SL}	36±6

Table 5.1: Our results of NaCl interface free energies at T_{M}.

In alkali halides, the extraordinarily poor wetting of the solid (100) surface by the melt is traced to the conspiracy of three separate factors, all of which can be finally related to the long range Coulomb interaction between ions: (i) surface anharmonicity stabilizes the solid surface; (ii) molecular correlations destabilize the liquid surface; (iii) a large density jump makes the solid-liquid interface very costly.

Several aspects uncovered in, or implied by, this study should be amenable to direct experimental verification. X-ray studies should confirm the diffuseness of the liquid surface, the abruptness of the solid-liquid interface, and the molecular short range order at the liquid surface. Overheating of solid NaCl(100) should be directly observable. So might the temporary settling of liquid mini-droplets. Moreover, the much larger solid surface entropy should cause the partial wetting angle of liquid on solid NaCl to *increase*, rather then decrease with temperature.

Part II

Nanofriction at high temperatures

Chapter 6

Nanotribology—hard tips sliding on a hot NaCl surface

As extensively shown in Part I, NaCl(100) has the peculiarity of being a nonmelting surface, that retains a strong crystalline stable state up to and even beyond T_{M}.

In this part of the thesis, I will investigate a useful potential application for a surface with these properties, in the field of nanofriction. Nanofriction is the friction felt by a tip, whose atomic size allows the scanning of surface areas of nanometric size. Nanotips can explore a small but crystallographically very well defined piece of surface, thus overcoming a standard problem in the general field of friction, namely that the surfaces in contact are generally non uniform and therefore somewhat ill defined, representing an important drawback of most frictional studies.

6.1 Motivation

Thanks to the advent of increasingly sophisticated tip-based tools, the physics of nanofriction is becoming an issue of growing importance, albeit one that received insufficient attention by the community so far. There is in particular a need for a deeper understanding of the physics of friction in extreme regimes including very high temperatures (HT) where the sliding materials may approach their melting points. In everyday life, very high frictional temperatures are in fact routinely attained in a variety of situations including machining, motors, braking, etc [119].

While rather complex phenomena are generally involved in many such practical situations, at the fundamental level even the very basic microscopic frictional processes taking place close to the substrate melting point have not yet been intimately explored, characterized and understood. For bare metals on metals, for example, a *drop* of wear-related friction is generally reported, and reasonably attributed to softening caused by high flash temperatures ("if one could move fast enough, one could ski on copper mountains..."[120]), but has not been otherwise pursued with surface science standards. Conversely, dry friction between hard materials has been known to *rise* at HT, ostensibly due to the onset of some diffusion [120]; but again that has not been further followed up microscopically. At the present stage, it is just not clear when, how and why closeness to the melting point will imply a drop or a rise of frictional forces under controlled and well defined microscopic contact circumstances. Nanofriction studies presently offer a fresh opportunity to address the microscopic physics behind these phenomena.

6.2 Advantages of using hot NaCl(100) as a substrate

In this thesis I started a first exploration of possible scenarios, obtained by addressing high temperature nanofriction through simulation and theory. For a meaningful case study, we should first of all qualify and specialize our choice of surfaces and tips. In fact, close to the bulk melting point T_{M}, most solid surfaces wet themselves – in full equilibrium conditions and without any perturbing tips – with a microscopically thin film of melt (surface melting) [112]. Such a liquid film will as a rule give rise to the sudden "jump to contact" of the surface with the tip long before closest approach – to some extent ruining the experiment, as was indeed observed [121, 122] (see Fig. 6.1) and predicted [123] long ago (see Fig. 6.2). In order to avoid this generally unwanted complication, one might for example resort to tips that are not wetted by the substrate. Alternatively one could choose to study a hard, *nonmelting* crystalline face exhibiting no spontaneous surface melting at all, one that will spontaneously remain solid and crystalline up to T_{M} [112]. One extra advantage of this last choice is the possibility to distinguish between very different frictional regimes, such as deep ploughing friction (involving heavy wear) and superficial grazing friction (wearless), a distinction otherwise made impossible by surface melting. This will therefore be the approach followed in our work. In doing that we moreover discarded inhomogeneous surfaces that are simply prevented from melting by some kind of

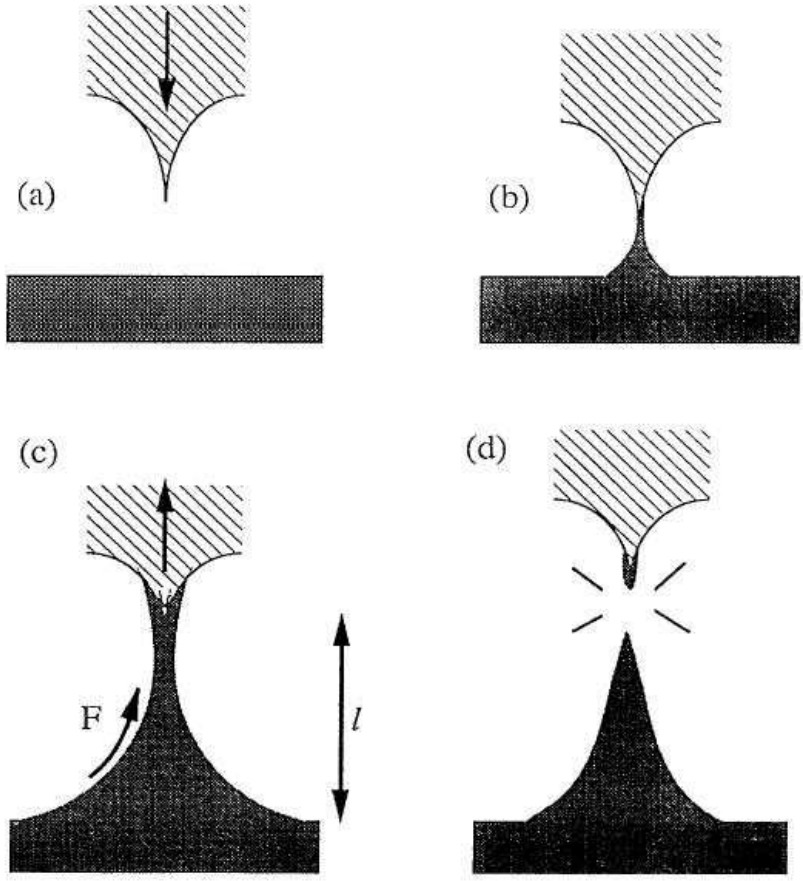

Figure 6.1: Schematic cycle of formation and rupture of surface-tip contact in experiment. (a) Approach to the tip. (b) Just after the jump to contact. (c) Growth of the neck. (d) Breaking of the neck. From Ref. [122]

protective coating, for they will be – unlike the intrinsically nonmelting homogeneous crystal surfaces – very difficult to control. Eventually, a very stable alkali halide surface such as NaCl(100) proved close to an ideal choice – at least theoretically – because of its extreme and recently understood nonmelting habit [124]. One added bonus is that salt does not wet a standard tip, which has made it already a choice substrate for abundant experimental nanofriction work at room temperature [116].

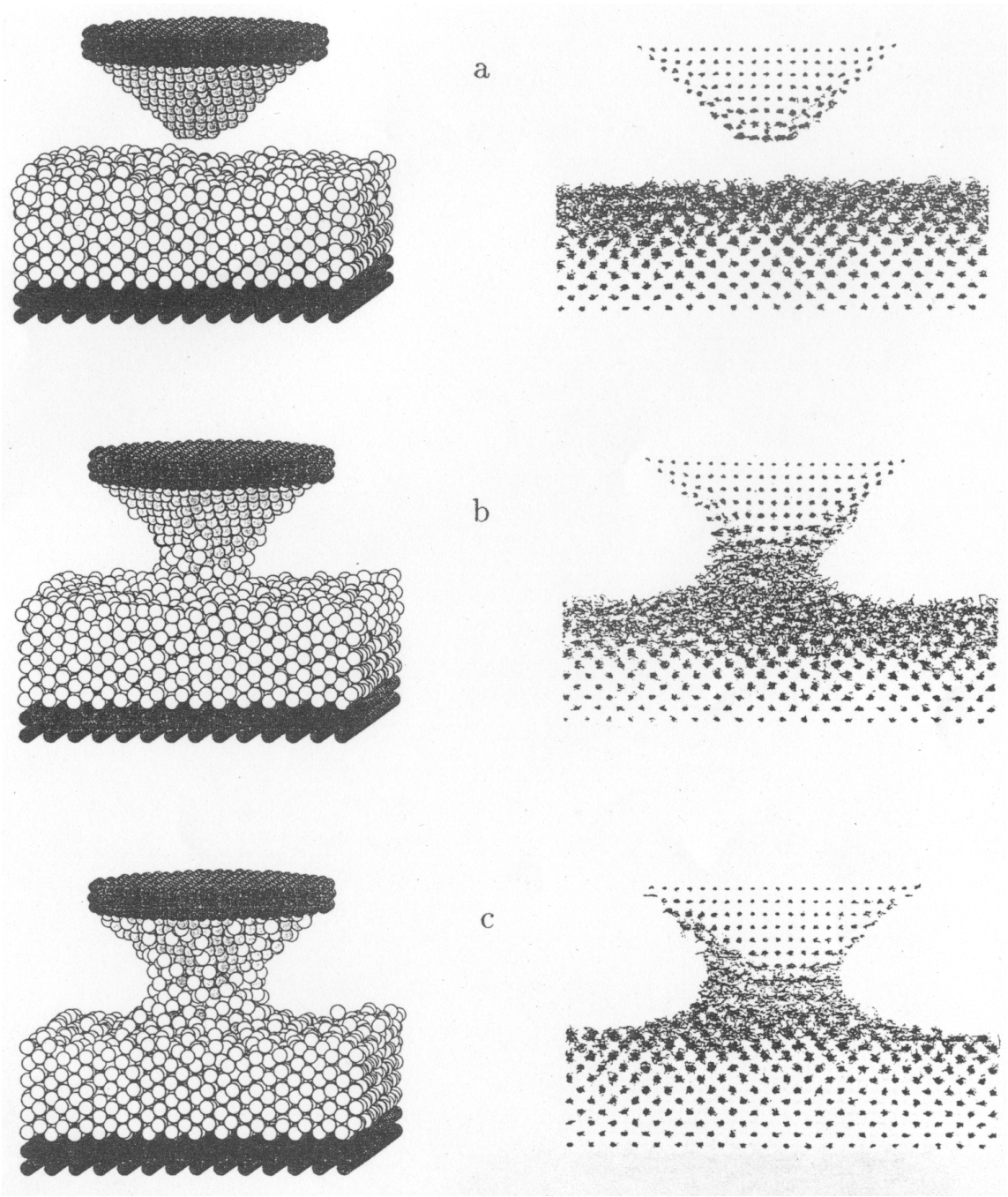

Figure 6.2: Gold tip in contact with Pb(110) surface. Instantaneous atomic configurations (a) initial formation of a neck at 300 K and (b) final stage with a well defined liquid neck of diameter 5.6 Å at 600 K. From Ref. [123]

6.3 Tip implementation

For our nanofriction simulations, we consider the tip apex materials which are commonly used in AFM wear experiments,such as diamond or tungsten. For

convenience, it is possible to assume that the tips are infinitely hard since the tip deformations are negligibly small compared to more pliable alkali halide surfaces [120] and the wear of indenter is not considered. The simulated tips were chosen rigid with a diamond structure and diamond room temperature lattice spacing. For deep wear simulations we created a conical tip atomically sharp on top, composed of $\sim$ 400 atoms. The diameter and height of the tip are shown in Fig. 6.3). On the contrary for light grazing wearless friction we use a completely blunt flat tip composed of $\sim$ 200 atoms (see Fig. 6.3). The flat surface of the tip has a (111) plane of 13Å diameter roughly. The empirical potential used to describe

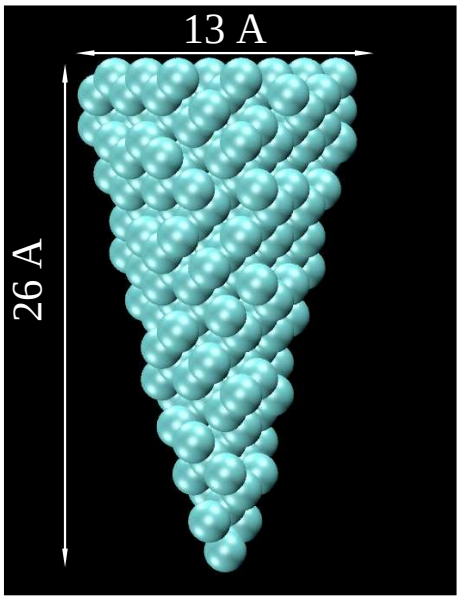

Figure 6.3: Rigid diamond tip constructed for the deep penetration. The tip length is $\sim$ 26Å, the diameter is about 13 Å, the total number of C atoms is 400 atoms.

tip-surface interaction was a pairwise Buckingham potential:

$$V(r_{ij}) = A_{\alpha\beta}\exp(-B_{\alpha\beta}r_{ij}) - \frac{C_{\alpha\beta}}{r_{ij}^6} \tag{6.1}$$

where $A_{\alpha\beta}$, $B_{\alpha\beta}$ and $C_{\alpha\beta}$ are parameters, determined on the basis of physical properties of materials. Table 6.1 gives the values of parameters for $Na-C$ and $Cl-C$ potential after by Tang *et al* [125]. An independent check was done for the Van der Waals interaction term C by fitting to the Hamaker constant (see Appendix B). The adhesion of the flat diamond tip is found to be $\simeq$ 0.7 eV at an equilibrium distance of 3 Å. The slight modification of the given model potential is obtained taking into account the polarization effects of the diamond apex

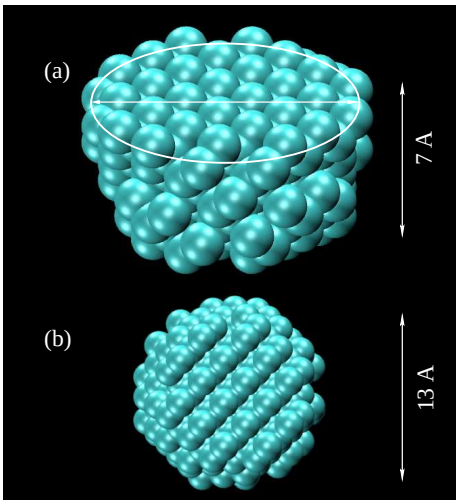

Figure 6.4: Rigid diamond tip constructed for the wearless friction. (a) Side view; (b) Top view. The tip length is $\sim$ 7Å, the diameter is about 13 Å, the total number of C atoms is 200 atoms.

	Na-C	Cl-C
A (eV)	741.92	1287.75
B ($Å^{-1}$)	4.51	3.00
C (eV $Å^6$)	3.016	52.533

Table 6.1: Parameters of Buckingham potential for NaCl-C proposed by Tang *et al*. From Ref. [125].

in the presence of surface electric field. This was done by introducing an additional term $\frac{\alpha}{r_{ij}^4}$ (where α is a static dipolar polarizability of the carbon atoms). The chosen cutoff of the potential is 10Å.

It is important to emphasize that we did not attempt to construct a realistic tip equipped with a cantilever. Moreover we slid our tips at constant velocities and therefore the stick-slip effects were not allowed.

Chapter 7

Ploughing friction on NaCl(100)

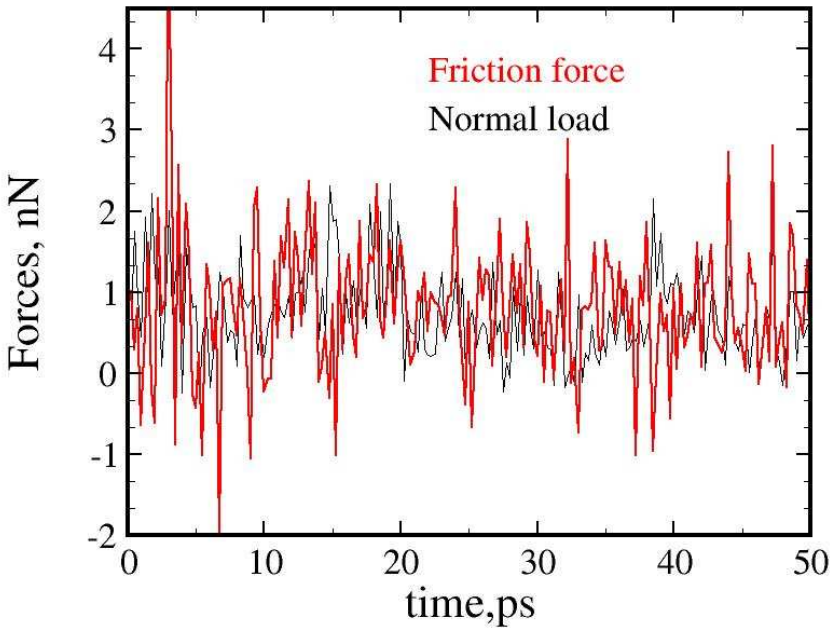

Figure 7.1: The instantaneous loading and friction forces at 300 K during a typical run.

The first series of runs were devised to study the dependence of the wear on temperature. We indented the surface with a sharp tip and slid at a constant velocity v (generally between 25 and 50 m/sec) parallel to the NaCl(100) with no allowance for any internal mechanics of tips or for cantilevers (no stick-slip). The NaCl(100) surface was 60×60Å^2 in lateral size, while the contact area of the sharp tip was much smaller. Under constant load especially at high temperatures the tip penetration would increase steadily with time and with temperature. To avoid

that, we chose to work in a constant penetration mode, the sharp tip edge entering the NaCl surface a fixed depth $d \sim 6$ Å. Initially the tip is placed at ~ 8Å distance from the surface. During first ~ 30 ps the tip approaches the surface and indents in. Next 15 ps we equilibrate the sample at constant temperature and then carried out the ploughing simulation. The forces both the vertical and in plane, were left

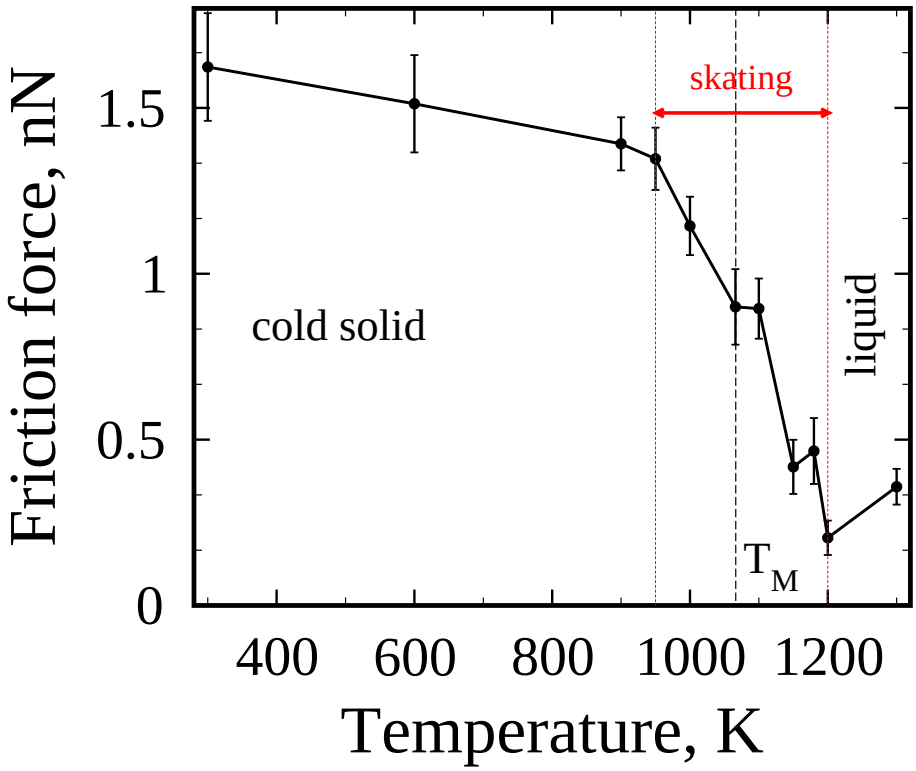

Figure 7.2: The friction force as a function of temperature at ~ 6 Å constant penetration depth. The tip's velocity is 50 m/sec.

free to fluctuate. Fig. 7.1 shows the typical ploughing friction force $F_x(t)$ and the corresponding vertical "load" force $F_z(t)$ felt by the ploughing tip at various temperatures. The large noise is clearly related to the discontinuous nature of wear, including the formation and displacement of debris, pushed onward and out of the way by the moving tip. As a function of temperature, the frictional force of Fig. 7.2 clearly shows two regimes.

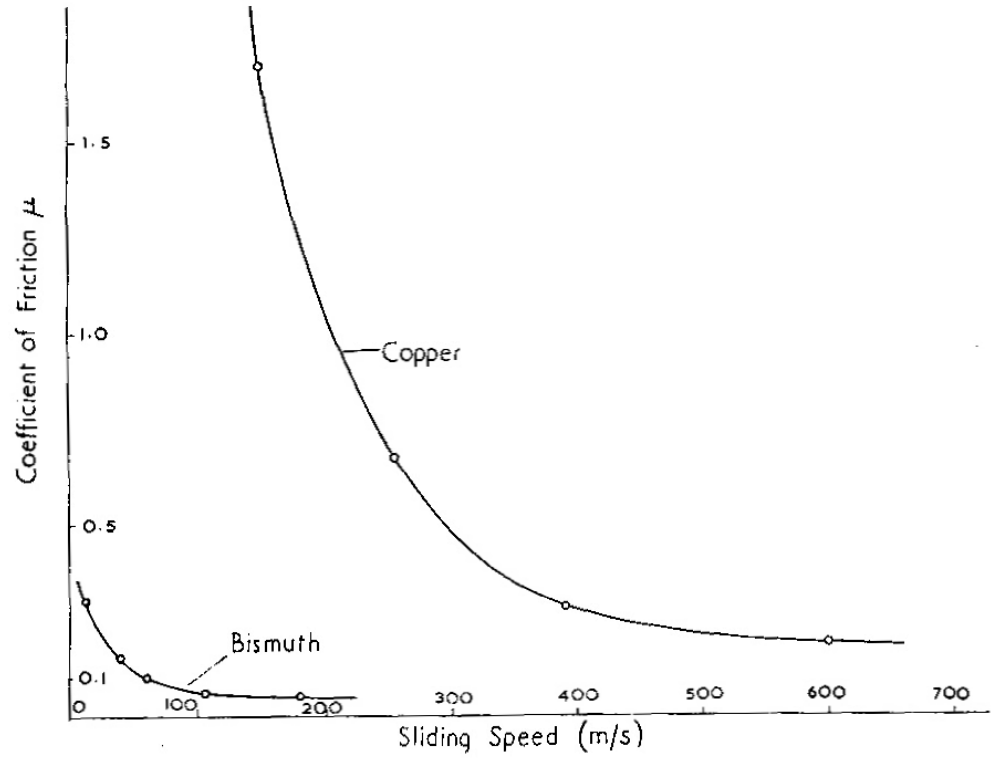

FIG. 236. Friction of steel on copper (load 10 gm) and on bismuth (load 30 gm). Continuous deceleration experiments.

Figure 7.3: The friction of steel on different metals, showing a drop for increasing speed due to softening caused by the high contact temperature. From Bowden and Tabor Ref. [120]

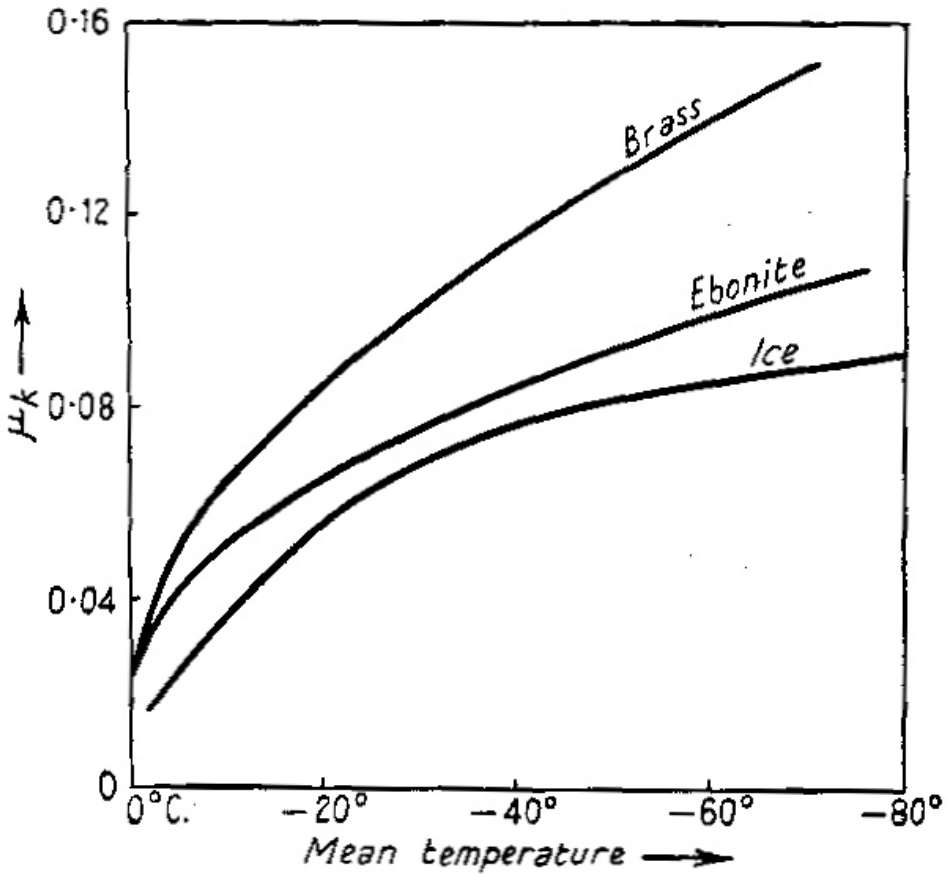

Figure 7.4: Wear of various materials on ice. The friction drops sharply as the melting point is approached (which permits ice skating). Temperature increases to the left. From Ref. [120]

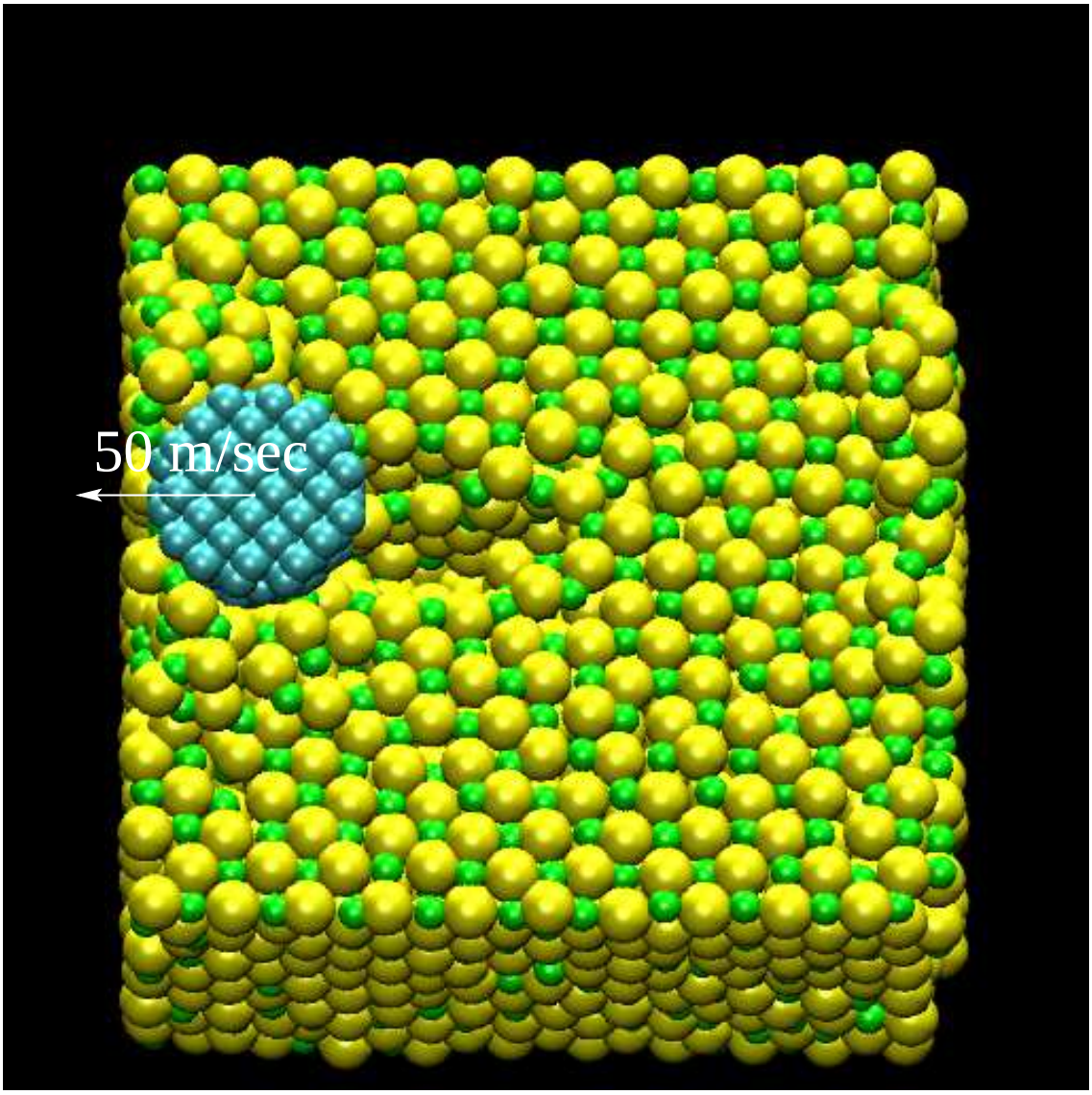

Figure 7.5: Tip scratching NaCl(100) at $T_{\mathrm{M}} - 150$K. The scribing feed is ~ 6Å the scratching speed is 50 m/sec. The trace remains solid and visible. Light blue spheres state for C, green— for Na^+ and yellow—for Cl^- respectively. The tip moves to the left.

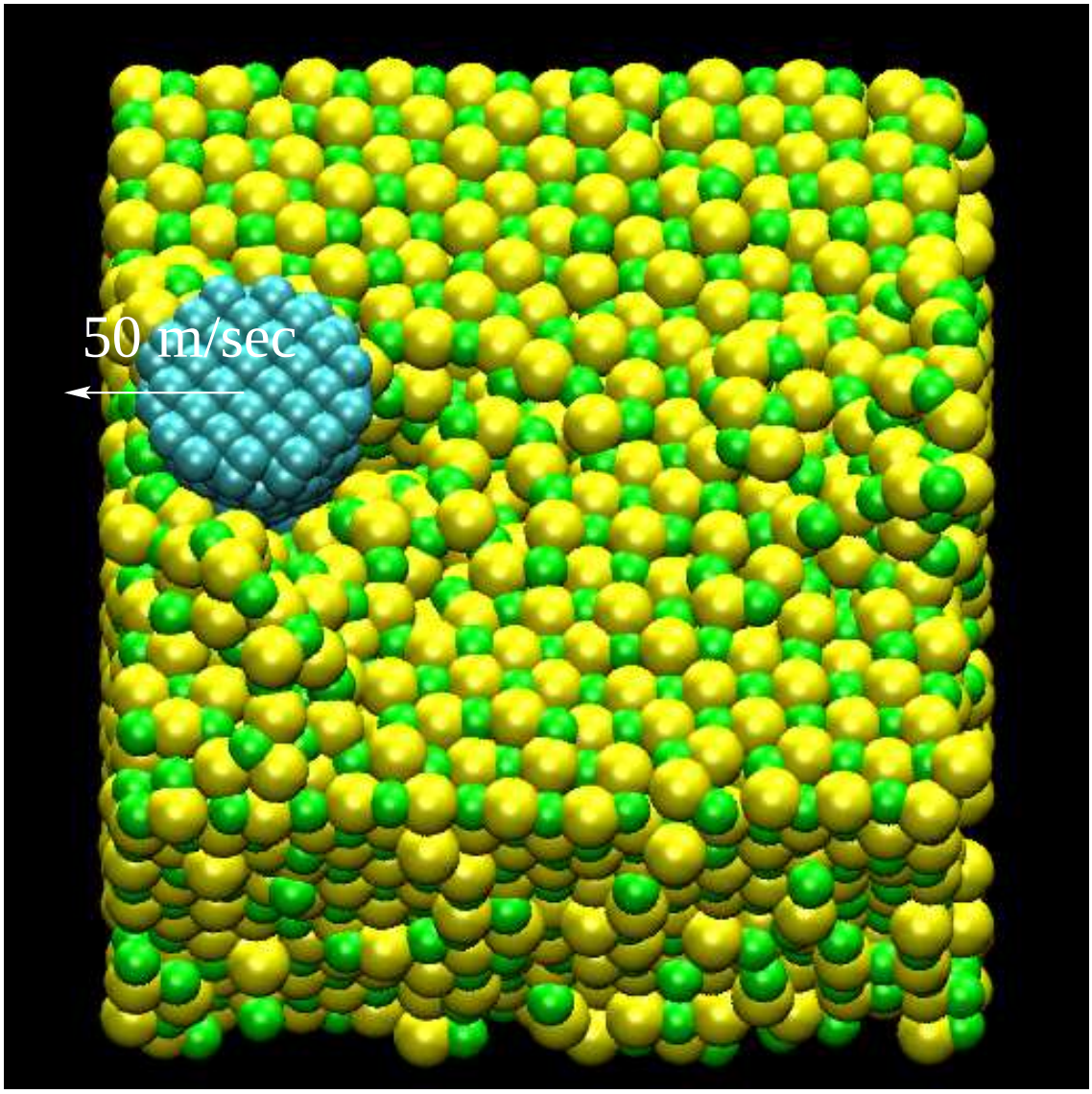

Figure 7.6: Tip scratching NaCl(100) at $T_{\mathrm{M}} + 150$K. The scribing feed is $\sim$ 6Å the scratching speed is 50 m/sec. The trace closes fastly behind the tip, surrounded by a local liquid cloud. Light blue spheres state for C, green— for Na^{+} and yellow—for Cl^{-} respectively. The tip moves to the left.

Up to $T_{\rm soft} \sim 900\,$K it is basically constant, corresponding to $\mu = \langle F_x/F_z \rangle \sim 1.2$. The high friction forces can be attributed to the breaking and reforming of the atomic bonds and the absence of any lubricating film or contaminant between the sliding surfaces (see Fig. 7.5). Above $T_{\rm soft}$, friction force F_x drops sharply by a factor of at about 3, and remains low across the $T_{\rm M}$ and all the way to $T_{\rm SS} \sim 1200\ K$ where the surface spontaneously melts. The drop of friction above $T_{\rm soft}$ resembles the experimental one reported for metals (see Fig. 7.3) on metals, and is even more reminiscent of that observed for hard sliders on ice – ice *skating* (see Fig. 7.4,7.7) [126]. The friction in last case may be remarkably low μ =0.1. The large influence of temperature on friction of ice is in contrast to the behavior of most other solids where temperature has only a small effect. The traditional view is that the low friction is due to a lubricating water layer, and the effect is marked in ice since the underlying material retains its rigid character even though the surface layers are molten.

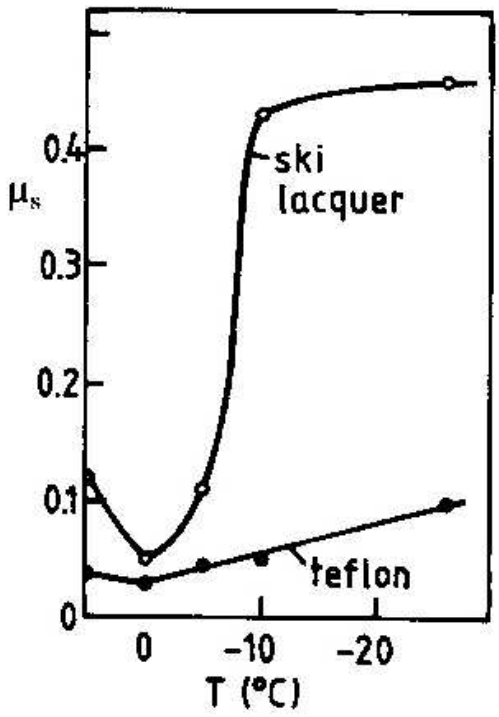

Figure 7.7: The dependence of the static friction coefficient on temperature for skis on snow. From Ref. [126]

In our simulation, we find that the frictional drop is accompanied by – and likely due to – a thin cloud of displaced Na and Cl ions which surround the tip

and have liquid-like mobilities (see Fig. 7.6). At low temperatures the furrow behind the apex rapidly reconstructed to reform (100) facets. Gnecco *et al* has even observed experimentally the reconstruction of the debris in stepped pyramid [116]. The characteristic time of the quasi-liquid trace existence behind the tip depends strongly on temperature and varies from 100 fs (at 300 K) to 5 ps (at 1150 K). Coated by this nearly liquid shroud (Fig. 7.8 shows the tip surrounded by a thin liquid cloud) the tip effectively skates. The ease with which the tip wades

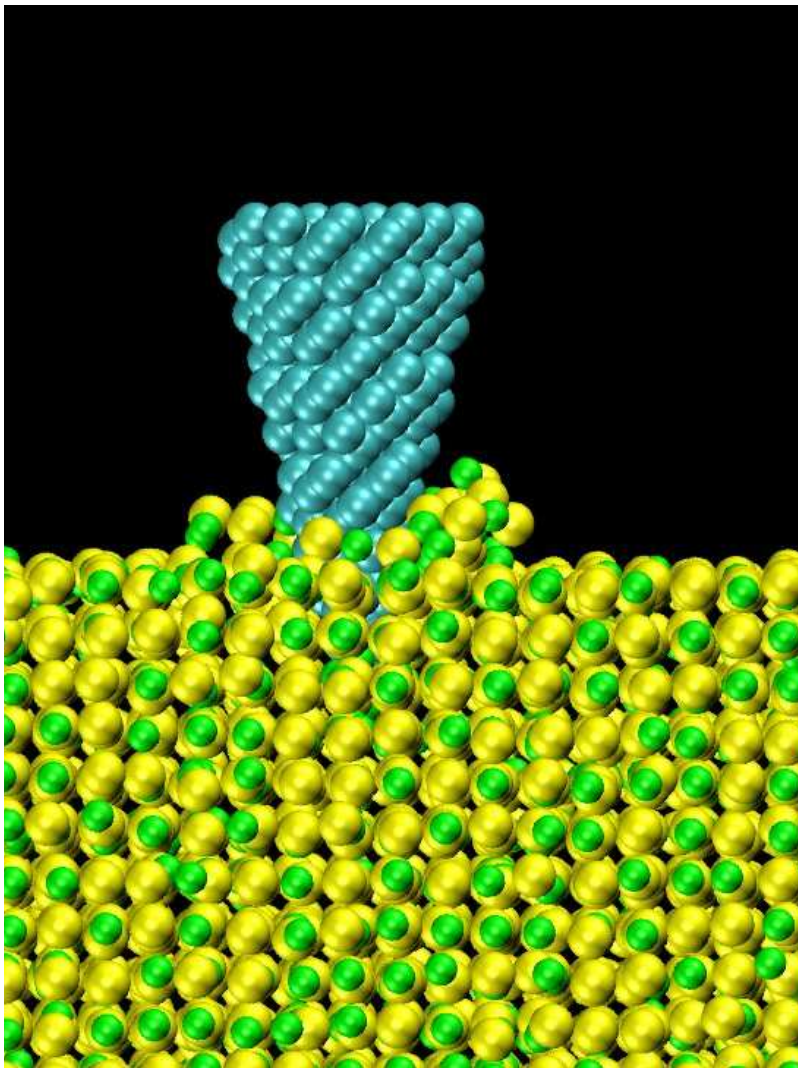

Figure 7.8: At T_{M} a penetrating tip moving through solid NaCl(100) is accompanied by a local liqiud cloud that moves with it. Light blue spheres state for C, green— for Na^+ and yellow—for Cl^- respectively.

through the solid is remarkable, particularly since in this regime the furrow (very well defined below T_{soft}) heals out spontaneously, leaving a perfect solid surface behind itself.

An approximate frictional energy balance can be made very easily e.g., at 300 K. $F_x \sim 1.5\,\mathrm{nN}$ over a sliding length of 60 Å yield a total of $\sim$ 60 eV. The furrow surface plus that of the debris is roughly 1000 Å^2, which with a surface energy $\gamma \sim 0.2$ J/m^2 yields 12 eV or about 20% of the total. If we consider the energy stored in internal deformations to be negligible, the remaining 80% is dissipated as heat, a rather typical figure in the literature [126].

Chapter 8

Wearless sliding friction on NaCl(100)

8.1 Influence of the pressure produced by tip on NaCl(100) nonmelting

A second series of simulations were devoted to the grazing friction phenomena at high temperatures. As we discussed above, we employed here a flat tip (see Fig. 6.3) of area $\sim$ 200 Å gently pressed with a 1 nN force over the surface. First of all, we checked the influence of the superincumbent tip on NaCl(100) shown on Fig. 8.1. Applying a normal load of 1 nN we have observed below the tip a increased local reluctance of the solid surface to melt (see Fig. 8.2). Indeed a hydrostatical stress of 5 kbar shifts the original melting point on 160 K above T_{M}. Nevertheless the pressure is only partly hydrostatic (uniaxial stress lowers the melting temperature instead) and the overall effect is not major.

8.2 Wearless sliding

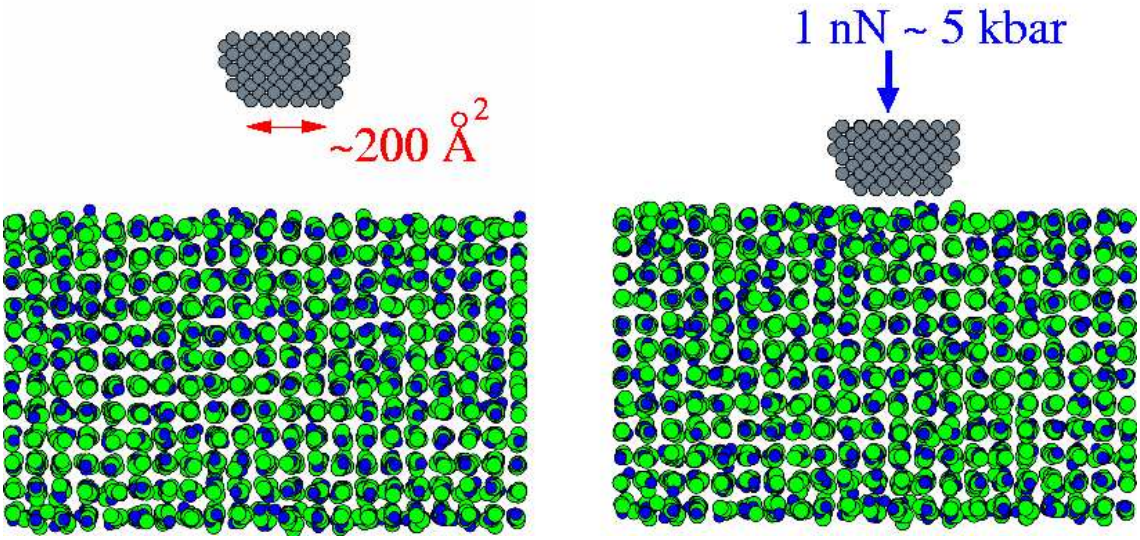

Figure 8.1: NaCl(100) under 5kbar pressure induced by the diamond tip at T_{M}. Light grey spheres state for C, green— for Na^+ and blue—for Cl^- respectively.

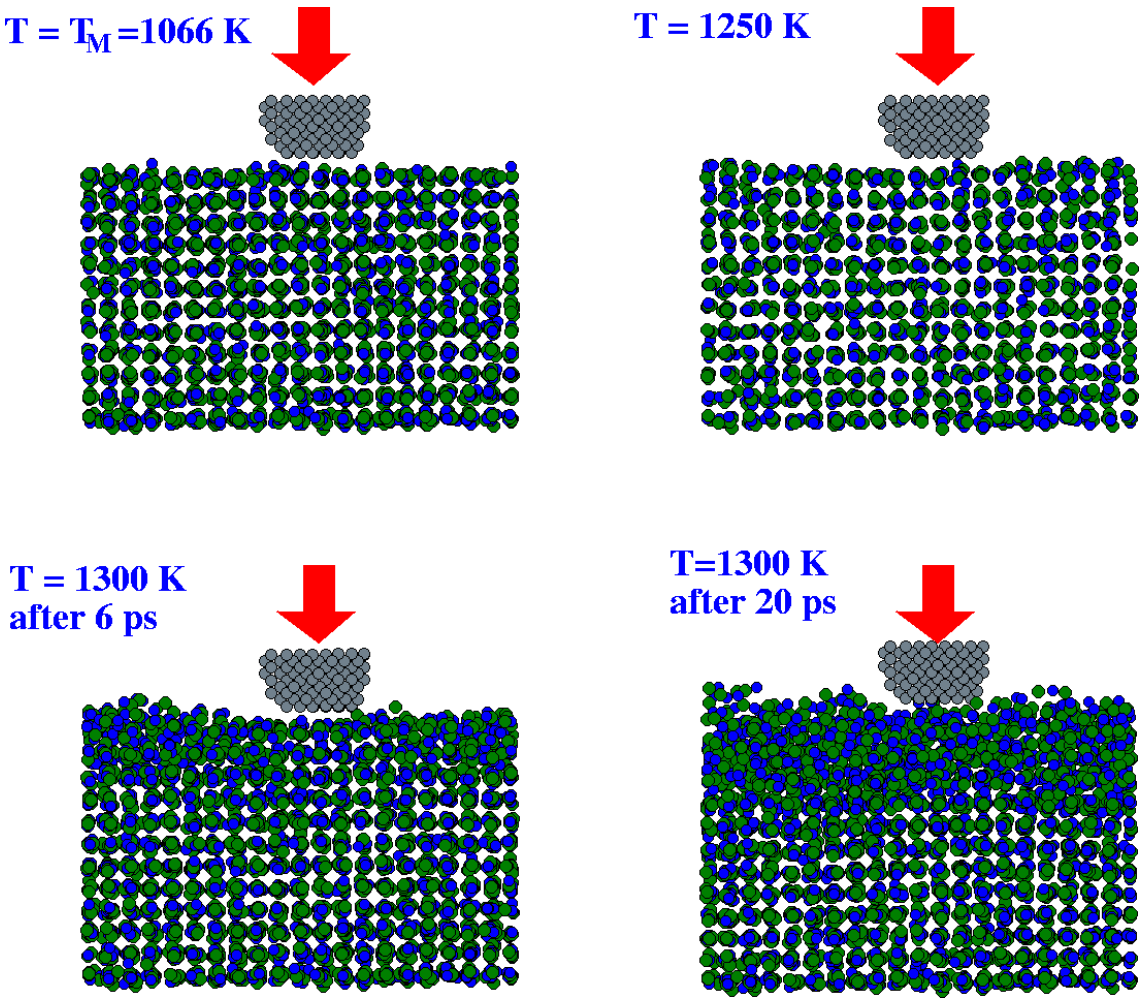

Figure 8.2: The pressure of 5 kbar delays melting even above surface spinodal point $T_{SS} \simeq 1210$ K. Light gray spheres state for C, green— for Na^+ and blue—for Cl^- respectively.

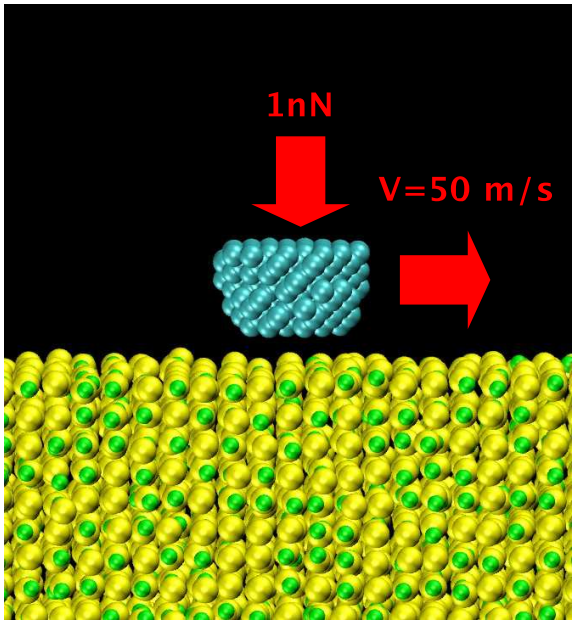

Figure 8.3: The snapshot of the blunt tip sliding on NaCl(100). Light blue spheres state for C, green— for Na^+ and yellow—for Cl^- respectively.

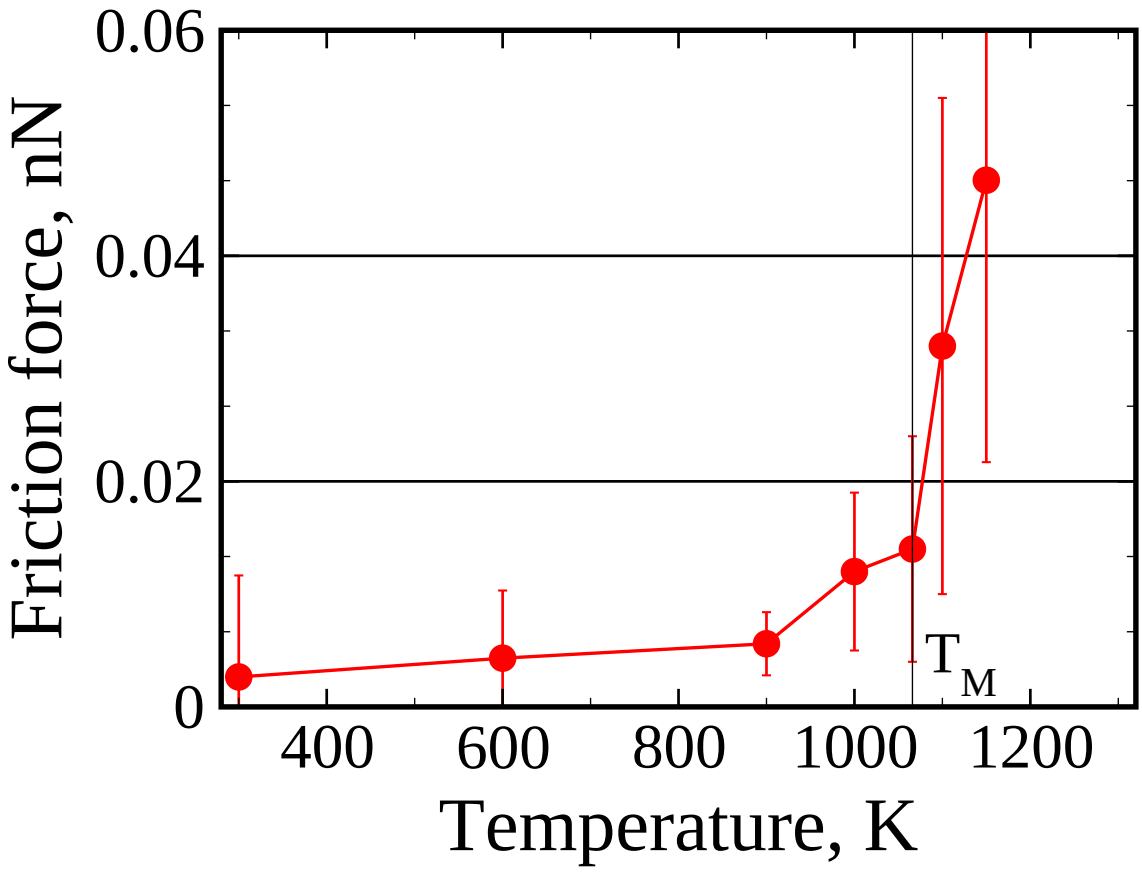

Figure 8.4: Frictional force of a grazing tip on NaCl(100). Note the very low friction, sharply increasing at T_{M} and above.

Next we carried out the grazing frictional runs again with a constant speed of 50 m/s and a fixed load of F_z= 1nN (see Fig. 8.3). At low temperatures the frictional force $F_x(t)$, though strongly fluctuating, averages to a very small value, $\mu = \langle F_x \rangle / F_z$ = 0.007 at 300 K. The frictionless sliding of two hard incommensurate crystal lattices known as "superlubricity" [127] and recently observed for a rotated graphite island on graphite [128] is most likely responsible for this low value. We have checked that changing the orientation of the tip with respect to substrate influences the value of friction. As temperature grows (Fig. 8.4), an initially moderate thermal growth of μ up to 1000 K is replaced by a relatively dramatic surge near T_{M}. Since a solid friction will eventually disappear giving way to viscous damping when the surface eventually melts, this surge represents a frictional peak, which contrasts with the drop observed for ploughing friction in the same temperature regime.

8.3 Theory of high temperature wearless friction

As the simulations show, the sliding of an adsorbate island, or of a very lightly pressed flat tip on a hard nonmelting surface terrace can take place without causing appreciable wear even close to the melting temperature, at least for nanometric sliding distances. The friction coefficient is correspondingly very small, the tip lattice and the surface lattice being mutually incommensurate "superlubricity" [127, 128]. In our example, a flat tip of area $\sim 200\text{Å}^2$ can experience a grazing friction coefficient one to two orders of magnitude smaller than the sharp penetrating tip, during ploughing, despite the latter's atomic size. Ploughing friction is principally a matter of wear, the tip leaving behind itself a furrowed surface – a different state from the initial flat surface – whereas the grazing frictional dissipation is quite different, and much gentler. Here the energy is dissipated mostly through the generation of phonons in the solid substrate (and in the tip), plus some modest tip-induced drift of diffusive surface atoms that might take place at high temperature. As a result, the surface behind the moving tip is left, after dissipation of the small amount of frictional heat, very much in the same state it was previously.

This observation justifies an attempt at treating grazing friction within linear response theory, namely assuming a steady state with negligible influence of the tip on the surface. While the details of this line of theoretical attack still require some work, the general idea is quite standard, and is in fact the same as that of a Stokes particle floating in a fluid.

A tip in contact with the hot surface will experience random forces – Brownian kicks. Were the tip free to move along (xy), these random forces would cause planar Brownian diffusion, characterized by a 2D tip diffusion tensor $D_{\alpha\beta}$. Accordingly, after a time t the tip would have diffused (ignoring for the time being the tensor aspects) a mean distance $\sqrt{4tD}$. From very general thermodynamic principles, there should be an Einstein type relationship, such as $\eta = k_B T/MD$ connecting the tip diffusion D with the tip friction η, describing phenomenologically the dissipative force η experienced by the tip when subjected to an infinitesimal drift velocity v in the (xy) plane.

Rather than the tip diffusion D, which would make a hard quantity to measure in simulation, we would now like to relate the friction η to properties of the substrate surface alone. To that end, we observe first that as is well known, from a

simple Langevin equation

$$M\ddot{\mathbf{R}} = -\eta M\dot{\mathbf{R}} + f(t) \tag{8.1}$$

for the motion of the tip of coordinate R one can extract the property [129] that the zero frequency self correlation of the random force $f(t)$ affecting any Brownian particle is directly related to friction, in the simple form

$$\eta = (1/3Mk_BT)\int_0^\infty dt\langle f(t)f(0)\rangle \tag{8.2}$$

This result relies, as detailed in e.g. in Ref. [129], on the usual assumption $\langle f(t)\rangle = 0$.

Assuming linear response, and a negligible tip influence over the surface, the random force can be written as a linear expression of the surface atom velocities u_i(t). Following Ying *et al* [130] it is convenient to move to 2D k-space:

$$u_i(t) = \int d\mathbf{q}u_{\mathbf{q}}(t)e^{i\mathbf{q}\cdot\mathbf{R}_i} \tag{8.3}$$

and write the random tip force in the form

$$f(t) = \sum_{\mathbf{q}} C_{\mathbf{q}}u_{\mathbf{q}}(t) \tag{8.4}$$

where $C_{\mathbf{q}}$ is a coupling function expressing the assumed linear relationship between the substrate atoms kicks onto the tip with individual velocities $u_i(t)$ and the overall instantaneous random force $f(t)$ felt by the tip. Inserting this expression into the equation for η, we obtain

$$\eta = \frac{1}{3Mk_BT}\sum_{\mathbf{q}}|C_{\mathbf{q}}|^2\int_0^\infty dtu^\star_{-\mathbf{q}}(t)u_{\mathbf{q}}(0) \tag{8.5}$$

$$= \frac{1}{3Mk_BT}\sum_{\mathbf{q}}|C_{\mathbf{q}}|^2 S(\mathbf{q},\omega=0) \tag{8.6}$$

where $S(\mathbf{q},\omega=0) = \int_0^\infty dtu^\star_{-\mathbf{q}}(t)u_{\mathbf{q}}(0)$ is the two dimensional dynamical structure factor of the tip-free surface substrate, measuring the substrate atom velocity-velocity correlation functions. In this manner, the grazing friction η is reduced to a property of the unperturbed surface. This result closely parallels the more complete one developed by means of the memory function formalism by Ying and collaborators[131, 130]. However, in the simple present form, it could also be arrived at directly by observing that the dissipation rate should in linear response theory take a Fermi Golden rule form,

$$1/\tau = \frac{2\pi}{\hbar}\sum_{\mathbf{q}}|C_{\mathbf{q}}|^2\chi''(\mathbf{q},\omega=\omega_{pert}) \tag{8.7}$$

where C measures the perturbation strength, and $\chi^{''}$ is the density of final states, here expressed by the dissipative part of the system's linear response function. The latter is in turn related to the dynamical structure factor through the fluctuation dissipation theorem [129]

$$\chi^{"}(\mathbf{q},\omega) = \frac{\pi\omega\rho}{k_B T} S(\mathbf{q},\omega) \tag{8.8}$$

where ρ is the density. Considering that the frequencies that are relevant for dissipation (long wavelength phonons and diffusional processes) are extremely small compared to e.g. the solid substrate Debye frequency, one can set ω =0 recovering (disregarding factors) the result Eq.(8.5) above.

Our scope here is to make use of the linear response approximation Eq.(8.5) to relate the grazing friction to the tip free dynamical surface properties. The coupling $C_{\mathbf{q}}$ is in principle a complicated function of the tip shape, and of the detailed forces between tip and surface. In our case of a large lateral tip size L ($L \sim 13\mathring{A}$) however, all $\mathbf{q}$ component of short wavelength will average out (similarly to a large ship averaging out all waves of shorter wavelength than its length) so that the relevant $\mathbf{q}$ values where $C_{\mathbf{q}}$ is nonzero will be restricted to $|\mathbf{q}| < 2\pi/L$ or roughly $|\mathbf{q}| < 0.5\text{Å}^{-1}$. A simple approximation could be for instance to assume

$$C_{\mathbf{q}} = C_0[1 - \theta(q - 2\pi/L)] \tag{8.9}$$

Since $2\pi/L$ is small, an even simpler approximation could be

$$C_{\mathbf{q}} = C_0\delta(\mathbf{q}). \tag{8.10}$$

With this choice we finally obtain

$$\eta = \frac{1}{3Mk_BT}|C_0|^2 S(\mathbf{q}=0,\omega=0) = \frac{1}{3Mk_BT}|C_0|^2 \sum_{ij}\int_0^\infty dt\langle u_i(t)u_j(0)\rangle \tag{8.11}$$

The velocity-velocity correlation functions can be extracted from simulations. Fig. 8.5 shows $\int S(\omega\to 0)dq$ extracted by an independent simulation of the NaCl(100) surface as a function of temperature. Although this is not exactly $S(\mathbf{q}=0,\omega=0)$ as required by Eq.(8.11), it can still be used for qualitative illustration.

For the slab case, which comprises surface atoms, there is a sharper rise close to T_{M} and $\omega \to 0$, attributable due to large and catastrophic softening of the very anharmonic surface lattice, still solid but extremely compliant in this regime. Comparison with Fig. 8.4 is qualitatively good, indicating this increase of compliance

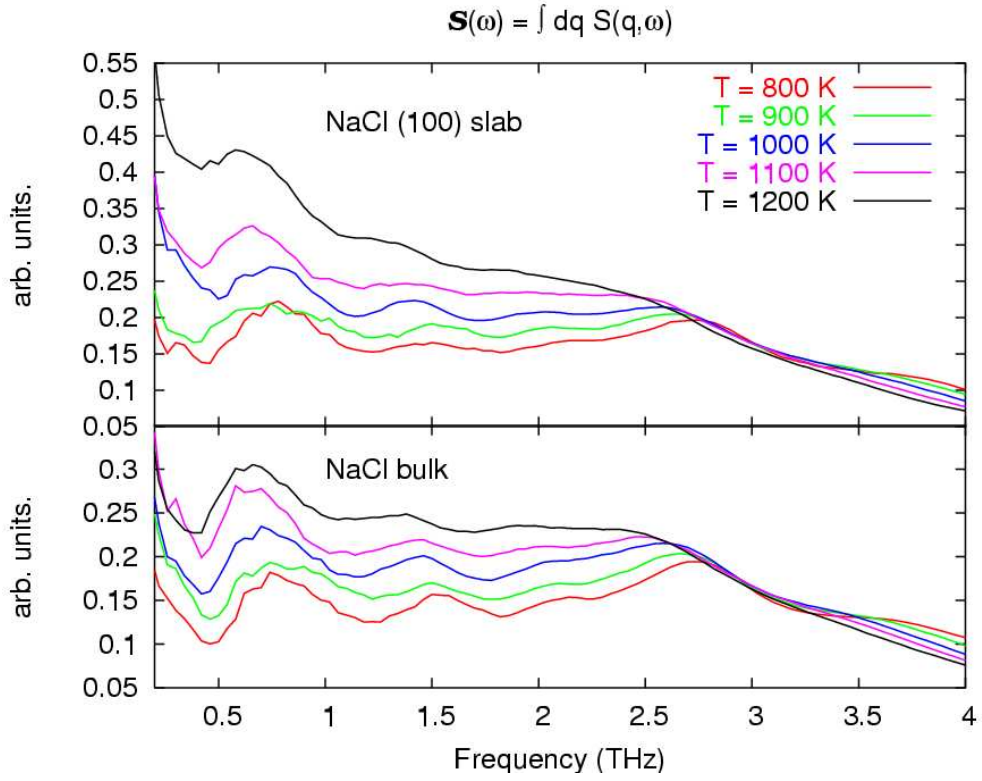

Figure 8.5: Dynamical structure factor as a function of temperature in rocksalt bulk (lower panel) and in slab (upper panel).

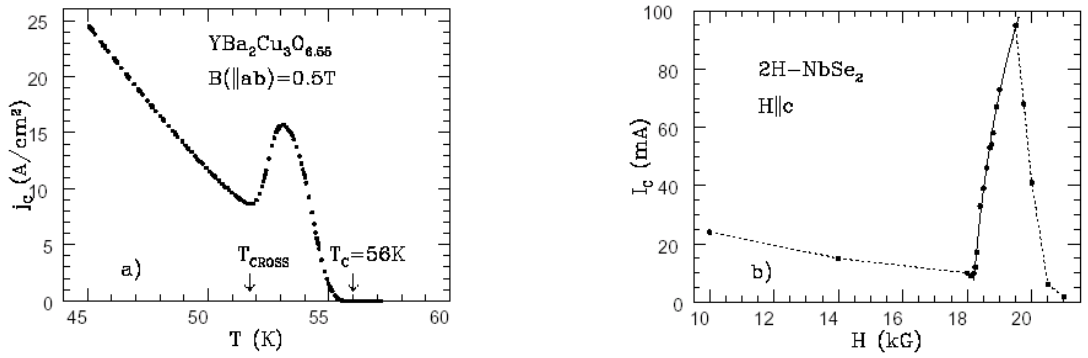

Figure 8.6: Peak effect in superconductors of type II showing that friction has a peak when the flux lattice is the softest.

as the reason for the high temperature peak of grazing friction. This may provide a microscopic explanation of macroscopic observations of high temperature frictional increase of hard sliders.

Flux lattice friction in superconductors of type II

We note that a well known analogue of the phenomenon we just described exists in the physics of type II superconductors close to H_{c2} (see Table 8.1). Here the flux lattice, whose frictional depinning from the ion lattice and impurities determines the critical current, turns very soft before eventually disappearing [132] (see Fig. 8.6). This soft state is so very compliant that the pinning force, and the critical current with it, suddenly develops a last sharp peak before dropping to zero at H_{c2}, a phenomenon that has been described by very similar formulas to those of sliding friction [130]. It is thus reasonable to propose that the high temperature friction increase of a hard grazing slider that we just described is the direct frictional analogue of the peak effect in superconductors.

Conclusions of part II

The high temperature nanofriction behavior of a sliding tip on a hard dry solid surface near the bulk melting point T_{M} was so far unexplored. We conducted case study simulations of hard tips sliding on hot NaCl(100), a nonmelting surface, revealing two distinct and opposite phenomena. Deep ploughing friction of

System	Mechanical Friction	Vortices in SC
Movable objects	Surface lattice	Vortex lattice
Driving force F_d	Mechanical force F_d	Lorentz force $\sim j$
Static friction F_s due to	Soft surface lattice	Soft vortex lattice
Critical parameter (max F_s)	Maximum static friction F_s^{stat}	Critical current density j_c
Static resistance	Static friction F_s	Pinning (F_{pin})

Table 8.1: Correspondence between mechanical friction and friction for vortices in SC. After Ref.[133]

a sharp tip shows a drop of the frictional force close to T_{M}, where the tip wades or skates through the hot solid, accompanied by a small moving liquid cloud, the furrow behind promptly healing and recrystallizing. At the opposite limit, the grazing (wearless) friction of a flat tip shows on the contrary a sharp surge of the initially weak frictional force as the surface lattice, still solid, turns increasingly compliant near T_{M}. This surge can be understood as a nanofrictional analogue of the celebrated peak effect of sliding vortices in the mixed state of type II superconductors.

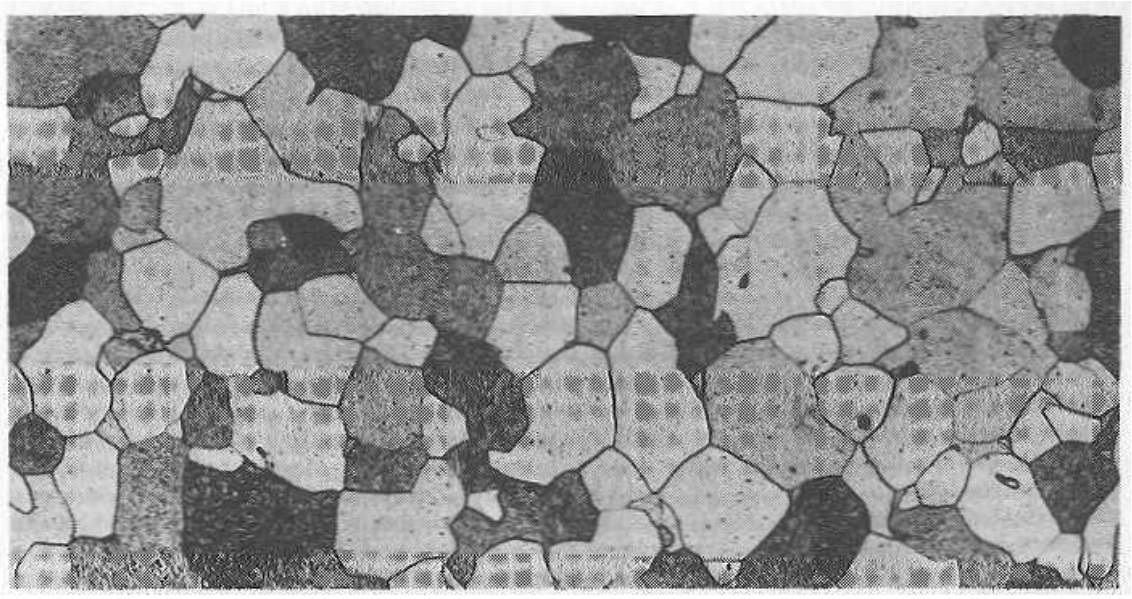

Figure 8.7: An example of polycrystalline copper surface. In macroscopic friction the melting facets can lubricate the surface reducing the friction like in skating. From Ref. [120]

We believe that these phenomena should be more general than the specific context in which they emerged. In particular, most metals possess at least one close packed nonmelting surface, such as Pb(111) or Al(111) [112]. Nanofriction on that surface should behave quite similarly to our results on NaCl(100).

High temperature experiments on an alkali halide like NaCl should be possible. Unlike the metals, because of a high vapor pressure (0.34 mmHg for NaCl at $T_{\rm M}$), and of the correspondingly high rate of evaporation 1.7×10^{-5} s^{-1}, for terraces 50Å wide, the step flow velocity at sublimation conditions at T=$T_{\rm M}$ will be about 10^{-5} m/s. So long as the tip velocity is larger than this value, our description of nanofriction is fully applicable. However, we note that irrespective of sublimation the *terraces* between the steps will still be well represented by the flat, dry, stable solid surface described in our simulations. Thus the effects described will be readily observed, for example once the sliding tip velocity v is faster than the step flow velocity.

It is worth mention here what will be the relationship between the nanofrictional phenomena just described and macroscopic friction between two real surfaces. A real metal surface looks like Fig. 8.7, showing polycrystalline domains exposing different facets. Some of them will have SM, but some will be NM like NaCl(100). The NM facets being the only hard ones should be those supporting a normal load at $T_{\rm M}$. The overall friction will result as a compounded effect of all these facets, with rather unpredictable results, although the decrease of the friction near $T_{\rm M}$ might be explained by the lubrication due to SM facets.

General conclusions

Here I summarize the main milestones and new results of this theoretical thesis, along with old experiments it explains and new experiments it suggests.

I have simulated NaCl(100) at high temperatures, and found it to be a strongly nonmelting surface. Large NaCl(100) terraces should remain solid and flat even well above T_{M}. Experimental confirmation of this result should be possible by e.g. X-ray scattering or by AFM with the caution that terraces will evolve with time due to heavy sublimation/condensation.

I calculated to my knowledge for the first time the free energy of a solid surface up to and above the bulk melting point. The results show an exceptionally high surface entropy of NaCl(100), largely of anharmonic origin.

I have simulated the liquid NaCl surface and found it to contain a sufficient amount of molecular short-range order, to reduce its entropy relative to that of the solid, which I was able for the first time to compare to.

I have demonstrated that a liquid NaCl droplet will not spread on NaCl(100) at the melting point, and will rather form a partial wetting angle of 50°, while the nanodroplet experiment would be worth considering experimentally, the partial wetting directly explains the long established "bubble" results of Mutaftschiev and his group.

As a byproduct I also calculated the solid-liquid interface free energy γ_{SL} of liquid NaCl/NaCl(100), again a calculation that does not appear to have been done before. The value of γ_{SL} is found to be very large, roughly 1/3 of the liquid surface tension γ_{LV}, that fits well with the large differences of properties between solid and liquid. This interface free energy could be addressed experimentally through, e.g. recrystallisation experiments.

I found that NaCl(100) serves as a good prototype for a theoretical (possi-

bly also experimental) study of nanofriction close to the melting point, a new area where there basically no results. I discovered that at low temperatures in the deeply indented ploughing regime the friction coefficient remains constant, whereas at high temperatures ploughing tip will experience a strong frictional drop near T_{M}, despite the surface solidification before and after the tip passage. This decrease is connected with a local cloud of liquid surrounding the tip similar to the skating.

A gently pressed, flat tip will conversely experience a sharp increase of sliding friction close to T_{M}. This is related with increased softness of the surface, and can be associated theoretically to the celebrated "peak effect" in the critical current of type II superconductors.

I frankly hope that these simulated experiments will be followed by real ones on a real alkali halide, or other nonmelting surface.

Acknowledgements

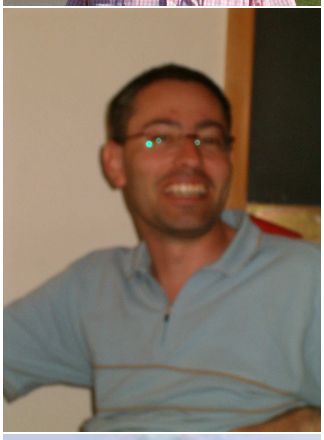

Four years passed rapidly... Four years of intensive work, new experiences, routine research, fallings and successes. For me they were years of growing: first conference, first talk, first article... I want to express my gratitude to SISSA as an institution. Here I have got an opportunity to work on modern computers, have access to recent research, study new things... I am grateful to Lorena and Student's Secretariat, who helped a lot at the first period of my stay in Trieste.

Of course, all these would be impossible without the people whom I was working with.
I want to thank my supervisor Erio Tosatti for teaching me to think and live in physics. For strong encouragement, faith and patience, for his ability always to find time and answer all my questions.
Great thanks to Davide for opening me the world of computers and ab-initio simulations. I cannot imagine this work without his genuine and effective help. For very kind, patient and optimistic support and friendly criticism.
I would like to acknowledge Ugo for illuminating discussions. I remember 2002: days and days of explanations and debugging the codes together. His influence was very crucial in some periods of my study. I appreciate his strong will to bring in order my codes, my Italian, my thoughts and my research. I hope I have picked up some features of his detail and profound approach to physics.
These years would be certainly less colorful and advantageless without my groupmates and friends. Sharing dreams, humor, ideas and realising them together was

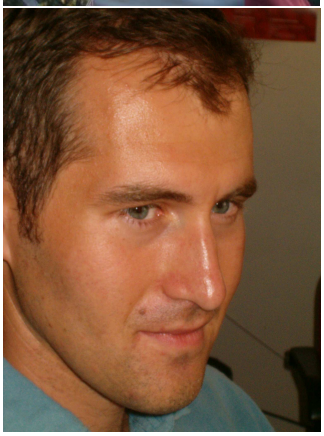

I wish to thank Claudio. Cheerful and open minded, he fills me with infinite enthusiasm, sincere friendship and real help, for millions of hints and advises in physics, computers, driving, life, etc.
Special thanks to Jaro for climbing lessons, Hamed for oriental wisdom, Lorenzo and Michele for stimulating environment, illuminating lunch discussions and many helpful suggestions. I hope to keep in touch in future and in any case I wish good luck.
During my PhD Katia and Natascia never permit me to give up. Their fervent spirit, fantasy, integrity, practical and full of life humor (" Are you still alive?") and suggestions always inspirit and keep me in form. Zhenia for many things.
I acknowledge the computational resources of CINECA and opteron in SISSA.
Of course, special thanks to my family.

Bibliography

[1] G. Grange and B. Mutaftschiev, Surf. Science **47**, 723 (1975).

[2] R. L. G. Grange and B. Mutaftschiev, J. Cryst. Growth **49**, 343 (1980).

[3] L. Komunjer and B. Mutaftschiev, J. Cryst. Growth **182**, 198 (1997).

[4] J. Frenken, P. M. J. Marèe, and J. F. van der Veen, Phys. Rev. B **34**, 7506 (1986).

[5] P. Carnevali, F. Ercolessi, and E. Tosatti, Phys. Rev. B **36**, 6701 (1987).

[6] B. Pluis, A. W. D. van der Gon, J. W. M. Frenken, and J. F. van der Veen, Phys. Rev. Lett. **59**, 2678 (1987).

[7] B. Pluis, D. Frenkel, and J. F. van der Veen, Surf. Science **239**, 282 (1990).

[8] X. Z. Wu *et al.*, Phys. Rev. Lett. **70**, 958 (1993).

[9] X. Z. Wu *et al.*, Science **261**, 1018 (1993).

[10] O. Gang *et al.*, Phys. Rev. Lett. **80**, 1264 (1998).

[11] According to S. Dietrich (private communication) surface melting could be called "complete interfacial wetting".

[12] F. D. Tolla, F. Ercolessi, and E. Tosatti, Phys. Rev. Lett. **74**, 3201 (1995).

[13] L. D. Landau and E. M. Lifshitz, *Statistical Physics* (Pergamon, Oxford, 1980), ch. XV.

[14] J. N. Israelachvili, *Intermolecular and surface forces* (Academic Press, San Diego, 1985).

[15] B. Pluis, T. N. Taylor, D. Frenkel, and J. F. van der Veen, Phys. Rev. B **40**, 1353 (1989).

[16] T. Zykova-Timan, U. Tartaglino, D. Ceresoli, and E. Tosatti, J. Chem. Phys. **123**, (2005).

[17] F. A. Lindemann, Phys. Z. **11**, 609 (1910).

[18] M. Ross, Phys. Rev. **184**, 233 (1969).

[19] P. M. Platzman and H. Fukuyama, Phys. Rev. B **10**, 3150 (1974).

[20] L. Pietronero and E. Tosatti, Solid State Commun. **32**, 255 (1979).

[21] G. Tammann, Z. Phys. Chem **68**, 205 (1910).

[22] C. S. Jayanthi, E. Tosatti, and A. Fasolino, Phys. Rev. B **31**, 470 (1985).

[23] J. Frenken and A. M. Molenbroek, Phys. Rev. B **50**, 11132 (1994).

[24] J. Hansen and L. Verlet, Phys. Rev. B **184**, 151 (1969).

[25] R. Lipowsky and B. Speth, Phys. Rev. B **28**, 3983 (1983).

[26] J. G. Broughton and L. V. Woodcock, Solid State Phys **11**, 2743 (1978).

[27] J. G. Broughton and G. H. Gilmer, J. Chem. Phys. **79**, 5105 (1983).

[28] F. Y. Hansen and H. Taub, Phys. Rev. Lett. **69**, 652 (1992).

[29] A. M. Molenbroek and J. W. Frenken, Phys. Rev. B **50**, 11132 (1994).

[30] J. van der Veen, in *Phase Transitions in Surface Films 2*, edited by H. Taub and *et al* (NATO – ASI Series B, New York, 1981), Vol. 267, p. 289.

[31] J. W. Herman and H. E. Elsayed-Ali, Phys. Rev. Lett. **74**, 3201 (1995).

[32] J. J. Métois and J. C. Heyraud, J. Phys. (Paris) **50**, 3175 (1989).

[33] F. D. Tolla, E. Tosatti, and F. Ercolessi, *Monte Carlo and Molecular Dynamics of Condensed Matter Systems* (Società Italiana di Fisica, Bologna, 1996), p. 345.

[34] A. C. L. X. J. Chen, F. Ercolessi and E. Tosatti, Surf. Science **264**, 207 (1992).

[35] R. Trittibach, C. Grutter, and J. H. Bilgram, Phys. Rev. B **50**, 2529 (1994).

[36] M. Yamada, Phys. Z. **24**, 364 (1923).

[37] G. Benedek *et al.*, Phys. Rev. B **28**, 2104 (1983).

[38] G. Boato, P. Cantini, and L. Mattera, Surf. Science **55**, 141 (1976).

[39] G. Janz, *Molten salts handbook* (Academic Press, New York, 1967).

[40] D. M. Heyes, Phys. Rev. B **30**, 2182 (1984).

[41] F. Bashforth and J. Adams, *An attempt to test the theories of capillary action* (University Press, Cambridge, 1883).

[42] D. Turnbull, J. Appl. Phys **21**, 1022 (1950).

[43] C. Valeriani, E. Sanz, and D. Frenkel, J. Chem. Phys. **122**, 194501 (2005).

[44] J. Heyraud and J. M*é*tois, J. Cryst. Growth **84**, 503 (1987).

[45] M. Wortis, in *Chemistry and physics of solid surfaces VIII*, edited by R. Vanselow and R. Howe (Springer-Verlag, Berlin, 1990).

[46] J. P. Rose and R. S. Berry, J. Chem. Phys. **98**, 3246 (1993).

[47] W. Zurek, Physics Today **44**, 36 (1991).

[48] M. S. Daw and M. I. Baskes, Phys. Rev. B **29**, 6443 (1984).

[49] F. Ercolessi, M. Parrinello, and E. Tosatti, Philos. Mag. **58**, 213 (1988).

[50] M. W. Finnis and J. E. Sinclair, Philos. Mag. **50**, 45 (1984).

[51] D. W. Brenner, Phys. Rev. B **42**, 9458 (1990).

[52] J. Tersoff, Phys. Rev. B **37**, 6991 (1988).

[53] N. Takeuchi, A. Selloni, and E. Tosatti, Phys. Rev. Lett. **72**, 2227 (1994).

[54] D. Frenkel and B. Smit, *Understanding molecular simulation : from algorithms to applications* (Academic Press, San Diego, 2002).

[55] M. P. Allen and D. J. Tildesley, *Computer simulation of liquids* (Clarendon Press, Oxford, 1987).

[56] H. C. Andersen, J. Chem. Phys. **72**, 2384 (1980).

[57] M. Parrinello and A. Rahman, Phys. Rev. Lett. **45**, 1196 (1980).

[58] S. Nozé, Mol. Phys. **52**, 255 (1984).

[59] J. Q. Broughton, G. H. Gilmer, and J. D. Weeks, J. Chem. Phys. **75**, 5128 (1981).

[60] M. Born and K. Huang, *Dynamical theory of crystal lattices* (Oxford Clarendon Press, Oxford, 1985).

[61] M. Born and J. E. Mayer, Z. Phys. **75**, 1 (1932).

[62] M. L. Huggins and J. E. Mayer, J. Chem. Phys. **1**, 643 (1933).

[63] F. G. Fumi and M. P. Tosi, J. Phys. Chem. Solids **25**, 31 (1964).

[64] M. J. L. Sangster and M. Dixon, Adv. Phys. **23**, 247 (1976).

[65] J. E. Enderby and G. W. Neilson, Advs. Phys. **29**, 323 (1980).

[66] N. March and M. Tosi, *Coulomb liquids* (Academic Press, London, 1984).

[67] B. Groh, R. Evans, and S. Dietrich, Phys. Rev. E **57**, 6944 (1998).

[68] M. González-Melchor, J. Alejandre, and F. Bresme, Phys. Rev. Lett. **90**, 135506 (2003).

[69] M. E. Fisher and Y. Levin, Phys. Rev. Lett. **85**, 3826 (1996).

[70] Y. P. Varshni and R. C. Shukla, J. Chem. Phys. **35**, 582 (1961).

[71] M. Wilson and P. A. Madden, J. Phys.: Condens. Matter **5**, 2687 (1992).

[72] F. G. Edwards, J. E. Enderby, R. A. Howe, and D. I. Page, J. Phys. C **8**, 3483 (1975).

[73] P. Tangney and S. Scandolo, J. Chem. Phys. **119**, 9673 (2003).

[74] N. March and M. Parrinello, *Collective effects in Solids and Liquids* (University of Sussex Press, Brighton, 1982).

[75] We acknowledge P. Tangney for giving us access to his code for polarizable Madden potentials.

[76] G. C. Benson, H. P. Schrieber, and F. van Zeggeren, Can. J. Chem. **34**, 1553 (1956).

[77] B. D. Todd, D. J. Evans, and P. J. Daivis, Phys. Rev. E **52**, 1627 (1995).

[78] H. Hendrik, P. Wolfgang, and K. Binder, , http://arxiv.org/abs/cond-mat/0309014.

[79] S. Ono and S. Kondo, *Molecular theory of surface tension* (Springer-Verlag, Berlin-Göttingen-Heidelberg, 1960).

[80] R. Shuttleworth, Proc. Phys. Soc. London **163**, 444 (1950).

[81] P. J. Steinbach and B. R. Brooks, J.Comp. Chem. **15**, 667 (1994).

[82] P. P. Ewald, Ann. Phys. **64**, 253 (1921).

[83] I. C. Yeh and M. L. Berkowitz, J. Chem. Phys. **111**, 3155 (1999).

[84] T. A. Darden, D. York, and L. Pedersen, J. Chem. Phys. **98**, 10089 (1993), we would like to acklowledge T. Darden who generously provided the code for PME calculations.

[85] D. E. Parry, Surf. Science **49**, 433 (1975).

[86] D. M. Heyes, M. Barber, and J. H. R. Clarke, J. Chem. Soc. Faraday Trans.II **73**, 1977 (1485).

[87] E. Spohr, J. Chem. Phys. **107**, 6342 (1994).

[88] A. A. Maradudin, *Theory of lattice dynamics in the harmonic approximation* (Academic Press, New York, 1971).

[89] M. Born, *Atomtheorie des festen Zustandes* (Teubner, Leipzig, 1923).

[90] D. Hooton, Phil. Mag. **46**, 422 (1958).

[91] D. A. McQuarrie, *Statistical Mechanics* (Harper Collins, New York, 1976).

[92] W. Shi and J. K. Johnson, Fluid Phase Equilib. **187**, 171 (2001).

[93] C. Micheletti, A. Laio, and M. Parrinello, Phys. Rev. Lett. **92**, 170601 (2004).

[94] A. Curioni and *et al*, J. Am. Chem. Soc. **119**, 7218 (1997).

[95] J. A. Barker and D. Henderson, Rev. Mod. Phys. **48**, 587 (1976).

[96] J. Anwar, D. Frenkel, and M. G. Noro, J. Chem. Phys. **118**, 728 (2003).

[97] *Landolt-Bornstein. Neue Serie. Gruppe III. Kristallstrukturdaten anorganischer Verbindungen. Teil a: Schlusselemente F, Cl, Br, J (VII. Hauptgruppe) Halogenie und Halogenkomplexe./ Crystal structure data of inorganic compounds. Part a: Key elements F, Cl, Br, I (VII. main group) halides and complex halides* (Springer-Verlag, Berlin, 1973), Vol. 7a.

[98] M. A. Viswamitra and K. Jayalakshmi, Acta Crystallogr. A **28**, S189 (1974).

[99] J. Hardy and A. Karo, *The lattice dynamics and statics of alkali halide crystals* (Plenum Press, New York, 1979).

[100] R. A. Cowley, W. Cochran, B. N. Brockhouse, and A. D. B. Woods, Phys. Rev. **131**, 1030 (1963).

[101] M. Amini, D. Fincham, and R. W. Hockney, J. Phys. C.: Solid State Phys. **12**, 4707 (1979).

[102] M. Amini and R. W. Hockney, J. Non-Cryst. Solids **31**, 447 (1979).

[103] R. Young and J. P. O'Connell, Ind. Eng. Chem. Fundam. **10**, 418 (1971).

[104] S. I. F. Ercolessi, O. Tomagnini and E. Tosatti, in *Nanosources and Manipulation of Atoms under High Fields and Temperatures: Aplications*, edited by V. T. Binh, N. Garcia, and K. Dransfeld (Kluwer, Dordrecht, 1993), Vol. 235.

[105] A. R. Belonoshko, R. Ahuja, and B. Johansson, Phys. Rev. B **61**, 11928 (2000).

[106] T. Zykova-Timan *et al.*, Surf. Science **566/568**, 794 (2004).

[107] P. Davidovits and D. L. McFadden, *Alkali halide vapors: structure, spectra and reaction dynamics* (Academic Press, New York, 1979).

[108] P. Brumer and M. Karplus, J. Chem. Phys. **58**, 3903 (1973).

[109] S. Dushman, *Scientific foundations of vacuum techniques* ("Wiley & Sons", New York, 1962).

[110] J. Akella, S. N. Vaidya, and G. C. Kennedy, Phys. Rev. **185**, 1135 (1969).

[111] B. Groh, R. Evans, and S. Dietrich, Phys. Rev. E **57**, 6944 (1998).

[112] U. Tartaglino, T. Zykova-Timan, F. Ercolessi, and E. Tosatti, Phys. Rep. **411**, 291 (2005).

[113] R. Evans and T. J. Sluckin, Molec. Phys. **40**, 413 (1980).

[114] R. L. Davidchak and B. B. Laird, Phys. Rev. Lett. **94**, 086102 (2005).

[115] J. Kolodiej *et al.*, Surf. Science **506**, 12 (2002).

[116] E. Riedo, E. Gnecco, R. Bennewitz, and et al, Phys. Rev. Lett. **91**, 084502 (2003).

[117] P. Noziéres, J. Phys (France) **50**, 2541 (1989).

[118] V. F. Petrenko and R. W. Whitworth, *Physics of ice* (University Press, Oxford, 1999).

[119] D. Dowson, C. Taylor, M. Godet, and D. Berthe, *Development in numerical and experimental methods applied to tribology* (Butterworths, London, 1984).

[120] F. P. Bowden and D. Tabor, *Friction: an introduction to tribology* (Doubleday, New York, 1973).

[121] J. Frenken, M. S. Hoogeman, and L. Kuipers, Surf. Science **340**, 231 (1995).

[122] L. Kuipers and J. Frenken, Phys. Rev. Lett. **70**, 3907 (1993).

[123] O. Tomagnini, F. Ercolessi, and E. Tosatti, Surf. Science **287/288**, 1041 (1993).

[124] T. Zykova-Timan, D. Ceresoli, U. Tartaglino, and E. Tosatti, Phys. Rev. Lett. **94**, 176105 (2005).

[125] H. Tang *et al.*, J. Chem. Phys. **108**, 359 (1998).

[126] B. J. Persson, *Sliding friction: physical principles and applications* (Springer-Verlag, Berlin, 1998).

[127] M. Hirano, K. Shinjo, R. Kaneko, and Y. Murata, Phys. Rev. Lett. **78**, 1448 (1997).

[128] M. Dienwiebel and *et al*, Phys. Rev. Lett. **92**, 126101 (2004).

[129] J. P. Hansen and I. R. McDonald, *Theory of simple liquids* (Academic Press, London, 1986), Chap. 8.

[130] E. Granato, T. Ala-Nissia, and S. Ying, Phys. Rev. B **62**, 11834 (2000).

[131] T. Ala-Nissila and S. Ying, Phys. Rev. B **42**, 10264 (1990).

[132] C. Tang, X. Ling, S. Bhattacharya, and P. Chaikin, Europhys. Lett **35**, 597 (1996).

[133] A. Maeda, Y.Inoue, and *et al*, Phys. Rev. Lett. **94**, 077001 (2005).

[134] I. E. Dzyaloshinskii, E. M. Lifshitz, and L. P. Pitaevskii, Soviet Phys. JETP **10**, 161 (1960).

[135] N. G. V. Kampen, B. R. Nijboer, and K. Schram, Phys. Lett. A **26**, 307 (1968).

[136] F. Wooten, *Optical properties of solids* (Academic Press, New York, 1972).

Appendix A

Numerical integration algorithm in md3

Nowadays one of the most attractive, simple and numerically stable integration scheme for Newton's equations of motion is velocity Verlet. Based on the Taylor expansion of the coordinates $\mathbf{r}(t)$ it calculates the position $\mathbf{r}(t+\delta t)$ at a time $t+\delta t$:

$$\mathbf{r}(t+\delta t) = \mathbf{r}(t) + \sum_n \frac{(\delta t)^n}{n!} \frac{\partial^n \mathbf{r}(t)}{\partial t^n}$$

If we add the corresponding equation for $\mathbf{r}(t-\delta t)$ and neglect the terms of order $(\delta t)^4$ and higher, a simple expression for the calculation of the particle position after a single time step is obtained:

$$\mathbf{r}(t+\delta t) = 2\mathbf{r}(t) - \mathbf{r}(t-\delta t) + \delta t^2 \frac{\mathbf{f}(t)}{m}$$

where m is an atomic mass and $\mathbf{f}(t)$ is the force experienced by this atom at time t. The velocities can be calculated at time t from the following expression:

$$\dot{\mathbf{r}}(t) = \frac{1}{2\delta t}(\mathbf{r}(t+\delta t) - \mathbf{r}(t-\delta t))$$

The described integration scheme is known as Verlet algorithm. A slight modification is velocity Verlet which calculates the velocities at time $t+\delta t$ using the velocities obtained at time $t+\delta t/2$:

$$\begin{aligned} \mathbf{v}(t+\frac{\delta t}{2}) &= \mathbf{v}(t) + \frac{\delta t}{2}\frac{\mathbf{f}(t)}{m} \\ \mathbf{r}(t+\delta t) &= \mathbf{r}(t) + \delta t \mathbf{v}(t) + \frac{(\delta t)^2}{2}\frac{\mathbf{f}(t)}{m} + \mathcal{O}(\delta t^4) \end{aligned}$$

Finally new velocities at time $t + \delta t$ are estimated as:

$$\mathbf{v}(t + \delta t) = \mathbf{v}(t) + \frac{\delta t}{2m}[\mathbf{f}(t + \delta t) + \mathbf{f}(t)] + \mathcal{O}(\delta t^3)$$

The modified velocity Verlet for Langevin and damping dynamics was developed by Ermak[55]. In his approximation the forces $\mathbf{f}(t)$ remain almost constant over the timestep δt. We implemented the algorithm for zero stochastic forces:

$$\begin{aligned} \mathbf{r}(t + \delta t) &= \mathbf{r}(t) + c_1 \delta t \mathbf{v}(t) + c_2 \delta t^2 \frac{\mathbf{f}(t)}{m} + \mathcal{O}(\delta t^4) \\ \mathbf{v}(t + \delta t) &= c_0 \mathbf{v}(t) + c_1 \delta t \frac{\mathbf{f}(t)}{m} + \mathcal{O}(\delta t^3) \end{aligned}$$

where $c_0 = e^{-\gamma \delta t}$, $c_1 = (\gamma \delta t)^{-1}(1 - c_0)$, $c_2 = (\gamma \delta t)^{-1}(1 - c_1)$ and γ is a friction coefficient.

The structure relaxation near the minimum of the potential energy is performed by "smart minimization", i.e. if $\mathbf{v}(t) \cdot \mathbf{f}(t) < 0$ the velocity $\mathbf{v}(t)$ is set zero.

Appendix B

Fitting the C_6 Van der Waals coefficient via Hamaker constant

The interaction of two polarizabe materials across a vacuum thickness ℓ is given by $-H/\ell^2$, where H is called the Hamaker constant [14] The evaluation of Hamaker constant is done using a simple analytic approach: we calculate the interactions between 2 semi-infinite media with complex dielectric constants $\varepsilon_1(\xi)$ and $\varepsilon_3(\xi)$, separated by a 3^{rd} medium with dielectric constant $\varepsilon_2(\xi)$, applying the general formula derived by Dzyaloshinskii [134] and independently by Van Kampen [135] for the case of "small" distances ($\ell \ll \lambda$, where λ is the principal absorption wavelength of the material):

$$H = \frac{\hbar}{32\pi^2} \int_0^\infty \int_0^\infty \frac{x^2}{b(\xi)\, e^x - 1} dx d\xi \tag{B.1}$$

with $\omega = i\xi$ imaginary frequency, $b(\xi)$ is given by

$$b(\xi) = \frac{\varepsilon_1(\xi) + \varepsilon_2(\xi)}{\varepsilon_1(\xi) - \varepsilon_2(\xi)} \quad \frac{\varepsilon_2(\xi) + \varepsilon_3(\xi)}{\varepsilon_2(\xi) - \varepsilon_3(\xi)} \tag{B.2}$$

For solid-vacuum-solid geometry $b(\xi)$ is simply

$$b(\xi) = \frac{\varepsilon_1(\xi) + 1}{\varepsilon_1(\xi) - 1} \quad \frac{1 + \varepsilon_3(\xi)}{1 - \varepsilon_3(\xi)}$$

In Eq. (B.1) one can suppose $b(\xi)\, e^x \gg 1$ and easily integrate over dx ($\int_0^\infty x^2 e^{-x} dx = 2$), so that the expression (B.1) takes the form

$$H = \frac{\hbar}{16\pi^2} \int_0^\infty \frac{\varepsilon_1(\xi) - 1}{\varepsilon_1(\xi) + 1} \quad \frac{1 - \varepsilon_3(\xi)}{1 + \varepsilon_3(\xi)} d\xi \tag{B.3}$$

To compute the latter integral it is necessary to express directly the dielectric constant dependence on the frequency.

The dielectric function can be modeled as Drude-Lorentz oscillator. For an insulator with mean gap $\hbar\omega_0$ and damping Γ the complex dielectric function is [136]:

$$\varepsilon(\omega) = 1 + \frac{\omega_p^2}{\omega_0^2 - \omega^2 - i\Gamma\omega}$$

with plasma frequency

$$\omega_p^2 = \frac{4\pi n e^2}{m}$$

where $n = Z\, n_{at}$ is the number density of the free (valence) electrons.

The mean bandgap energy can be estimated from the refractive index, namely:

$$n_R^2 = \varepsilon(0) = 1 + \frac{\omega_p^2}{\omega_0^2} \tag{B.4}$$

The parameters and bandgap results are given in the Table B.

	NaCl	C
n_R	1.5442	2.4173
Z(valence)	8	4
lattice spacing (Å)	5.9	3.566
$\hbar\omega_p$ (eV)	14.6	31.2
$\hbar\omega_0$ (eV)	12.4	14.6

Calculating the analytical continuation of $\varepsilon(\omega)$(an even function) (Eq.(B)) on upper halfplane ($\xi > 0$) the final result yields:

$$\varepsilon(i\xi) = 1 + \frac{\omega_p^2}{\xi^2 + \Gamma\xi + \omega_0^2} \tag{B.5}$$

Substituting expressions (B.4) and (B.5) for $\varepsilon(\omega)$ into the formula (B.3) one get the integral of the form (Γ is almost negligible for insulators)

$$\int_0^\infty \frac{dx}{(a^2 + x^2)(b^2 + x^2)} = \frac{\pi}{2ab(a+b)}$$

where

$$\begin{aligned} a^2 &= \omega_0^2(NaCl) + 1/2\omega_p^2(NaCl) \\ b^2 &= \omega_0^2(C) + 1/2\omega_p^2(C) \end{aligned}$$

The Hamaker constant for NaCl-vacuum-diamond interactions is found to be -0.05391 eV and for NaCl-vacuum-W interactions— -0.1325 eV. From another definition of Hamaker constant $H = \frac{\pi}{12} C_6(\rho_C - \rho_v)(\rho_v - \rho_{NaCl})$ we can derive the values for the Van der Waals interaction parameters C = 60.27 eV $\cdot$ Å^6 and C = 414 eV $\cdot$ Å^6 accordingly.